Fabrication of room temperature gas sensors based on metal oxide semiconductor nanostructures

Thesis submitted to

COCHIN UNIVERSITY OF SCIENCE AND TECHNOLOGY

in partial fulfillment of the requirements

for the award of the degree of

DOCTOR OF PHILOSOPHY

Subha P P

DEPARTMENT OF PHYSICS

COCHIN UNIVERSITY OF SCIENCE AND TECHNOLOGY

COCHIN - 682022, KERALA, INDIA

November 2017

Fabrication of room temperature gas sensors based on metal oxide semiconductor nanostructures

Ph.D. thesis in the field of material science

Author:

Subha P P
Nanophotonic and Optoelectronic Devices Laboratory
Department of Physics
Cochin University of Science and Technology
Cochin - 682 022, Kerala, India.
Email: subhapp8@gmail.com

Supervisor:

Dr. M K Jayaraj
Professor
Department of Physics
Cochin University of Science and Technology
Cochin - 682 022, Kerala, India.
Email: mkj@cusat.ac.in

November 2017

Dedicated to my Achan and Amma

Department of Physics,
Cochin University of Science and Technology,
Kochi-682022, India

Dr. M K Jayaraj
Professor

28th November 2017

Certificate

Certified that the work presented in this thesis entitled ***"Fabrication of room temperature gas sensors based on metal oxide semiconductor nanostructures"*** is based on the authentic record of research carried out by Subha P P under my guidance in the Department of Physics, Cochin University of Science and Technology, Cochin 682 022 and has not been included in any other thesis submitted for the award of any degree. All the relevant corrections and modifications suggested by the audience during the pre-synopsis seminar and recommendations by the Doctoral committee of the candidate have been incorporated in the thesis.

Dr. M K Jayaraj
(Supervising Guide)

---

phone: +91 484 2577404 extn. 33 Fax: 91 484 2577595 Email: mkj@cusat.ac.in

Declaration

I hereby declare that the work presented in this thesis entitled ***"Fabrication of room temperature gas sensors based on metal oxide semiconductor nanostructures"*** is based on the original research work carried out by me under the supervision and guidance of Dr. M K Jayaraj, Professor, Department of Physics, Cochin University of Science and Technology, Cochin-682022 and has not been included in any other thesis submitted previously for the award of any degree.

Kochi-22 Subha P P

28th November 2017

Acknowledgement

The completion of this doctoral thesis would not have been possible without the help and support of a great many people who deserve to be both acknowledged and thanked here. It is with pleasure; I record my sincere gratitude and appreciation to each one of them.

At this moment of accomplishment, I am greatly indebted to my supervising guide Prof. M.K.Jayaraj for his valuable guidance, constant support, and scholarly inputs I received throughout the entire research period. His deep insight helped me a lot at various stages of my research work. Under his guidance, I successfully overcame many difficulties and learned a lot. I sincerely thank him for the prompt reading and careful analysis of my thesis.

I thank Prof. M Junaid Bushiri, Head, Department of Physics and all the former Heads of the Department - Prof. S. Jayalekshmi, Prof. B. Pradeep and Prof. M.R. Anantharaman for permitting me to use the research facilities in the Department. I thank all other teachers in the Department for their encouragement and support.

I would like to thank Dr. Aldrin Antony, IIT Bombay for extending his help at various stages of my research period. I thank Dr.P.M. Aneesh, Central University of Kerala, for all the help and support given to me right from the beginning of my Ph.D. career.

I thank SAIF STIC-CUSAT, SAIF -IIT Bombay, CeNSE -IISC, and CNN-M.G University for the characterization facilities provided.

I am grateful to Department of Science and Technology and University Grant Commission for research fellowship.

I thank all the nonteaching staff of Department of Physics and Administrative office, CUSAT for all the help and cooperation.

Special thanks to all my teachers for their encouragements at different stages of the academic life.

I am extremely thankful to my senior researchers in OED lab, Dr. Arun Aravind, Dr. James K K, Dr. Satish B, Dr. Reshmi R, Dr. Saji K J, Dr. Sreeja R, Dr. Sanal K C, and Dr. Sasank for all the help and support.

I gratefully acknowledge the support of my dear friends Dr. Hasna, Dr. Vikas and Dr. Saritha for their generous care throughout the research period. Their timely help and friendship shall always be remembered. My heartfelt thanks to Kurias and Shijeesh for their friendship.

My sincere thanks to the really supportive and active young generation of OED lab for all the co-operation and support I received. I thank Anjana, Jasna, Manu, Abhay, Anju, Midhun, Merin and Subin for the lively atmosphere and fruitful discussions in the lab. My special thanks to Ratheesh, Dr.Rajeev, Dr.Sreekumar, Dr.Aswathy and Dr.Kavitha for their help and suggestions. I remember with gratitude Dr.Vanaja, Anooja and Anjala for their help and care.

I treasure my friendship with Rajesh, Majeesh, Dr.Navaneeth, Dr. Sajan, Dr. Deepu, Dr.Poornima, Dr.Geetha, Dr.Subin, Dr. Anu, Dr.Santhosh, Geethu, Anshad, Tittu, Archana, Sreejith, manoj and Savitha.

Words cannot express the feelings I have for my parents for their constant unconditional love and support. I owe my deepest gratitude to Achan and Amma for their sacrifice and support. It is their determination and constant encouragement that ultimately made it possible for me to see this journey to the end. Thanks to my brother Syam for his love and care.

My heartfelt regard goes to my father in law, mother in law and sister in law for their love and moral support.

Finally, I would like to acknowledge my husband Dr.Krishnaprasad for his continued and unfailing love, patience, support and understanding during my Ph.D. tenure that made the completion of the thesis possible. He was always with me at times I thought that it is impossible to continue and I greatly value his contribution throughout the entire Ph.D. career. No words to express my love and affection to my little angels Malavika and Nandhika who are the pride and joy of my life.

Above all, I thank the almighty for giving me the strength and patience to work through all these years.

Subha

Contents

List of figures

List of tables

Preface

A sensor is a device which detects the presence of chemical or biological molecules. In recent years, the demand for chemical sensors is growing at a consistent rate due to their wide use in environmental monitoring, medical diagnostics, industrial safety, automotive emission monitoring etc. Off all the numerous solid-state sensors, metal oxide semiconductor nanostructures are the potential candidate for fabricating efficient gas sensors because of their interesting properties. The resistance of oxide-based sensors greatly depends on the surrounding atmosphere with which the material is in contact with. The high-temperature operation of oxide-based sensors limits their use in so many applications. In addition, miniaturization as well as reduced power consumption of the device is not possible with sensors operating at high temperature. Extensive research has been carried to fabricate low cost, portable gas sensors with reduced power consumption and better gas sensing properties. Doping, formation of hierarchical structures, UV light illuminations etc. are some of the possible routes for improving the gas sensing properties together with reducing operating temperature of the sensor.

The basic gas sensing mechanism of metal oxide based gas sensors relies on the interaction between target molecules and adsorbed oxygen ions on the surface of the semiconductor. The reaction changes the resistance of the material in accordance with nature of the target gas as well as the sensing material. A good sensor should possess a high value for response and fast response and recovery times. The focus of the present thesis is towards fabricating room temperature gas sensors with better gas sensor parameters. The content of the various chapters is summarized below.

Chapter 1 gives an introduction to metal oxide based gas sensors, their working principles applications etc. A brief literature review of different metal oxide nanostructures studied under the present work and their properties are also discussed. A detailed description of the need for room temperature gas sensors is included in this chapter.

Chapter 2 includes the details of the hydrothermal method used for the synthesis of various nanomaterials. The basic mechanism and the parameters which affect the hydrothermal reaction are also discussed. We have fabricated an in-house experimental set up for gas sensing measurements. The details of the experimental set up fabricated are also included in this chapter.

Chapter 3 deals with the synthesis, characterization, and room temperature gas sensing properties of ZnO and ZnO/CuO heterojunction sensors. The samples were synthesized using simple solution techniques including hydrothermal and wet chemical methods. The response of our devices to ethanol, hydrogen sulfide and ammonia were investigated at room temperature. Improved response parameters have been observed in the case of n-ZnO/p-CuO heterojunction compared to ZnO alone. The response value was 2 for ZnO and it is enhanced to 6 in the case of ZnO/CuO heterostructure. The gas sensing mechanism of the devices is described in detail.

Chapter 4 includes the effect of seed layer on the growth of TiO_2 as well as the attachment of Ag nanoparticles on the gas sensing properties of TiO_2 nanorods. TiO_2 nanorods were grown on FTO/glass substrates by seed-mediated hydrothermal method. The deposition of seed layer promoted the growth of well separated individual TiO_2 nanorods on

FTO/glass substrates. The exceptional catalytic properties of Ag nanoparticles enhanced the interaction between adsorbed oxygen ions and target gas molecules leading to better gas sensing properties in Ag-TiO_2 heterostructure. With the addition of Ag nanoparticles, the response and recovery time of the sensor has been reduced to 3 and 73 seconds from 6 and 213 seconds respectively. The gas sensing mechanism of Ag-TiO_2 heterostructure is also investigated.

Chapter 5 details the growth and characterization of n-TiO_2/p-CuO heterojunction and its room temperature gas sensing properties. The attachment of CuO nanoparticles on the surface of TiO_2 nanorods forms p-n heterojunctions. The formation of heterojunction increases the overall resistance of the sensing material due to the formation of depletion regions at the n-side and at the interface of the junction. The formation of p-n heterojunction, as well as the increased surface area of the device, enhanced the room temperature ethanol sensing properties. The response of the TiO_2/CuO sensor enhanced to 34 where the value was 8 for TiO_2 sensor. The mechanism responsible for the improved sensing properties is also discussed.

Chapter 6 describes the fabrication of n-TiO_2/n-ZnO heterojunction device by two-step hydrothermal method. The samples were characterized and room temperature gas sensing properties were investigated. The migration of charge carriers across the n-n junction forms an accumulation layer at the side of ZnO which is further depleted by additional oxygen adsorption, enhancing the gas sensing properties of TiO_2/ZnO heterojunction device. In the case of TiO_2/ZnO sensor, we got all the response parameters enhanced together. The response has been increased to 40 from 8 and recovery time has been reduced to 90 seconds

from 213 seconds respectively. The gas sensing mechanism of the heterojunction device is also discussed in detail.

Chapter 7 summarizes the main results in the thesis and recommends the scope for future works.

Publications related to the work presented in the thesis

Journal publications

1. Surface modification of TiO_2 nanorod arrays by Ag nanoparticles and its enhanced room temperature ethanol sensing properties, **P P, Subha**, K Hasna and M K Jayaraj, *Material Research Express* 4(10) (2017).

2. Enhanced room temperature gas sensing properties of low-temperature solution-processed ZnO/CuO heterojunction, **P P Subha** and M K Jayaraj, *Chemistry Central Journal* (Under review).

3. Solution-processed TiO_2/CuO heterojunction for enhanced room temperature ethanol sensing applications, **P P Subha**, L S Vikas and M K Jayaraj, *Physica Scripta* (Under review).

Other publications to which author has contributed

1. Solar photocatalytic degradation of methyl orange dye using TiO_2 nanoparticles synthesized by sol–gel method in neutral medium, **P P Subha**, M K Jayaraj, *Journal of Experimental Nanoscience* 10 (14), (2014).

2. Wide band gap-type semiconducting thin films grown by pulsed laser deposition, A C Saritha, S Sasanka Kumar, M Majeesh, K Hasna, **P P Subha**, L S Vikas and M K Jayaraj, Journal of electron devices 19, (2014).

3. Enhanced green upconversion luminescence in ZnO:Er^{3+},Yb^{3+} on Mo^{6+} co-doping for temperature sensor application, Anjana R; **P P Subha**, K M Kurias, and M K Jayaraj, *Methods and Applications in Fluorescence* (Accepted).

4. Development of highly sensitive recyclable surface-enhanced Raman scattering substrates using TiO_2 nanorods decorated with Ag nanoparticles, K Hasna, **P P Subha**, K Rajeev Kumar and M K Jayaraj, *Journal of Materials Science* (Under review).

5. Fast UV sensing properties of n-ZnO nanorods/p-GaN heterojunction, L S Vikas, K A Vanaja, **P P Subha**, M K Jayaraj, *Sensors and Actuators A: Physical* 242, (2016)

Conference presentations

1. Room temperature hydrogen sulfide gas sensing using metal oxide nanorod arrays, **P P Subha**, K Hasna and M K Jayaraj, IUMRS-(ICEM-2014, Taiwan).

2. H2S gas sensing properties of ZnO nanorods synthesized by hydrothermal method, **P P Subha**, K Hasna, L S Vikas, A C Saritha and M K Jayaraj, (IUMRS-ICA-2013, Bangalore, India).

3. Solar Photocatalytic Degradation of Methyl Orange Dye Using TiO_2 Nanoparticles Synthesized by Sol-gel Method in Neutral Medium, **P P Subha**, Meera S, Hasna K, Vikas L S, Vanaja K A, M.K Jayaraj, Saritha A.C, (ICMAT-2013, Singapore).

4. Hydrothermal synthesis of TiO_2 nanorod arrays for Gas sensor applications**, P P Subha** and M K Jayaraj (Nano India 2013, NIIST, Thiruvananthapuram).

5. Photoluminescence of ZnO microrods synthesized by hydrothermal method, **P. P. Subha**, L.S. Vikas, K. Hasna and M. K. Jayaraj, (Cochin Nano 2011, Cochin, India).

6. Growth of vertically aligned ZnO nanorods on various substrates by hydrothermal method, P. M. Aneesh, **P P Subha**, L. S. Vikas, Sonima Mohan and M. K. Jayaraj, Proc. of SPIE, 7766, 776606-1, (2010)

7. Enhancement of a-Si: H solar cell efficiency by Y2O3: Yb3+, Er 3+ near-infrared spectral upconverter, K M Kurias, R Anjana, **P P Subha**, A Antony, MK Jayaraj, Next Generation Technologies for Solar Energy Conversion VII 9937, 99370X (2016).

8. Preparation of ZnO nanoparticles showing upconversion luminescence through simple chemical method, R Anjana, **P P Subha**, K M Kurias, and M K Jayaraj, AIP Conference Proceedings 1731 (1), 050078 (2016).

Chapter 1

Introduction to metal oxide semiconductor gas sensors

This chapter details the importance of metal oxide semiconductor nanostructures in gas sensing applications, their basic working principles and various performance parameters of a gas sensor. The methods to improve the gas sensing performance, the reasons for the enhanced sensing properties and various applications of gas sensors are also discussed in detail.

1.1 Metal oxide semiconductors

Among the inorganic semiconductors, metal oxides are the focus of current research since they are the most common minerals on earth and also due to their physical and chemical properties and functionalities. The

electrical behavior of metal oxides[1,2] ranges from insulators (e.g., Al_2O_3, MgO) through semiconductors (TiO_2, ZnO etc.) to metals (V_2O_3, ReO_3) which finds numerous applications in the fields of transparent electronics, piezoelectric devices, spintronics, catalysis, sensors, solar cells etc. Figure 1.1 schematically depicts the technological application of metal oxides. A thorough understanding of the fundamental properties of a metal oxide system is a prerequisite in research and development towards practical applications. It has been known for the last five decades that the electrical conductivity of metal oxide semiconductors varies with the changes in the surrounding atmosphere.[3–5] The tunable physical and chemical properties of metal oxide semiconductors make them a promising candidate in the gas sensing industry.[6–8]

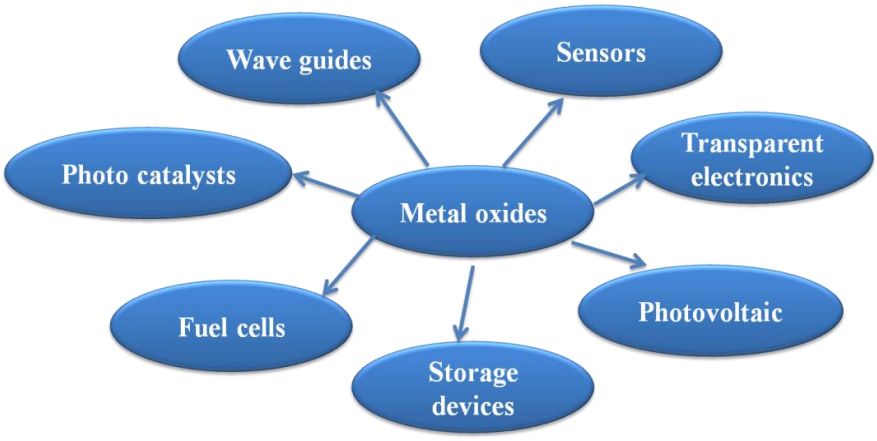

Figure 1.1. Technological applications of metal oxides.

The development in the field of nanotechnology has contributed to significant improvements in the gas sensor industry because of the interesting properties of nanomaterials.[9–11] The unique properties such as

large surface to volume ratio and enhanced electron transfer kinetics linked to the nanometer size of nanostructured metal oxides have attracted great interest.[12,13] Gas sensitivity down to parts per billion has been achieved with oxide nanostructures such as rods, particles, wires etc. The improved sensitivity together with the advantages of nanostructures helps scientists and researchers to fabricate portable low power consuming gas sensors. If the dimensions of particles are comparable to the wavelength of electrons, quantum mechanical effects play an important role in changing their physical properties, especially the electrical, magnetic and optical properties.[11,13] A blue-shift in optical spectra of quantum-confined particles and an increase in luminescence efficiency of semiconductors make them suitable for fabricating various semiconductor devices.[14,15]

1.2 Metal oxide chemiresistive gas sensors

Reliable detection of hazardous, harmful or toxic gases has become a major issue due to more stringent environmental or safety regulations worldwide. Emissions from automobiles and industry are major sources of hazardous gases such as carbon monoxide (CO), hydrogen sulfide (H_2S), nitrogen oxides (NO_x), volatile organic compounds (VOCs) etc. Exposure to the above hazardous gases cause shortness of breath, nausea, swelling of tissues in the throat, impair immunity system and in the worst case, they may even cause death.[16] Solid state gas sensors present a high potential for applications where the use of highly sensitive analytical techniques such as gas chromatography, spectrophotometry, high-performance liquid chromatography etc. are prohibitively expensive. The interaction between the analyte in the surrounding gas phase and the sensor material is transduced into a

measurable electrical signal that most often is a change in the conductance, capacitance, or potential of the sensor material. Different gas sensitive metal oxide nanostructures have been identified and used in the field of air quality monitoring and industrial safety. Due to this wide application range, the need for cheap, small, low power consuming and reliable solid-state gas sensors have grown over the years and triggered a huge research worldwide.

1.2.1 Historical background

A sensor is a device which can detect the presence of a chemical or biological molecule in the ambient. Chemiresistive gas sensors based on semiconducting metal oxides have attracted the attention of many researchers and scientists due to the low cost, flexibility associated with their production, simplicity of their use, a large number of possible applications etc. Before the invention of gas detecting devices, people used canary birds in mines to detect the presence of poisonous gases like carbon monoxide, methane etc., because the anatomy of canaries are something special that they need more oxygen hence they are highly sensitive to toxic gases. In the early 1950s, it was understood that some semiconductor materials modify their resistance depending on the surroundings they are in contact with. In 1953, Brattain and Bardeen observed this effect in Ge.[17] Heiland in 1954 described that metal oxide semiconductors such as ZnO also modify their semiconducting properties with change in its ambient.[18] Later, in 1962 Seiyama and Kato showed that the conductivity of ZnO thin films heated to ~300°C was sensitive to the presence of traces of reactive gases in the air.[19] In 1967, Shaver explained the effects of noble metal (Au, Ag, Pd, Pt etc.) addition on the

surface of metal oxide gas sensors.[20] These results initiated further development of commercial gas sensors. At the beginning of 1970s, Taguchi brought metal oxide semiconductors to an industrial product. The first chemiresistive gas sensor was fabricated and patented by Taguchi using SnO_2.[21] Taguchi type sensors are now one of the world's leading gas sensor manufacturers and it is the present day Figaro Engineering Inc. in Japan. By the end of 1980's, semiconductor-based gas sensors became one of the thrust areas of research for the sensor community. The need for gas sensors with high sensitivity, selectivity, faster response and recovery, thermal and chemical stability, low power consumption etc. generated intensive efforts to develop new gas sensing materials. The dramatic development in the understanding of material science and material chemistry helped scientists and researchers to fabricate high-performance gas sensors.

The early metal oxide-based sensor materials possessed a number of unfavourable characteristics such as high cross-sensitivity, poor selectivity, sensitivity to humidity, long-term signal drift and slow sensor response.[22] In order to improve sensor performance, a series of various metal oxide semiconductors have been tested. At first, the poor understanding of sensor response mechanism caused the use of trial and error strategy in the search for an appropriate material. Binary metal oxides such as SnO_2[23], ZnO[24], TiO_2[25] etc. are the commonly used sensing materials. The most successful investigations were on sensors based on SnO_2. Figure 1.2 represents the current status of studies on n- and p-type oxide semiconductor gas sensors.

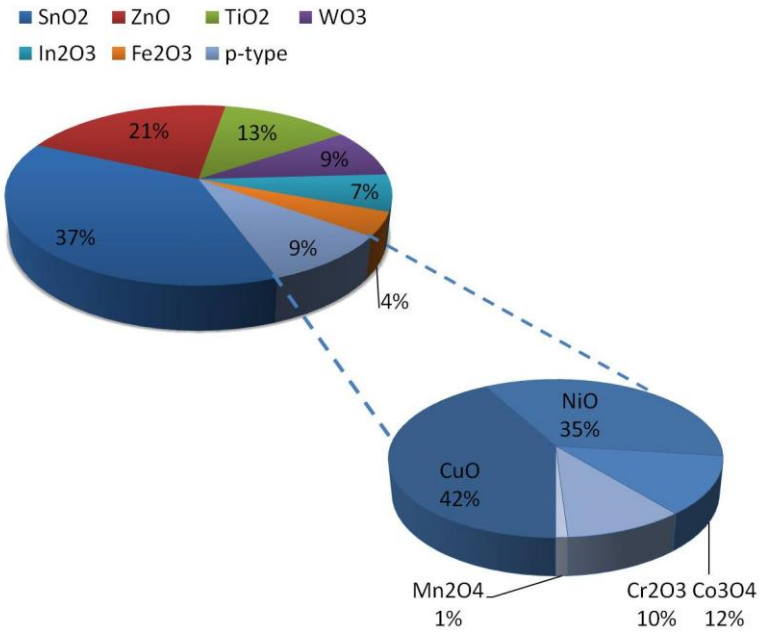

Figure 1.2. Statistics of the studies on various n- and p-type oxide semiconductor gas sensors. [15]

1.2.2 Working principle of metal oxide gas sensors

Over the years great efforts have been made by scientists and researchers to understand the sensing mechanism as well as the underlying processes. In the early days, the sensing mechanism was explained on the basis of electron theory of chemisorption and catalysis on semiconductors developed by Wolkenstein in 1961.[26] Later, in the beginning of 1980s, the electric charge transport through metal oxide semiconductor in oxygen and target gas ambient have been described in detail.[27,28] Following these theories, the fundamental sensing mechanism of metal oxide semiconductor sensors relies on the change in resistance upon interaction between the adsorbed oxygen molecules and the target

gases.[13,29–31] Even though the working principle is simple, the mechanism involved in gas sensing is fairly complex. The basic working principle of chemiresistive sensors includes a receptor function and transducer function.[7,32,33] Sensors based on metal oxide semiconductors are mainly applied to detect target gases through redox reactions between the target gases and the adsorbed oxygen ions on the metal oxide surface which includes two steps:

a) Redox reactions, during which oxygen ions distributed on the surface of the materials would react with molecules of target gases, leading to a change in the width of the depletion region formed on the surface of the oxide surface.

b) This variation is transduced into a change in electrical resistance of the sensors. The resistance variation could be detected by measuring the change of capacitance, work function, mass, optical characteristics, reaction energy etc.

Conductometric metal oxide gas sensors rely on changes in electrical conductivity due to the interaction with the surrounding atmosphere. The normal operating temperature of metal oxide gas sensors is in general within the range between 200°C and 500°C where conduction is electronic and oxygen vacancies are doubly ionized.[34,35] At higher temperatures, oxygen vacancy mobility becomes appreciable and the mechanism of conduction becomes mixed ionic-electronic. Metal oxide gas sensors should be operated at temperatures low enough so that appreciable bulk variation never occurs and high enough so that gas reactions occur in a time of the order of the desired response time. Gas

sensors working at room temperature is the focus of current gas sensor industry because of their reduced power consumption and their use in explosive environments where high temperature is not favorable.[36–39]

The sensing mechanism in metal oxide (MO) gas sensors is related to adsorption of species over their surfaces. The adsorption phenomena can be of two types: physisorption[28] and chemisorption.[35,40] Physisorption is defined as an adsorption event where van der Waals forces are involved in the bonding between the surface and adsorbate. Chemisorption is the formation of a chemical bond between the molecule and the surface during the adsorption process which requires activation energy. The most important chemisorbed species when operating in ambient air are oxygen and water. At lower temperature (< 100°C) oxygen adsorbs over metal oxide in molecular (O_2^-) form, since O_2^- has lower activation energy. At temperatures greater than 100°C, the atomic O^- or O^{2-} forms dominate.[5,29,41–43] The buildup of oxygen ions leads to the formation of an electron depletion region or space charge region and potential barrier at each grain boundary as shown in the figure 1.3. Electrons must acquire enough energy to overcome this double Schottky potential barrier which now controls the conductance of the material.

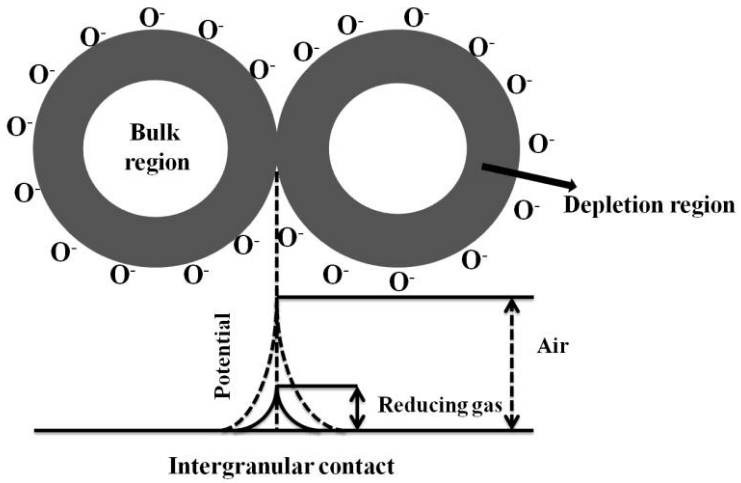

Figure 1.3. Schematic depicting the potential barrier developed at the intergranular contact of two oxide particles.

When a reducing gas like H_2S is introduced into the sensing material, it will react with the adsorbed oxygen ions on the surface which causes electrons to be injected back into the material releasing SO_2 and H_2O. This leads to the reduction in potential barrier height between adjacent particles generating a measurable change in the conductivity of the material. The H_2S sensing mechanism of metal oxides is schematically demonstrated in figure 1.4.

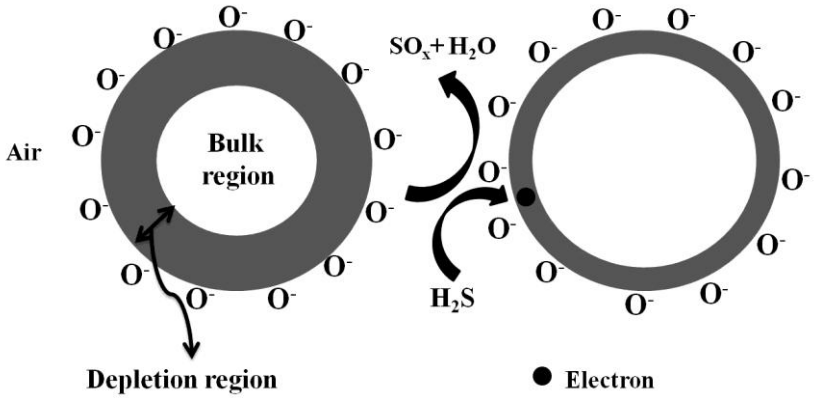

Figure 1.4. H_2S sensing mechanism of metal oxide nanostructures.

1.2.3 Performance parameters of a metal oxide semiconductor gas sensor

The morphology of the sensing material has a significant effect on the gas sensing properties. The gas sensing material can be classified into dense and porous.[43,44] In dense or compact material, the gas molecules can interact only with the surface of the oxide material. Figure 1.5 shows the schematic representation of a compact sensing layer where Z_g, Z_0 and qV_s are sensing layer thickness, thickness of the depletion region and band bending, respectively. Here, the geometric surface itself is the active surface where interaction takes place.

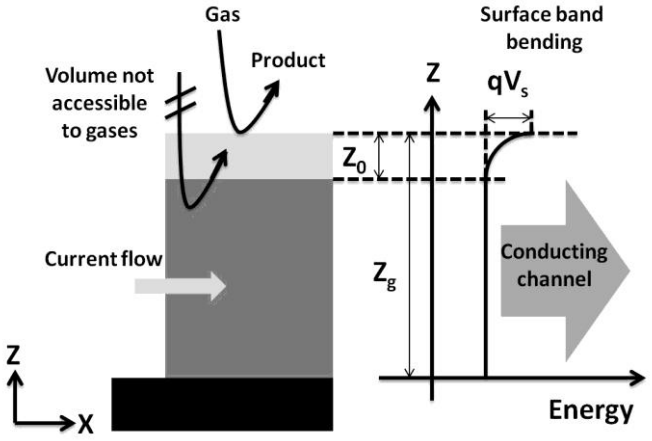

Figure 1.5. Schematic representation of a compact sensing layer.

In the case of porous sensing materials, the target gas molecules can penetrate into the inner oxide grains which will enhance the sensitivity. Here, the interaction between the target gas and the oxide takes place at the surface of individual grains, boundaries between grains and also at the interface of oxide and electrode; hence the active surface is much higher than the geometric one. The schematic representation of porous sensing layer with geometry and energy band is shown in figure 1.6 where X_g, X_0, E_b and qV_s are grain size, depletion layer thickness, minimum of the conduction band in the bulk and band bending respectively. For a better gas sensor, a significant amount of porosity is necessary. Porous material is defined as a continuous solid material filled with voids. International Union of Pure and Applied Chemistry (IUPAC) classified porous materials into macro, meso and micro porous materials depending on the pore size. Micro porous materials have pore size less than 2 nm, pore size is in between 2 nm and 50 nm for mesoporous and if

it is greater than 50 nm, the material is called macro porous.[45] Among the different classes of porous materials, mesoporous materials have the highest potential for gas sensing applications.

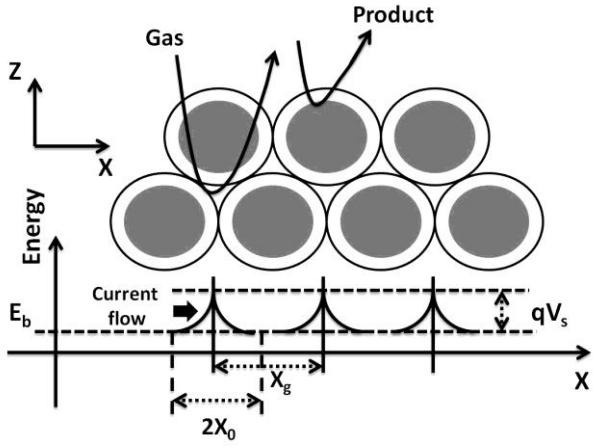

Figure 1.6. Schematic representation of a porous sensing layer.

The sensing performances of a sensor are controlled by three main factors such as receptor function played by the surface of each grain, transducer function played by the grain boundary and utility factor of the sensing body shown in figure 1.7.[7,32,46] The receptor function involves how the material responds to the surrounding atmosphere containing oxygen and other target gases. Oxygen molecules get adsorbed on the material by withdrawing electrons from the conduction band and form a depletion layer. The target gases react with these adsorbed oxygen molecules and change the resistance of the material depending on the nature of the sensor material (n-type or p-type) and the gas (reducing or oxidizing) molecules.

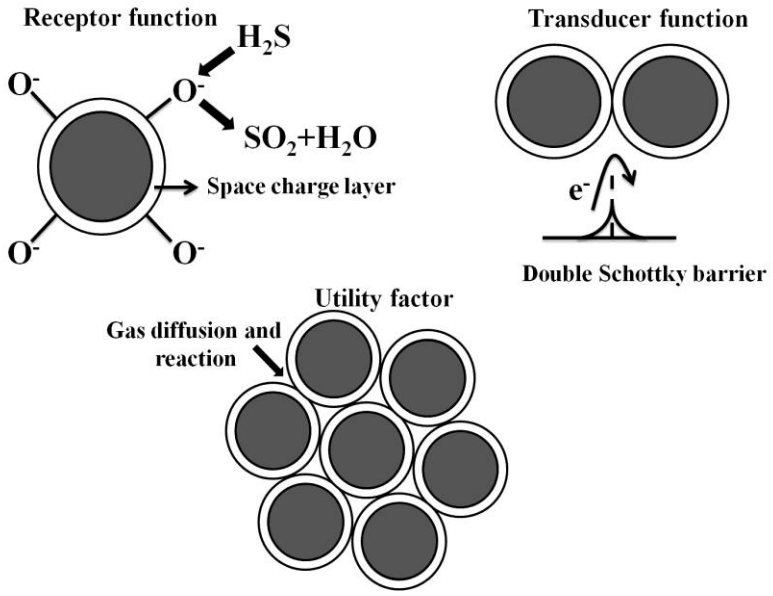

Figure 1.7. The factors determining the response of metal oxide semiconductor gas sensor.

The receptor function depends on the adsorption-desorption parameters. The adsorption and decomposition of gas molecules can be explained by physisorption and chemisorption. In physisorption or physical adsorption, the forces of attraction between the adsorbate and adsorbent are weak van der Waals type. Generally, physisorption is reversible and the adsorbate can be easily removed by increasing temperature or decreasing pressure. Here, the adsorbates do not require any activation energy and they are not fixed to any specific sites. Whereas in chemisorption, the forces of attraction are ionic or covalent and the adsorbates require activation energy. The activation energy is regarded as

the minimum energy required to undergo a reaction. The reaction is highly specific and irreversible. Both physisorption and chemisorptions increase with an increase in surface area of the oxide semiconductor.

Transducer function is the capability of the device to convert changes caused by the gas interaction into an electrical signal. This function is controlled by the semiconductor itself, such as grain size, grain boundaries, contacts between the electrode and the oxide and the electrochemical interactions taking place between the semiconductor and the gas molecules.[47,48] Grain size has a significant role in transducer function and the effects are schematically shown in figure 1.8. For an n-type semiconductor, the adsorption of any reducing gas decreases the width of the depletion region and correspondingly the height of the barrier decreases.[10,32] If the grain size D is very much larger than the Debye length L_D ($D >> 2L_D$), the gas interactions takes place only at the surface of the grains and the bulk of the semiconductor remain unaffected. In this case the sensing mechanism is independent of the grain size. If $D \geq 2L_D$, the conducting channel is influenced as shown in the figure 1.8. Here, compared to the previous case the response will be improved because of the increase in surface to volume ratio of the semiconducting oxide. If $D \sim 2L_D$, the material is fully depleted of free charge carriers and the sensor will exhibit excellent response.

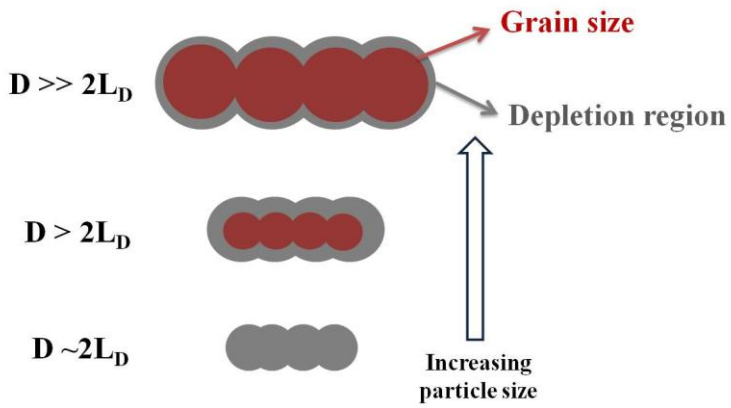

Figure 1.8. Schematic representation of grain size effects.

The utility factor is associated with the accessibility of the inner oxide grains to the adsorbed target gas. The target gas molecules can diffuse into the sensing material while reacting with the adsorbed oxygen. If the reaction rate is too high compared to the diffusion, most of the gas molecules will be consumed at the surface and cannot reach the inner oxide grains, leaving them unutilized for gas sensing.[49] The penetration depth of the target gas into the sensing material can predict how the response of the sensor depends on the microstructure of the sensing material as well as the properties of the target gas. The gas concentration inside a film decreases with increase in depth due to surface reaction. If the concentration of adsorption sites available for the target gases is high, there will be a significant change in the resistance of the metal oxide and hence the gas response will be improved. The utility factor depends on the porosity, thickness of the sensing film, grain size, operating temperature of the gas sensor etc.

The performance of a metal oxide gas sensor can be analyzed by defining certain parameters. The typical response curve of a chemiresistive gas sensor is schematically shown in figure 1.9.

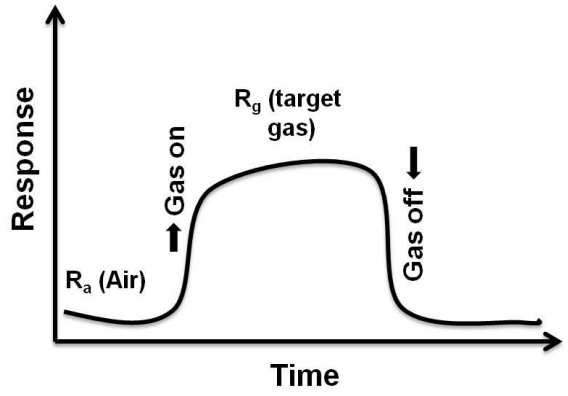

Figure 1.9. The typical response curve of a chemiresistive gas sensor.

The response curve of a gas sensor is characterized by the following parameters.

1. Response: The response $'S'$ is defined as the ratio of the change in resistance of the sensor to the resistance in ambient air.

$$S = \frac{R_g - R_a}{R_a} \tag{1.1}$$

Usually, the gas adsorption on a surface can be empirically represented as

$$S = 1 + aC^b \tag{1.2}$$

where $'C'$ is the gas concentration, $'a'$ and $'b'$ are constants.

$$\log(S-1) = \log(a) + b\log(C) \tag{1.3}$$

It can be seen from the above equation that $\log(S-1)$ has a linear relation with $\log(C)$ with slope $'b'$. The $'b'$ value which represents the charge state of adsorbed oxygen ion species on the surface of the metal oxide can be obtained from the slope of a plot between $\log(S-1)$ and $\log(C)$.

2. Selectivity: It is the ability of the sensor to respond to a particular gas in a mixture of gases. It can be expressed in terms of selectivity coefficient. The selectivity coefficient of a gas $'X'$ to another gas $'Y'$ can be written as

$$Q_X = \frac{S_X}{S_Y} \tag{1.4}$$

where $S_X \; and \; S_Y$ are sensitivities of the sensor to $'X'$ and $'Y'$ respectively.

3. Stability: It is the ability of a sensor to provide reproducible results for a period of time which means retaining the sensitivity, selectivity, response time and recovery time after repeated use.

4. Response time: Response time can be defined as the time taken for the sensor to reach 90% of the maximum response.

5. Recovery time: It is the time taken for the sensor to reach 10% of the maximum response. A good sensor should have small values of response and recovery time so that it can be used for practical applications.

6. Detection limit: It can be defined as the lowest value of the gas concentration which can be detected by the sensor.

7. Dynamic range: It is the capability of the sensor to respond to a wide range of target gas concentrations.

1.2.4 Sensor response formula for chemiresistive gas sensors

Every gas sensor has an optimum operating temperature and the adsorption of oxygen depends on the working temperature.[50] At lower temperatures (< 150°C), oxygen molecules get adsorbed on the metal oxide surface by withdrawing electrons and form molecular oxygen ions.

$$O_{2(gas)} + e^- \leftrightarrow O_{2\,(ads)}^- \tag{1.5}$$

At high temperatures (> 150°C), oxygen ion molecules are dissociated into atomic oxygen ions with singly or doubly negative electric charge following the equations

$$\frac{1}{2}O_2 + e^- \overset{k_{Oxy}}{\Longleftrightarrow} O_{(ads)}^- \tag{1.6}$$

$$\frac{1}{2}O_2 + 2e^- \overset{k_{oxy}}{\Longleftrightarrow} O_{(ads)}^{2-} \tag{1.7}$$

k_{oxy} is the reaction rate constant.

The chemical reaction between a gas molecule and oxygen can be generally written as

$$X + O^{b^-}_{(ads)} \rightarrow X' + be^- \tag{1.8}$$

X and X' are target gas and out gas, b is the number of electrons and k_{gas} is the reaction rate constant.

The rate equation for electron density 'n' can be written as

$$\frac{dn}{dt} = k_{gas}[O_{ads}]^b\,[X]^b \tag{1.9}$$

Where

$$k_{gas} = Aexp\left(-E_a/k_BT\right) \tag{1.10}$$

$'E_a'$ is the activation energy of a reaction, $'k_B'$ is the Boltzmann constant and $'T'$ is absolute temperature.

Integrating equation (1.9), we will get

$$n = \Gamma_t\, k_{gas}[O_{ads}]^b\,[X]^b + n_0 \tag{1.11}$$

$'\Gamma_t\,'$is a time constant, $'n_0'$ is the carrier concentration in air ambient.

The carrier concentration $'n'$ is defined as

$$n = \frac{\alpha}{R} \tag{1.12}$$

$'\alpha'$ is the proportionality constant and $'R'$ is the resistance.

Substituting equation (1.12) in (1.11)

$$\frac{1}{R_g} = \frac{\Gamma_t\, k_{gas}[O_{ads}]^b\, [X]^b}{\alpha} + \frac{1}{R_a} \tag{1.13}$$

Using equations (1.1) and (1.13) the response S can be written as

$$S = \frac{\Gamma_t\, k_{gas}[O_{ads}]^b\, [X]^b}{n_0} + 1 \tag{1.14}$$

From the equation (1.14), the response is directly proportional to rate constant k_{gas} and inversely proportional to electron density n_0 of the intrinsic material. These two factors compete for each other and maximum response is obtained at the optimum temperature. The equation (1.14) works well for thin films and bulk materials. In order to use the equation in case of nanostructures, the effect of surface to volume ratio and depletion layer width has to be taken into account.

i) Surface to volume ratio

The surface to volume ratio in terms of adsorbed oxygen ions can be written as

$$[O_{ads}] = \frac{\sigma_0 \emptyset V_m}{V_s} \tag{1.15}$$

where $'\sigma_0'$ is number of oxygen ion per unit area,$'\emptyset'$ is a ratio of surface area per volume of material $'V_m'$, and $'V_s'$ is the system volume. Substituting in equation (1.15) in (1.14)

$$S = \frac{\Gamma_t \, k_{gas} \left(\sigma_0 \emptyset \left({}^{V_m}/_{V_s} \right) X \right)^b}{n_0} + 1 \tag{1.16}$$

Now the response depends directly on the surface to volume ratio which is well suited for sensors based on metal oxide nanomaterials.

ii) Depletion layer width

According to depletion layer or space charge model,[51] the Debye length L_D which is a characteristic length for semiconductors can be written as

$$L_D = \left(\frac{\epsilon k_B \, T}{q^2 \; n} \right)^{1/2} \tag{1.17}$$

where 'ε' is the static dielectric constant, 'q' is the electrical charge of the carrier, and 'n' is the carrier concentration. Debye length is a measure of the distance over which a charge imbalance is neutralized by majority charge carriers under steady-state or equilibrium conditions.[52] From the equation (1.17) it is seen that if the temperature is kept constant, L_D depends only on the carrier concentration. Let us assume that the sensing material is in the shape of a cylinder with diameter D whose conducting channel is along the axis of the cylinder. In air ambient, depletion layer is formed on the surface due to oxygen adsorption. The width of the depletion layer decreases upon adsorbing a reducing gas. The carrier concentration of the depletion region n' in terms of Debye length can be written as

$$n' = n_0 \frac{\pi(D - 2L_D)^2}{\pi D^2} \tag{1.18}$$

Now the response can be written as

$$S = \left[\frac{\Gamma_t \, k_{gas} \left(\sigma_0 \emptyset \left({V_m}/{V_s} \right) \right)^b}{n_0} \right] \frac{D^2 X^b}{(D - 2L_D)^2} + 1 \tag{1.19}$$

Case I: if D>>$2L_D$

When the depletion layer thickness is very small compared to the diameter of the cylinder, the depletion layer has no effect on the sensor response similar to the case of bulk materials and the equation (1.19) can be approximated to (1.14).

Case II: If D>$2L_D$

Here also the depletion layer has no significant effect on the response. But the sensor response will be higher compared to the previous case because of the increased oxygen ion density due to large surface to volume ratio.

Case III: If D~$2L_D$

In this case, the depletion layer strongly affects the sensor response. Thus the equation (1.19) can be used for evaluating the response of metal oxides having any size variations.

1.2.5 Factors improving the performance of semiconductor gas sensors

The performance of a semiconductor gas sensor can be improved by controlling the factors affecting its receptor and transducer functions.[47] The introduction of foreign particles or additives on the surface of sensor material can modify its receptor function. The foreign material can remarkably improve the sensing characteristics especially the selectivity of a gas sensor. The additives can be either noble metals like Pd, Pt, Au, Ag etc. or oxides of metals such as CuO, TiO_2, SnO_2 etc. The transducer function mainly depends on the particle size and width of the depletion region.[53] As the particle size decreases the specific surface area increases resulting in a large number of active adsorption sites for gas adsorption and consequently a high sensitivity can be observed. The sensitivity drastically increases when the particle size D become approximately equal to $2L_D$ where L_D is the Debye length. The use of small particles for gas sensor fabrication effectively reduce the size of the whole device maintaining the high sensitivity.[54]

The surface modification of metal oxide sensors using additives form heterojunctions. The physical interface between two different materials can be called as a heterojunction and the combination of multiple heterojunctions together in a device is called a heterostructure. One of the most promising heterostructure classes includes the formation of quasi one dimensional (1D) nanostructures decorated with another material. Even though nanoparticles possess high surface to volume ratio, 1D nanostructures are more suitable for developing gas sensors. A large number of grain boundaries in nanoparticles contribute maximum

resistance to the device. Also, these grain boundaries act as scattering centers prohibiting the directional flow of charge carriers.[55] The advantage of using 1D structure for developing gas sensors is due to the fact that they possess a reduced number of grain boundaries and can be used as a suitable host material for the growth of secondary material. The commonly used heterostructures (figure 1.10) are formed by the (a) attachment of spherical nanoparticles on the surface of 1D structures, (b) 1D structures radially grown from the host, form a brush-like structure and (c) core-shell structure.

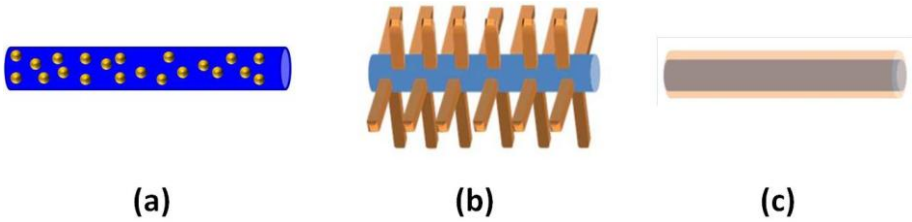

Figure 1.10. Schematic of different heterostructures.

1.2.6 Sensing mechanism of heterostructures

The electrons diffuse from the material having a lower work function to that having higher work function when there is a difference in work function between the materials forming a junction, until thermal equilibrium is reached.[56] This leads to the formation of a depletion region and a potential barrier at the interface. The target gas molecule reacts readily with one material and the reaction byproduct may react with the second material to complete the reaction, referred to as a synergistic reaction. The above-mentioned effects can be amplified by the use of nano-heterostructures because of their small size and high surface to

volume ratio. The improvement in sensing performance of these composites have been attributed to many factors, including electronic effects[57–59] such as band bending due to Fermi level equilibration, charge carrier separation, depletion layer manipulation and increased interfacial potential barrier energy. The chemical effects[60,61] such as a decrease in activation energy, targeted catalytic activity and synergistic surface reactions; and geometrical effects[62,63] such as grain refinement, surface area enhancement, and increased gas accessibility also leads to the improvement in sensing. The above mentioned Fermi level equilibration is equivalent to electron-hole recombination in the vicinity of a p-n junction (semiconductor/semiconductor junction) called the "Fermi level-mediated charge transfer". In addition to the p-n junction, Schottky junction (metal/semiconductor junction) and n-n junction (semiconductor/semiconductor junction) can also be formed at the interface of heterostructures.[52,64–67]

i) Metal-semiconductor junction

The attachment of metal nanoparticles on the surface of metal oxide semiconductors significantly alters the conductivity as well as the active surface area of the whole structure. The terminology “Schottky barrier” is a potential energy barrier for electrons formed at a metal-semiconductor interface that is often referred to as Schottky junction. The barrier height,Φ_B, after contact is given by

$$\Phi_B = \Phi_m - \chi_s \tag{1.20}$$

In figure 1.11, Φ_m and ϕ_s are the work functions of the metal and semiconductor and χ_s is the electron affinity of the semiconductor. In the case of an n-type semiconductor, the contact is Schottky when $\phi_m > \phi_s$, and Ohmic when $\phi_m < \phi_s$. Usually metal-semiconductor junction in Schottky contact facilitates the gas sensing characteristics. In most cases an n-type semiconductor with a suitable metal is chosen because the Fermi level of the metal is lower than the semiconductor, so that electrons flow from the semiconductor to the metal until the Fermi levels have equilibrated and the corresponding band diagram is shown in the figure 1.11.

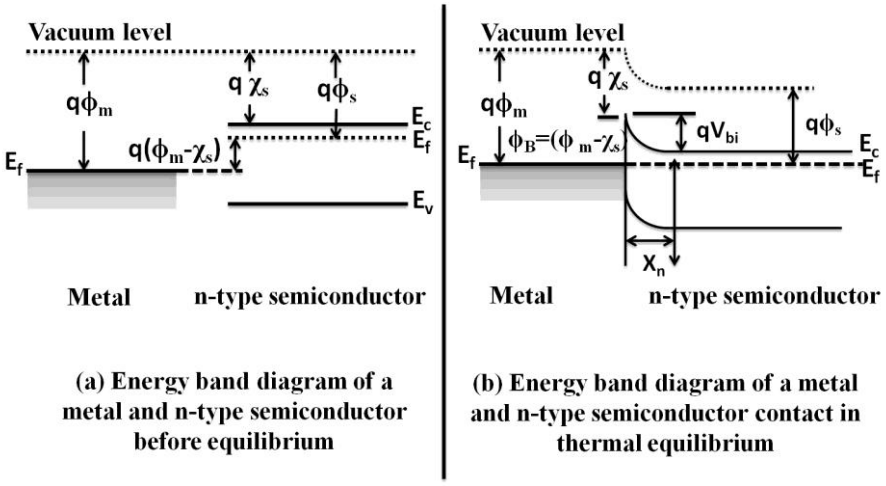

Figure 1.11. Schematic diagram showing the possible band structures at the metal-semiconductor junction (a) before and (b) after thermal equilibrium.

The charge transfer generates a wide depletion region at the interface of metal and semiconductor hence a remarkable increase in the resistance of

the structure can be observed. The width of the depletion region X_n can be calculated as

$$X_n = \left[\frac{2\varepsilon V_{bi}}{qN_n}\right]^{1/2} \tag{1.21}$$

Where V_{bi} is the built in potential at the interface and N_n is the donor concentration in the n-type semiconductor. In addition to the formation of Schottky barrier, most of the metal nanoparticles can act as a catalyst to lower the activation energy for gas adsorption and desorption.[68] The decrease in activation energy significantly lowers the response and recovery time and operating temperature of the gas sensor. The high electron density and catalytic activity of metal nanoparticles dramatically improve the gas sensing performance of the heterostructure.

ii) Semiconductor-semiconductor junctions

p-n junction

Oxide/oxide interfaces especially the formation of a p-n junction (figure 1.12) has significant importance in gas sensing applications. The attachment of a p-type semiconductor on the surface of an n-type material can form junctions at the interface extending the width of the depletion region and decreasing the width of the conduction channel. The depletion layer on n-side, accumulation layer on p- side and junction at the interface together contribute to the increased resistance. The reduced width of the charge conduction channel leads to increase in the total resistance of the heterostructure.

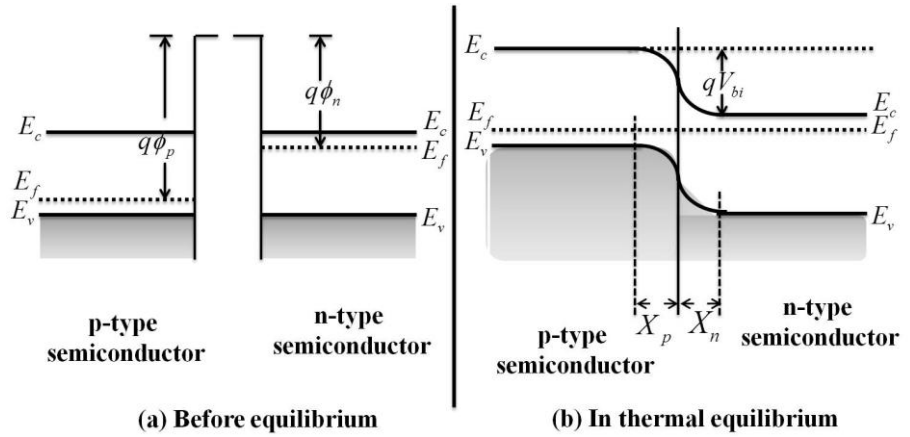

Figure 1.12. Schematic diagram showing the possible band structures at the p-n junction (a) before and (b) after thermal equilibrium.

The width of the depletion layer in n-type and p-type can be written as[69]

$$\chi_n = \left\{\frac{2\epsilon_n V_{bi}}{q}\left[\frac{N_p}{N_n}\right]\left[\frac{1}{N_n + N_p}\right]\right\}^{1/2} \tag{1.22}$$

$$\chi_p = \left\{\frac{2\epsilon_p V_{bi}}{q}\left[\frac{N_n}{N_p}\right]\left[\frac{1}{N_n + N_p}\right]\right\}^{1/2} \tag{1.23}$$

where $'\epsilon_n'$ and $'\epsilon_p'$, are the static dielectric constants and $'N_n'$ and $'N_p'$, are the carrier concentration of n- and p- type semiconductor metal oxide semiconductor respectively. The term $'qV_{bi}'$ equals to the Fermi level difference between the n- and p- type semiconductors. Similar to the case

of metal nanoparticles, the catalytic activity of p-type metal oxide nanoparticles can also used for the selective detection of an analyte gas.

n-n junction

Similar to the formation of p-n junctions, semiconductor-semiconductor can also form n-n junctions at the interface of the two materials. When two n-type materials form a junction, due to the difference in their work functions, migration of electrons takes place from the material having a lower work function to that having higher work function, leading to the formation of an accumulation layer on the latter side. This accumulation layer is further depleted by additional oxygen adsorption from ambient air contributing to enhanced gas sensing performance.[70]

1.3 Material background

1.3.1 Zinc oxide

Zinc oxide (ZnO) is one of the promising II-VI semiconductors with a direct band gap of 3.37 eV and large exciton binding energy (60 meV). ZnO crystallizes in Wurtzite symmetry having a hexagonal unit cell with lattice parameters $a = 0.3242$ nm and $c = 0.5208$ nm at 300K, with a c/a ratio of 1.606, which is close to the 1.633 of an ideal hexagonal close-packed structure. Wurtzite hexagonal ZnO is schematically shown in figure 1.13. The structure is composed of two interpenetrating hexagonal close packed (hcp) sublattices, each of which consists of only one type of atom.[71]

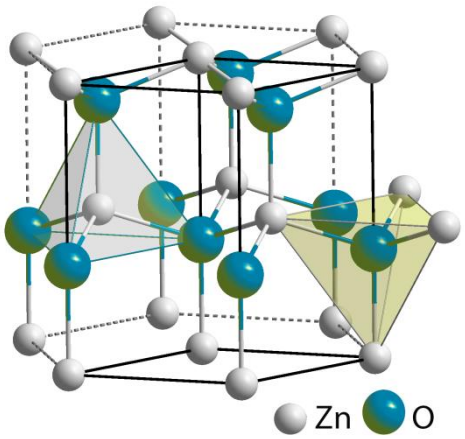

Figure 1.13. Crystal structure of wurtzite hexagonal ZnO.

ZnO is an attractive candidate for several technological applications because of its interesting properties.[72] The potential advantages of ZnO over GaN, such as large exciton binding energy, resistance to radiation damage, high break down strength etc. make ZnO a promising material for fabricating optoelectronic devices like light emitting diodes, laser diodes, photodetectors etc.[73] The presence of various defects in ZnO give rise to strong luminescence in the visible region, hence it is a suitable material for phosphor applications.[15] Due to its high thermal conductivity, ZnO can be used as an additive in rubber to increase the thermal conductivity of tires. The conductivity of ZnO is highly sensitive to the presence of various trace gases in the surrounding ambient hence it can be used for developing efficient gas detecting devices for various applications.[74]

1.3.2 Titanium dioxide

Titanium dioxide (TiO_2) is one of the extensively studied n-type semiconductors due to its broad range of applications such as in photovoltaic,[75,76] photo catalysis,[77,78] lithium ion batteries,[79] photonic crystals[80] etc. TiO_2 exists in three polymorph forms: anatase, rutile, and brookite, where rutile is the thermodynamically most stable phase. Rutile TiO_2 has a tetragonal unit cell, with unit cell parameters $a = b = 4.584$ Å, and $c = 2.953$ Å (figure 1.14). The unit cell consists of TiO_6 octahedra where each Ti^{4+} ion is surrounded by an octahedron of six O^{2-} ions. Each octahedron shares corners with eight neighbors and shares edge with two other neighbors, forming a linear chain.

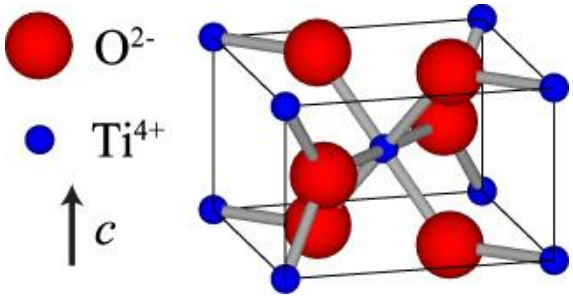

Figure 1.14. Crystal structure of rutile TiO_2.

Being a good photocatalyst, TiO_2 can solve several serious environmental and pollution related challenges.[78] Also, TiO_2 can address the issues related to energy crisis through the effective utilization of solar energy based on photovoltaic devices.[81] TiO_2 is stable, nontoxic and photostable in solutions. A semiconductor becomes an efficient photocatalyst when the redox potential of the charge couple (electron/hole) lies within the band gap domain of the photocatalyst. The photoinduced charge transfer between the semiconductor and the

adsorbed molecules is governed by the band energy positions of the semiconductor and the redox potential of the adsorbate.[82,83] Apart from this, an ideal photocatalyst should be easy to synthesize and use, cost-effective, nonhazardous to living organisms and environment and effectively activated by solar radiation to catalyze the reaction. Compared to other semiconducting materials, TiO_2 possess all the above-mentioned characteristics making it an effective photocatalyst. TiO_2 is a preferred n-type semiconductor for fabricating dye-sensitized solar cells because its conduction band edge lies slightly below the excited state energy level of many commonly used dyes so that effective electron injection takes place between the dye and the semiconductor. O'Regan and Gratzel developed the first dye-sensitized solar cell in 1991 using porous thick film of TiO_2 nanoparticles coated with a monolayer of charge transfer dye.[84] The energy produced by the photovoltaic cells must be used immediately or stored in some form. Hydrogen is considered as a promising source of renewable energy since the discovery of photocatalytic hydrogen generation on TiO_2 electrodes by Honda and Fujishima in 1972.[85] Even though TiO_2 is a potential candidate for photocatalytic and photovoltaic applications, it is equally good for developing efficient gas sensors because its electrical properties can be markedly affected by the changes in surrounding atmosphere. TiO_2 is particularly attractive for gas sensor applications because of its lower cross-sensitivity to humidity.

1.4 Review on ZnO and TiO_2 based room temperature gas sensors

The gas sensing performance is largely dependent on the operating temperature of the sensor which actually controls the reaction kinetics. Generally, oxide based gas sensors operate at temperatures above 150°C

adversely limiting its wide applications. The current trend in the gas sensor industry is the development of room temperature gas sensors which essentially reduce the power consumption, minimize the device configuration, provide long-term stability etc. of the device. Surface modification, additive doping, UV or visible light illuminations etc. are some important strategies which can be employed to reduce the operating temperature of oxide-based gas sensors. Table 1.1 shows the sensing properties of some reported TiO_2 and ZnO based sensors.

Table 1.1. Gas sensing properties of some ZnO and TiO_2 based sensors.

Material	**Operating Temperature (°C)**	**Gas, Concentration (ppm)**	**Respons e**	**Ref.**
TiO_2-SnO_2	320	Ethanol, 50	86[c]	[25]
TiO_2-ZnO	150	Ethanol, 25	10.54[a]	[70]
ZnO/CuO	300	Carbon monoxide, 300	7.6[a]	[86]
ZnO/Au	300	Ethanol, 1000	222[a]	[42]
ZnO/CuO	200	Hydrogen sulfide, 5	83.84[a]	[87]
ZnO/CuO	RT	Ethanol, 200	3.3[a]	[88]
ZnO/CuO	300	Ethanol, 100	98.8[a]	[89]
ZnO/Al:ZnO	RT	Ethanol, 300	0.94[c]	[90]
Ag-TiO_2	200	Ethanol, 500	46.15[a]	[91]
Ag-TiO_2	350	Ethanol, 1000	41.7[a]	[92]
Ag-TiO_2	350	Ethanol, 400	28[a]	[93]
Co_3O_4/TiO_2	115	Xylene, 50	113[b]	[94]
SnO_2/Co_3O_4	135	Acetone, 10	2.72[b]	[95]
TiO_2/ Co_3O_4	160	Ethanol, 100	65[b]	[96]

[a]:$S = \frac{R_a}{R_g}$; [b]:$S = \frac{R_g}{R_a}$; [c]:$S = \frac{\Delta R}{R_g}$; RT: Room temperature

1.5 Applications of chemiresistive gas sensors

Chemiresistive gas sensors have widespread applications in industries, environment monitoring, space stations, military environments, breath analysis etc. A good sensor should have

- high value of response
- high selectivity
- low values for response and recovery time
- lower operating temperature
- reduced power consumption
- high stability etc.

Some of the important applications of gas sensors are listed below.

1.5.1 Environment monitoring

Indoor and outdoor air quality monitoring is important for the well being of humanity as well as other living organisms. Emissions from automobiles, industries etc. contain several toxic gases harmful to health. Table 1.2 shows the exposure limit of certain poisonous gases. These gases have short term as well long-term impacts on human health. For example, even though the threshold limit is 10 ppm for hydrogen sulfide, after 3 to 7 minutes of exposure, the person loses the sense of smell and the gas cause eye and throat damage. With higher concentrations, severe health and even lethal consequences may happen. Metal oxide based gas

sensors can be used to detect the presence of common poisonous gases emitted from various sources.

Table 1.2. Toxicity limit of certain poisonous gases

Sl. No.	**Chemical**	**Toxicity limit (ppm)**
1	Ammonia	25 ppm
2	Hydrogen sulfide	10 ppm
3	Benzene	0.5 ppm
4	Carbon monoxide	25 ppm
5	Carbon dioxide	5000 ppm
6	Chlorine	0.5 ppm
7	Nitrous oxide	50 ppm
8	Nitrogen dioxide	3 ppm
9	Gasoline	300 ppm
10	Diesel fumes	15 ppm

1.5.2 Exhaled breath analysis

Metal oxide based gas sensors can be used as biomarkers for disease diagnosis. The concentrations of component gases in ones exhaled breath is in correlation with specific diseases. Hydrogen sulfide, acetone, toluene, ammonia, and nitrogen monoxide etc. have strong relationships with halitosis, diabetes, lung cancer, kidney diseases, asthma etc.[86] The concentration of acetone in the exhaled breath of a healthy person is not expected to exceed 900 ppb and if the concentration is 3 ppm or above, the person may have diabetes. Halitosis is commonly called bad breath

where unpleasant odor presents in the exhaled breath due to the presence of gases like hydrogen sulfide, dimethyl sulfide etc. For healthy people, the concentration of these gases in the exhaled breath is less than 150 ppb while in patients the value can exceed around 1 ppm. Metal oxide gas sensors having low detection limit can be used for detecting the presence of component gases in the exhaled breath.

1.6 Limitations of chemiresistive gas sensors

For most of the practical applications, the main issue is not only to estimate the target gas concentration, but also to identify a particular gas in a mixture of gases. Metal oxide based gas sensors have a high value of response to various gases, but their selectivity is poor. Selectivity of a sensor is its capability to distinguish a particular gas from a mixture of gases. Selectivity can be improved by using an array of sensors each having an individual response to all the gases in the mixture similar to the case of electronic nose or E-nose. Electronic sensing refers to the capability of reproducing human senses using sensor arrays and pattern recognition system.

Chapter 2

Synthesis techniques and characterization tools

This chapter describes the synthesis methods and characterization tools used in the present thesis. Hydrothermal and wet chemical methods have been used for growing one-dimensional nanorods and hierarchical structures. The as grown samples were characterized using different characterization techniques like XRD, TEM, micro Raman, FESEM and semiconductor characterization system. For gas sensing measurements, we have fabricated an in house experimental set up.

2.1 Synthesis of metal oxide nanostructures

Metal oxide semiconductors such as ZnO, SnO_2, TiO_2, WO_3 etc. are already established in the field of gas sensor industry. These materials

with specific morphology and dimension can be easily synthesized by physical as well as chemical methods. Commonly used methods are listed in figure 2.1. Chemical methods are much more suitable for synthesizing oxide nanostructures having various dimensionalities and morphology. The general approaches for the synthesis of nanomaterials are top-down and bottom-up.[87,88]

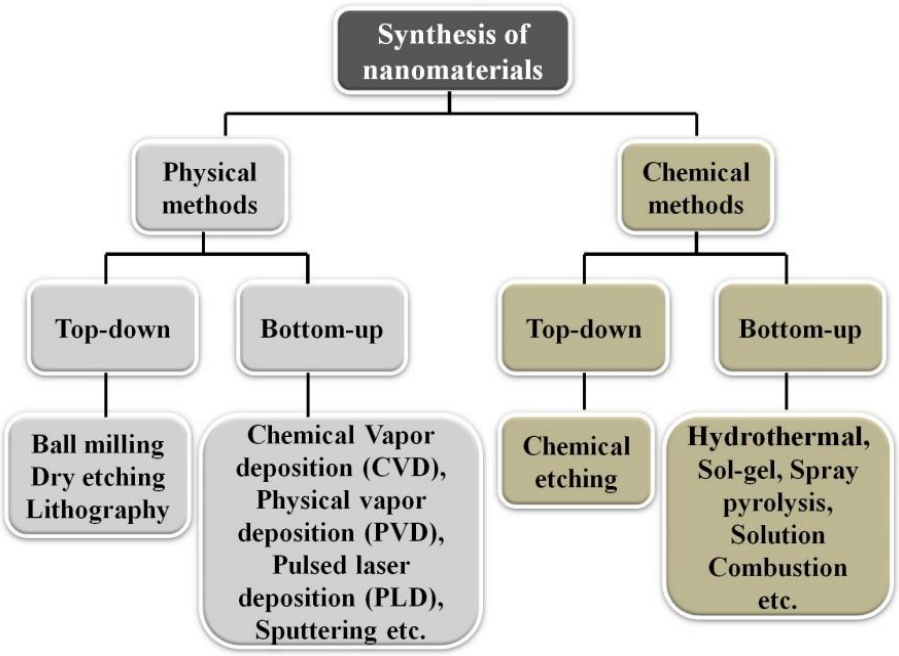

Figure 2.1. Methods for the synthesis of nanomaterials.

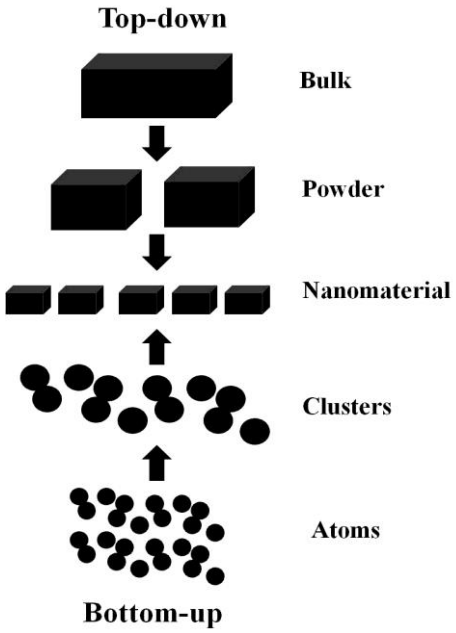

Figure 2.2. Schematic representation of top-down and bottom-up approaches.

Top-down approaches start with particles or patterns on a larger scale which can be reduced to nanoscale whereas bottom-up approaches start with atoms, molecules combined to form nanostructures as shown in figure 2.2. Compared to top-down approaches, bottom-up approaches are much less expensive and more suitable for large scale production of nanomaterials. Among the synthesis methods listed in figure 2.1, solution based bottom-up techniques are easy to implement and widely accepted for the synthesis of nanomaterials. Sol-gel, hydrothermal, solution combustion etc. can be used for the synthesis of nanomaterials with desired size and shape depending on the applications in a relatively cheap way. The sol-gel method is a versatile technology involves the evolution

of inorganic networks through the formation of a colloidal suspension (sol) and gelation of the sol to form a network in a continuous liquid phase (gel). The reactions involved in sol-gel processes are hydrolysis and condensation of the precursor solutions. The rate of hydrolysis and condensation reactions is governed by various factors such as pH, temperature, concentration etc. Solution combustion synthesis is a self-sustained thermal process where the heat for the reaction comes from the combustion of reactants.[89] The process starts with dehydration and thermal decomposition of the homogeneous solution and involves several thermally coupled exothermic reactions resulting in the formation of solid product and gas.

Of the methods like sol-gel, solvothermal, solution combustion etc. utilized in metal oxide nanostructure synthesis, hydrothermal/solvothermal processes have emerged as a powerful method for controlled synthesis of nano-morphologies. The term hydrothermal is purely of geological origin. It was first used by the British Geologist, Sir Roderick Murchison (1792–1871),[90,91] to describe the action of water at elevated temperature and pressure in bringing about changes in the earth's crust leading to the formation of various rocks and minerals. The flexibility and reliability of this synthesis approach is demonstrated here for the transformation of transition-metal oxides into high-quality anisotropic nanomaterials.

The hydrothermal technique has been widely studied and employed in inorganic synthesis for many years. The term hydrothermal usually refers to any heterogeneous reaction in the presence of aqueous solvents or mineralizes under high pressure and temperature conditions to

dissolve and recrystallize materials that are relatively insoluble under ordinary conditions. The hydrothermal technique has found its place in several branches of science and technology because of reduced contamination and low synthesis temperature. In hydrothermal synthesis, the solid is first dissolved completely and then precipitated again excluding any kind of topotactic reaction. The advantages of hydrothermal technique compared to other techniques for sample preparation are listed below:

- Samples can be grown in powder form or on the surface of rigid as well as flexible substrates
- Particles of desired size and shape can be easily synthesized by varying hydrothermal temperature and reaction time
- Chemical composition and stoichiometry of the material can be maintained.
- Samples do not need milling and calcination

Crystal growth or materials processing under hydrothermal conditions requires a pressure vessel capable of containing corrosive solvent at high temperature and pressure. For a typical hydrothermal reaction, apparatus, called either “autoclaves” or “bombs”, are used. To prevent corrosion of the internal cavity of the autoclave, protective inserts like teflon, quartz, glass etc. are generally used depending on the temperature and nature of the precursor solution.

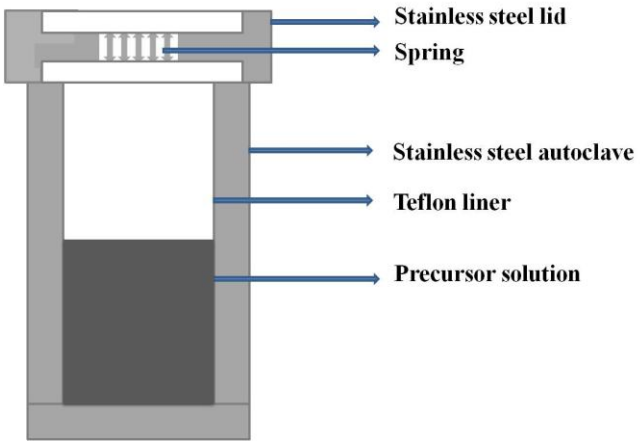

Figure 2.3. Schematic diagram of a typical laboratory autoclave.

An ideal hydrothermal autoclave should have the following characteristics:

- It should be inert to acids, bases, and oxidizing agents.
- Assembling and disassembling must be easy.
- Should have sufficient length to obtain the desired temperature gradient.
- Should be leak-proof with unlimited capabilities to the required temperature and pressure.
- Rugged enough to bear high pressure and temperature of experiments for long duration, so that no machining or treatment is needed after each experimental run.

2.2 Characterization tools

This section briefly discusses the various characterization tools used in the present study. The structural properties of all the samples were investigated using X-ray diffraction, transmission electron microscopy, and micro Raman analysis. Field emission scanning electron microscopy was used for morphological characterization of the nanostructures. UV-Visible spectrophotometer was used for optical studies. Electrical characterization was carried for investigating the junction characteristics of the heterojunction samples. For gas sensing measurements, an in-house experimental set up has been fabricated.

2.2.1 Structural characterization

i) X-ray diffraction

X-ray diffraction is a tool not only for structural investigation, but also can be implemented for stress measurements, calculation of particle size, and determination of orientation etc. of materials. In 1912, the German physicist Max von Laue suggested that if crystals were composed of regularly spaced atoms and the wavelength of X-rays is approximately equal to the interatomic distance in crystals, then the crystal can diffract X-rays. Later, the English physicists, W. H. Bragg and his son W. L. Bragg analyzed Laue's experiment in detail and mathematically expressed the necessary conditions for diffraction. Since the atoms are arranged periodically in the lattice, the rays scattered by them have definite phase relationships between them. The phase relations are in such a way that destructive interference takes place in most directions of scattering and

constructive interference takes place in few directions forming diffracted beams. The two important geometric facts to be considered while dealing with Bragg's law are

i. The incident beam, the normal to the reflecting plane, and the diffracted beam are always coplanar.

ii. The diffraction angle, which is the angle between the diffracted beam and transmitted beam is always 2θ.

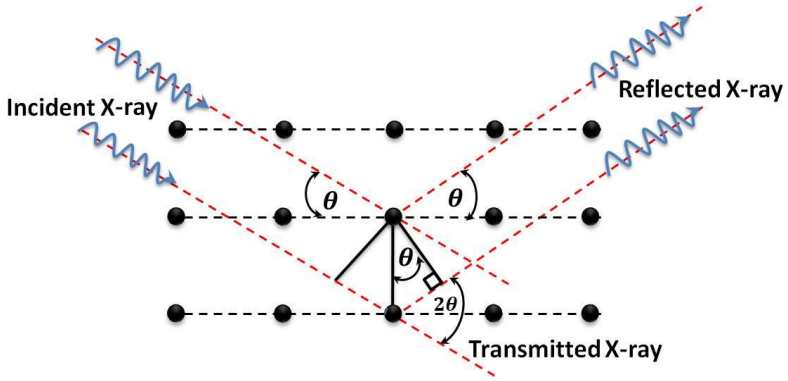

Figure 2.4. Bragg diffraction from a set of crystal planes.

The Bragg's diffraction from a set of crystal planes is shown in figure 2.4. The diffraction of monochromatic X-rays takes place only at those particular angles of incidence which satisfy the Bragg's law. Bragg's law can be mathematically expressed as

$$n\lambda = 2d \sin\theta \qquad (2.1)$$

where 'λ' is the wavelength of the radiation used, 'd' is the interplanar spacing, 'θ' is the angle between diffracted beam and the relevant crystal

plane and 'n' is the order which is often unity. By measuring the angle 'θ', the interplanar spacing 'd' can be calculated, provided the wavelength of X-ray is known. In the present work, the crystal phase and crystallinity of the samples were investigated by glancing angle X-ray diffraction taken using PANalytical X'pert PRO high-resolution X-ray diffractometer (HRXRD) with CuKα (λ=1.5418 Å).

ii) Transmission electron microscopy

Transmission electron microscopy (TEM) is a microscopy technique in which a beam of high energy electrons is transmitted through a specimen to form an image. When electron beam passes through a thin section of the specimen material, it interacts with atoms of the specimen and are scattered. A sophisticated system of electromagnetic lenses focuses the scattered electrons into an image or a diffraction pattern depending on the mode of operation. Figure 2.5 shows the path of the electron beam in a transmission electron microscope. In TEM, the diffraction pattern obtained from a selected area of the specimen offers a unique capability to determine the lattice parameter and crystal symmetry, and this mode of operation is called selected area electron diffraction pattern (SAED). The 'd' spacing of the planes corresponding to the rings in the SAED pattern can be determined by the following equation

$$Rd = L\lambda \tag{2.2}$$

Where L is the effective camera length, λ is the de Broglie wavelength of the accelerating electrons, R is the ring radius of a standard electron diffraction pattern, and d is the interplanar spacing. In the present study,

the detailed microstructure of the samples was analyzed using JEM2100 transmission electron microscopy (TEM) measurements.

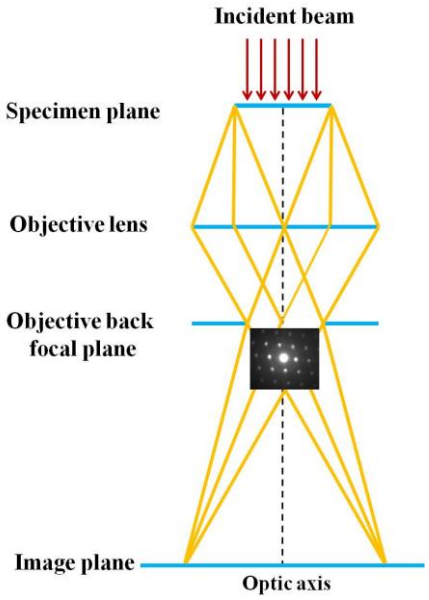

Figure 2.5. Schematic diagram showing the path of the electron beam in transmission electron microscope.

iii) Raman spectroscopy

Raman spectroscopy was named in honor of its inventor Sir C.V Raman along with K.S Krishnan. It is a spectroscopic technique based on the inelastic scattering of monochromatic light, usually from a laser source. The incident photons from the laser source interact with the vibrating molecules of the sample and originate a scattered light. The frequency of the scattered photons is shifted up or down in comparison with the frequency of the incident radiation and this shift in frequency

gives information about the vibrational, rotational and other low frequency transitions within the molecule.[92]

When a monochromatic radiation of frequency 'υ_0' is incident on a non-absorbing medium, most of the radiation is transmitted without any change, and some of it is scattered. If we analyze the scattered radiations, a small portion of the scattered energy will be found at frequencies $\vartheta' = \vartheta_0 \pm \vartheta_m$.[93] The displaced frequencies are associated with the transitions between vibrational, rotational, and electronic levels of the molecular systems. The scattering of radiation without change of frequencies is called Rayleigh scattering and scattering of radiation with change in the frequency is called Raman scattering. Raman scattering is always accompanied by Rayleigh scattering. Raman lines at wave numbers less than the incident wave number $(\vartheta_0 - \vartheta_m)$ are known as Stokes lines, and those with wave numbers greater than ϑ_0, $(\vartheta_0 + \vartheta_m)$ are called anti- Stokes lines. The frequency shifts of the Raman lines, their intensity and polarization are characteristics of the scattering substance. Usually, Stokes lines are monitored for analysis because anti-Stokes lines are much weaker than Stokes lines. The levels involved in the Raman spectra are shown in figure 2.6. In the present work, room temperature Raman studies were carried out using Lab RAM HR spectrophotometer (HORIBA JOBIN YVON) with an Ar^+ laser (514 nm) as the excitation source.

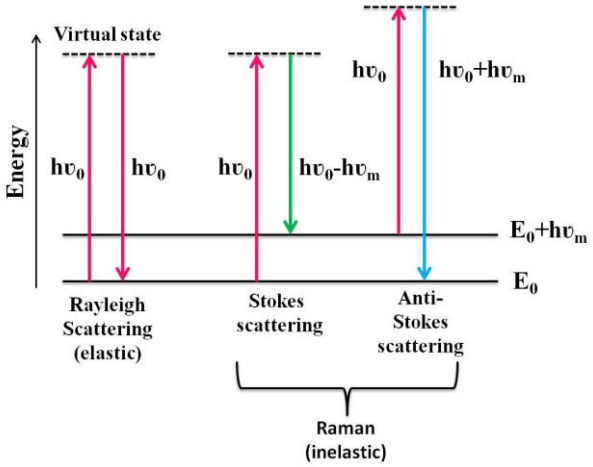

Figure 2.6. Simplified Jablonski diagram of Rayleigh process, Stokes process and anti-Stokes process.

2.2.2 Morphological characterization

Field emission scanning electron microscopy

Field emission scanning electron microscopy (FESEM) analysis is an effective technique used for analyzing the surface morphology of the samples. FESEM uses a focused beam of electrons to generate an image. The important components of an FESEM system are electron gun, electronic lenses, scanning coil, specimen sample, and detector. The electron gun generates low as well as high energy electron beams resulting in both improved spatial resolution and minimized sample damage. The generated electrons, called primary electrons are accelerated in a high electric field gradient. The electronic lenses in the system deflect and focus the beam of electrons and produce a narrow beam which

bombards the object resulting in the generation of secondary electrons (SE) from the sample. The detector detects these secondary electrons and produces an electronic signal, finally transformed into an image. The surface morphology of the samples in the present study was analyzed using Carl Zeiss field emission scanning electron microscopy (FESEM).

2.2.3 Optical characterization

UV-Visible absorption spectroscopy

The optical absorption spectroscopy provides information of the semiconductor about the band gap, direct or indirect transitions, etc. Compared to other characterization techniques, optical methods are generally non-destructive and require little or no sample preparation. Optical absorption spectroscopy is based on the principle that if the energy of the incident radiation is equal to or greater than the band gap of the semiconductor, the radiation is completely absorbed. When the energy is less than the band gap of the material, the radiation is transmitted. The observed absorption spectra show a peak when the photon energy is equal to the band gap of the material. The absorption spectra of the synthesized samples were recorded using JASCO V-570 spectrophotometer.

2.2.4 Electrical characterization

The p-n junctions are the building block of many technologically revolutionized devices. Therefore, its characterization is inevitable for the design of junction based devices. Current-voltage (I-V) characterization is an effective method used for analyzing the rectifying nature of a p-n heterojunction. The p-n junction characteristics of the fabricated

heterojunction devices were studied using Keithley 4200 Semiconductor analyzer.

2.3 Fabrication of in-house experimental setup for gas sensing measurements

An in-house experimental set up has been developed in our laboratory for gas sensing studies. The system consists of a stainless steel chamber with rubber tube at its bottom. Inside the chamber, we have a sample holder with two terminals connected in series with a Keithley source measure unit. The schematic of the measurement set up is shown in figure 2.7.

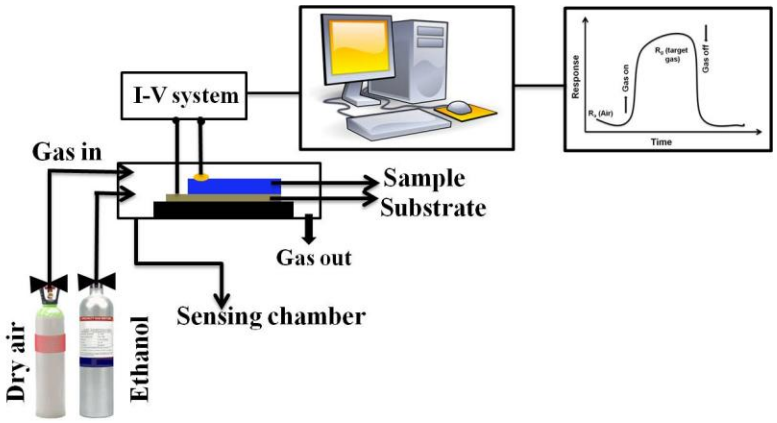

Figure 2.7. Schematic representation of the experimental set up for gas sensing measurements.

Gas sensors were fabricated by depositing circular gold electrodes on the top of the sample. Initially, we measured the current through the device in synthetic air ambient until it attains a stable value. Once it reaches a stable value, various concentrations of the target gas are introduced into the

chamber and the corresponding variation in current has been measured. For all the measurements, commercially available high purity sample gases with moisture content less than 2 ppm have been used, which prevents the effects of humidity on the gas sensing properties. The response 'S' of the sensor can be defined as

$$S = \frac{I_g - I_a}{I_a} = \frac{R_g - R_a}{R_a} = \left|\frac{\Delta R}{R_a}\right| \quad (2.3)$$

where I_g and I_a are the current measured in the presence of gas and in air. We have taken I_a as the average of first 50 values of current measured in air.

Chapter 3

Enhanced room temperature gas sensing properties of low-temperature solution-processed ZnO/CuO heterojunction

In this chapter, room temperature (29°C) ethanol sensor based on vertically aligned ZnO nanorods decorated with CuO nanoparticles was successfully fabricated by simple cost-effective solution processing. The heterojunction sensor exhibited better sensor parameters compared to pristine ZnO. The response of the heterojunction sensor to 50 ppm ethanol is, at least, 2-fold higher than the response of the ZnO bare sensor. Also the response and recovery time of ZnO/CuO sensor to 50 ppm ethanol are 9 and 420 seconds whereas the values are 16 and 510 seconds, respectively for ZnO sensor. In addition to ethanol, the fabricated device has the capability to detect other reducing gases like hydrogen sulfide and ammonia at room temperature.

Enhanced room temperature gas sensing properties of low-temperature solution-processed ZnO/CuO heterojunction", P P Subha and M K Jayaraj, *Chemistry Central Journal* (under review).

3.1 Introduction

Zinc oxide (ZnO) is a wide band gap (3.37 eV) II-VI semiconductor having excellent physical, chemical and electrical properties[72,94] which makes it a promising candidate for various applications like sensors,[95,96] solar cells,[97] spintronics,[98] transparent electronics,[99] catalysis[100] etc. The conductivity of zinc oxide is highly sensitive to the presence of various trace molecules in the atmosphere hence can be used for developing gas detecting devices. The use of nanostructured ZnO is more suitable for fabricating high-performance gas sensors especially because of their high surface to volume ratio. However, to obtain good response characteristics, gas sensors should be fabricated with well aligned crystalline ZnO nanorods with higher density and aspect ratio.[101,102] The seed mediated hydrothermal method is an effective way to grow vertically aligned ZnO nanorods on any substrate surface.[103] Seed layer acts as the nucleation site where zinc nutrients in the precursor solution are consumed in the growth process to produce aligned ZnO nanorods.

There are several methods which can be employed to enhance the gas sensing properties of metal oxide nanostructures. Fabrication of gas sensors based on hierarchical structures is an effective way to improve the sensing performance because hierarchical structures offer several interesting properties favorable for developing high-performance gas sensors.[104] Hierarchical structures can be formed by loading metals[105,106] (Ag, Au, Pd etc.) or metal oxides[58,107] (CuO, NiO, TiO_2 etc.) on the surface of the sensing material under consideration. Researchers have already found the enhanced gas sensing characteristics of metal

oxide/metal oxide hierarchical structures.[58,108,109] The hierarchical structure can form either p-n, n-n or p-p type semiconductor junctions depending on the nature of the material under consideration. p-CuO and n-ZnO can be combined in different ways to utilize the advantages of p-n heterojunction in gas sensor applications. In the present study, we have investigated the gas sensing characteristics of n-ZnO/p-CuO hierarchical structures.

3.2 Experimental

3.2.1 Materials

All the reagents used were analytically pure and used without further purification. Zinc acetate dihydrate (Zn $(CH_3COO)_2$ $2H_2O$), sodium hydroxide (NaOH) and copper acetate hydrate ($Cu(CO_2CH_3)_2H_2O$) were purchased from Fisher scientific. Ammonia solution, isopropyl alcohol, and ethanol were purchased from Merck Millipore. De ionized water was obtained from an ultrafilter system. ITO/glass substrates were purchased from Sigma Aldrich (surface resistivity 15-25 Ω/sq). The substrates were cleaned by standard cleaning procedure.[103]

3.2.2 Synthesis of ZnO nanorods on ITO/glass substrates

A thin layer of ZnO seed layer was deposited by immersing the cleaned ITO/glass substrate in a solution containing zinc acetate (0.025 M) and sodium hydroxide (0.05 M) in 100 ml ethanol. The substrate was immersed in the solution for 5 minutes and the dipping process repeated for 8 times to obtain a uniform ZnO layer over a considerable area of the

substrate. In between each dipping process, the sample was kept at 80°C on a hot plate. The annealing of the substrates at the optimized temperature 250°C in air results in the formation of ZnO nanoparticles. The ITO/glass substrate with ZnO nanoparticle seed layer will act as a lattice matched substrate for the hydrothermal growth of aligned ZnO nanorods. The precursor solution for hydrothermal experiment was prepared by dissolving zinc acetate (0.1 M) and ammonia (25%) in 100 ml de-ionized water. The solution was transferred into a Teflon lined autoclave with the seed layer coated substrate immersed horizontally facing up. Hydrothermal experiments were carried out at the optimized temperature and time; 180°C for 1 hour; in a laboratory oven. After hydrothermal experiment the samples were taken out and sonicated in iso-propyl alcohol for few seconds to remove unaligned nanorods lying over the vertically aligned nanorods.

3.2.3 Deposition of CuO nanoparticles on the surface of ZnO nanorods

CuO nanoparticles were deposited by a wet chemical method. 0.05 M copper acetate solution was prepared in ethanol at room temperature and ZnO sample was immersed in the solution for 1 hour. After deposition sample was annealed at 250°C for 2 hours in air to form ZnO/CuO heterostructure.

3.3 Results and discussion

The growth mechanism of ZnO nanorods depends on the reactant species and crystallographic habits of wurtzite hexagonal ZnO. The growth process of vertically aligned ZnO nanorods is schematically

shown in figure 3.1. $Zn(OH)_2$ nuclei starts to precipitate when the concentration of Zn^{2+} and OH^- in the precursor solution exceeds a critical value. Upon annealing, these $Zn(OH)_2$ are converted into hexagonal ZnO nuclei which act as the seed for the growth of C-axial oriented ZnO nanorods. Wurtzite hexagonal ZnO is a polar crystal which has polar and non-polar faces. In a polar ZnO crystal, zinc and oxygen atoms are stacked alternately along the C-axis in such a way that catalytically active 'Zn' terminated (0001) surface will be at the top and chemically inert 'O' terminated $(000\bar{1})$ surface will be at the bottom. Because of the thermodynamic instability of polar faces, they often undergo rearrangement to minimize their surface energy and also tend to grow more rapidly. Furthermore, the growth depends on the growth velocities of different crystal planes in ZnO. The growth velocity of different crystal planes under hydrothermal conditions can be written in the order of $[0001] > [01\bar{1}\bar{1}] > [01\bar{1}0] > [01\bar{1}1] > [000\bar{1}]$.[110,111] Therefore, ZnO crystal has a strong tendency to grow along $[0001]$ direction or C-axis which ultimately leads to the formation of vertically oriented ZnO nanorods. The chemical reaction between zinc acetate and ammonia is represented by following equation (1)

$$\left.\begin{aligned} Zn(CH_3COO)_2 + NH_4OH \rightarrow Zn(OH)_2 + 2CH_3COONH_4 \\ Zn(OH)_2 \rightarrow ZnO + H_2O \end{aligned}\right\} \quad (1)$$

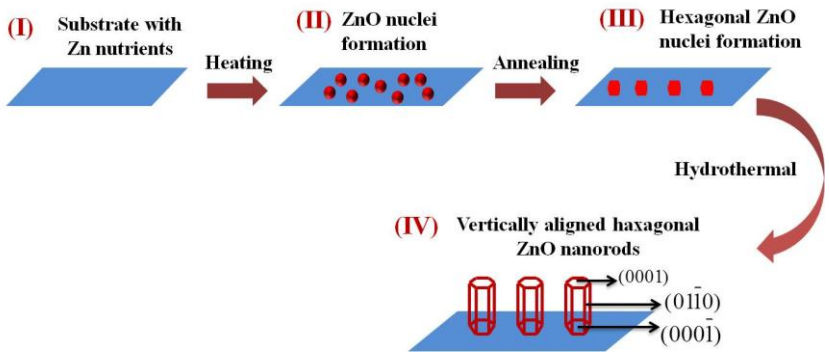

Figure 3.1. Schematic illustration of the possible growth mechanism of vertically aligned ZnO nanorods.

The crystal structure, as well as crystallinity of the samples, was analyzed using high resolution glancing angle X-ray diffraction pattern shown in figure 3.2. The highly dispersed small CuO nanoparticles were not detected in the X-ray diffraction. All the observed diffraction peaks correspond to wurtzite hexagonal ZnO and no peaks corresponding to CuO have been observed in the spectra. The high intensity of the peak along (0002) direction confirms the c-axial growth of ZnO nanorods.

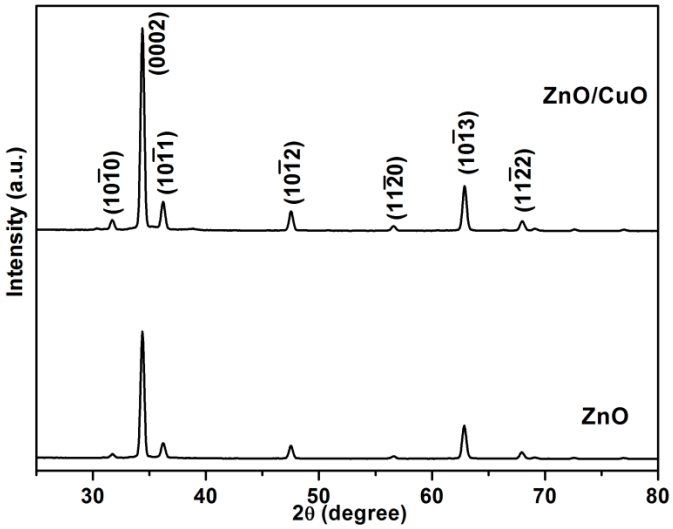

Figure 3.2. Glancing angle X-ray diffraction pattern of ZnO and ZnO/CuO hierarchical structure.

The microstructure of the samples was further analyzed using TEM measurements. The TEM image in figure 3.3(a) shows the one-dimensional morphology of the nanorods and the observed lattice planes in figure 3.3(b) matches with (0002) plane of ZnO with a lattice spacing of 2.6 Å. The CuO nanoparticles can be seen on the surface of ZnO nanorods as depicted in figure 3.3(c) which make the surface of nanorod rough. The presence of bright spots in the SAED pattern in figure 3.3(d) indicates the crystalline nature of ZnO/CuO structure. In addition to (0002), $(10\bar{1}0)$ and $(10\bar{1}1)$ planes of wurtzite hexagonal ZnO, $(\bar{1}\,11)$ lattice plane of monoclinic CuO can be clearly seen in the SAED pattern confirming the formation of ZnO/CuO hierarchical structures.

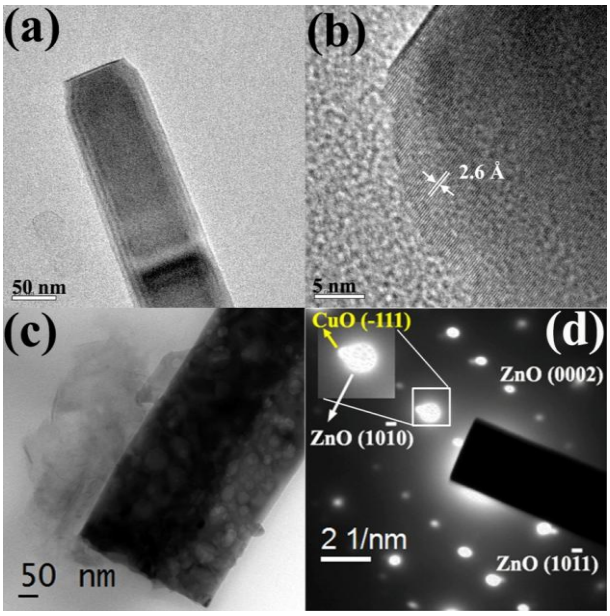

Figure 3.3. (a) TEM and (b) HRTEM images of ZnO nanorod, (c) TEM image and (d) SAED pattern of ZnO/CuO hierarchical structure.

Micro Raman spectroscopy is a nondestructive technique used for analyzing the vibrational properties of materials. Raman spectra of both ZnO and ZnO/CuO are displayed in figure 3.4. All the observed vibrational modes such as E_{2L} (98 cm^{-1}), $A1_{TO}$ (381 cm^{-1}), E_{2H} (437 cm^{-1}), and $E1_{LO}$ (580 cm^{-1}) corresponds to wurtzite hexagonal structure of ZnO. Monoclinic CuO exhibit three Raman active modes ($A_g + 2B_g$) which are assigned respectively at 278 cm^{-1}(A_g), 333 cm^{-1} (B_{1g}) and 620 cm^{-1} (B_{2g}).[112,113] Along with the vibrations of ZnO, A_g mode corresponding to monoclinic CuO has been observed for ZnO/CuO heterostructure. The Raman vibrations of CuO are highly dependent on the method of preparation and this may be the reason for the absence of B_{2g} vibration.

The co-existence of ZnO and CuO Raman modes in the Raman spectra confirms the formation of ZnO/CuO hierarchical structure.

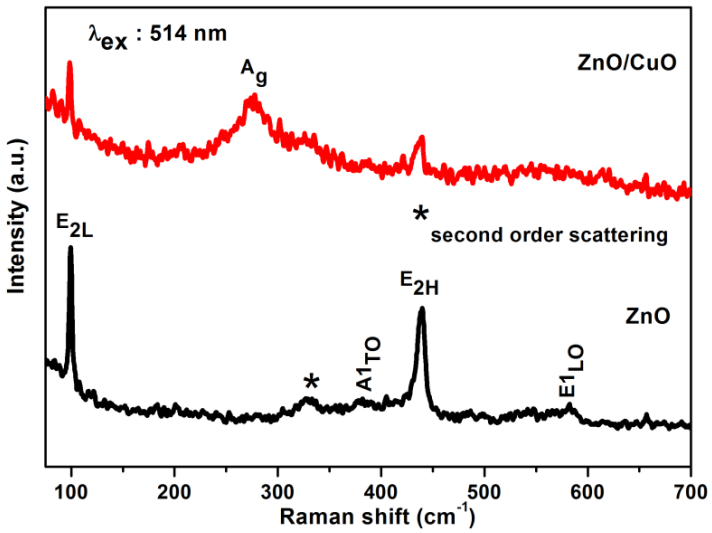

Figure 3.4. Micro Raman spectra of ZnO and ZnO/CuO hierarchical structure.

The surface morphology of all the samples was analyzed using FESEM images shown in figure 3.5. The c-axial growth of nanorods against the substrate surface forms a porous network which makes the gas diffusion in and out easier. The sonication has effectively removed unaligned nanorods lying over the vertically aligned nanorods shown in the inset of figure 3.5(a). The diameter and length of the nanorods are approximately 95 nm and 2 μm respectively. The presence of CuO on ZnO nanorods can be clearly seen in figure 3.5(d). The attachment of CuO increases the interfacial area and correspondingly an enhanced gas sensing behavior can be observed.

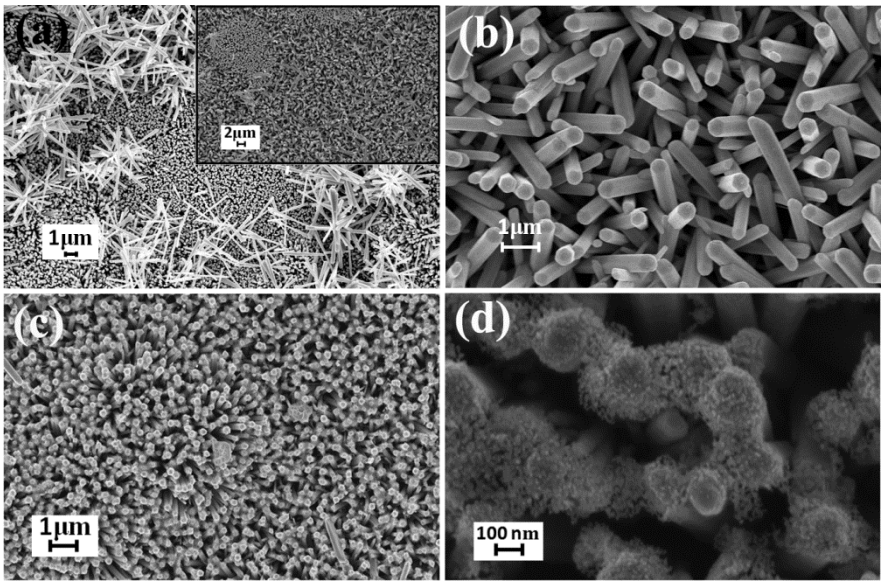

Figure 3.5. FESEM images of a) as grown ZnO nanorods (inset shows the image of the sonicated sample) b) magnified view of the sonicated sample c) CuO attached ZnO nanorods and d) magnified view of ZnO/CuO.

The UV-Visible absorption spectra of ZnO and ZnO/CuO hierarchical structures are shown in figure 3.6. The spectra of pure ZnO nanorods possess an absorption around 370 nm corresponding to the band gap of ZnO whereas the band gap absorption edge gets slightly red-shifted to 374 nm in the case of ZnO/CuO hierarchical structure similar to that observed in the previous reports.[100,114] Also ZnO/CuO sample has a high value of absorbance in the visible region compared to pristine ZnO. These factors confirm the formation of CuO loaded ZnO hierarchical structures.

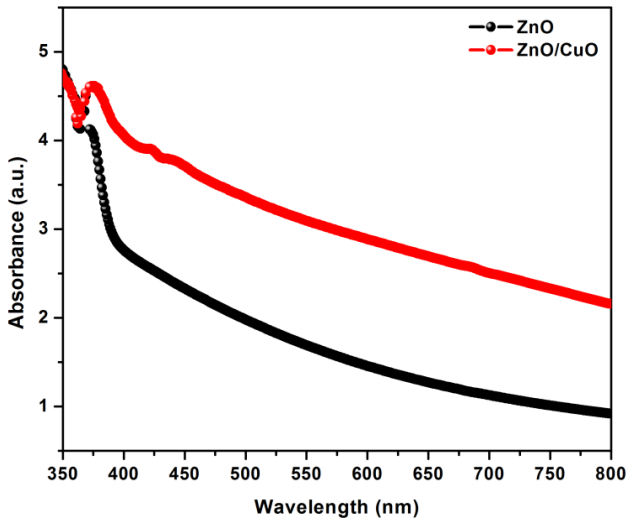

Figure 3.6. UV-Visible absorption spectra of ZnO and ZnO/CuO structures.

The gas response characteristics of the sensors were investigated by applying 1 V to ZnO and 8 V to ZnO/CuO respectively. The room temperature (29°C) ethanol sensing characteristics of ZnO and ZnO/CuO nanostructures were monitored by measuring the change in current upon exposure to different concentrations of the target gas. The response of ZnO and ZnO/CuO to various concentrations of ethanol is shown in figure 3.7. The room temperature response of the sensor increases in ethanol ambient due to the redox reactions taking place between the metal oxide and the target gas. Both ZnO and ZnO/CuO samples exhibit a very good response to ethanol even for 5 ppm concentration at room temperature. The response of both the sensors increases with increase in the concentration of the target gas. Compared to pristine ZnO, ZnO/CuO exhibit improved response values for all the concentrations used in the

present study. The C-axial orientation, as well as the attachment of CuO nanoparticles on ZnO nanorod surface, increase the exposed surface area of the sensor contributing to enhanced sensing characteristics. More importantly, the p-n junctions formed at the interface of n-ZnO and p-CuO significantly improve the gas sensor performance.

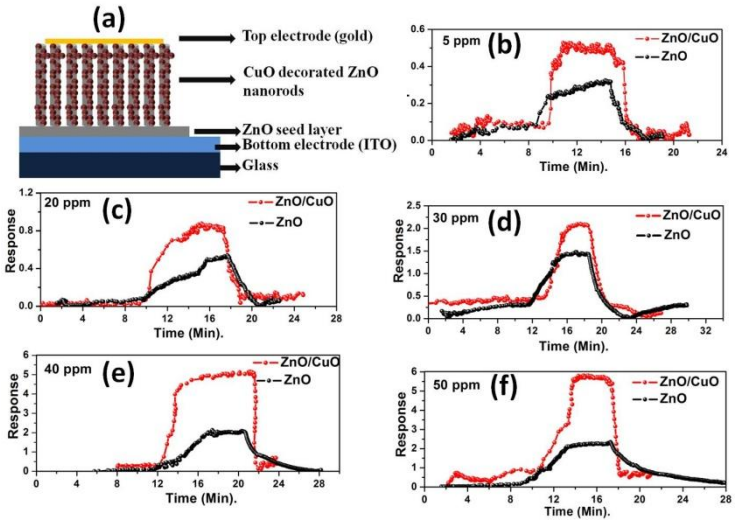

Figure 3.7. Schematic representation of the (a) device structure and (b-f) room temperature ethanol sensing characteristics of ZnO and ZnO/CuO nanostructures for ethanol at various concentrations.

Figure 3.8 shows that the response of ZnO/CuO structure is higher than the response of ZnO for all target gas concentrations. The response and recovery time of the fabricated sensors are depicted in figure 3.9. It can be seen that the response time decreases with increase in concentration whereas the recovery time increases with increase in target gas concentration. This can be attributed to the fact that the number of molecules having minimum required energy for the reaction increases at

high concentrations hence more and more target gas molecules react with adsorbed oxygen ions resulting in a faster change in resistance. Whereas the adsorption takes place slowly at low concentrations due to the lower coverage of gas molecules hence the change in resistance also takes place slowly. The significance of the present work is that even at room temperature both the sensors respond to 5 ppm ethanol gas within less than 100 seconds. For 5 ppm of ethanol, the response time calculated is 98 and 30 seconds for ZnO and ZnO/CuO respectively and almost complete desorption of the target gas takes place especially at lower concentrations within a few minutes. A good sensor should have a high value of response and low value of response time. The complete solution processed p-n heterojunction sensor fabricated in the present study exhibits very good values of gas sensor parameters at room temperature compared to the previous reports.[115,116] The high value of recovery time of the devices is due to the slow desorption rate of ethanol at room temperature.[117]

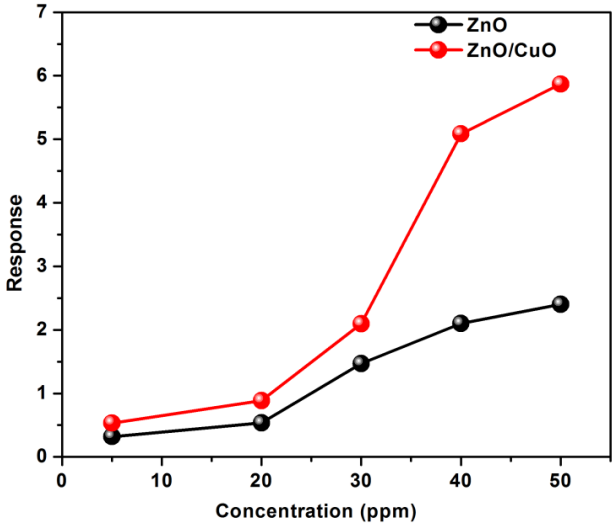

Figure 3.8. Comparison of ethanol response of ZnO and ZnO/CuO structures.

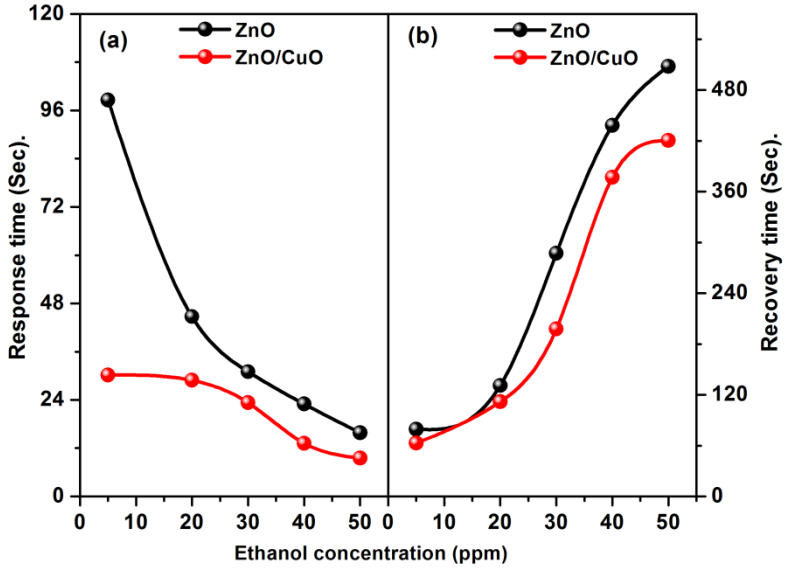

Figure 3.9. (a) Response and (b) recovery time of ZnO and ZnO/CuO structures to ethanol.

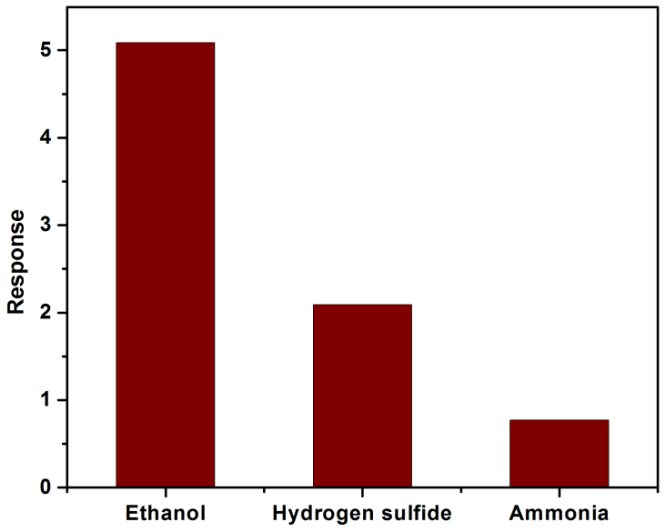

Figure 3.10. The response of ZnO/CuO hierarchical structure to various reducing gases (40 ppm) at room temperature.

In addition to ethanol, the response of ZnO/CuO sensor to other gases was also studied. Figure 3.10 shows the response of ZnO/CuO sensor to 40 ppm concentration of ethanol, hydrogen sulfide, and ammonia. The response value is 5.08 for ethanol whereas it is 2.09 and 0.77 for hydrogen sulfide and ammonia respectively. This is because the electron donating effect of different types of gas molecules is different which depends on the nature of the gas as well as the sensing material.

The basic gas sensing mechanism of metal oxide semiconductors relies on the interaction between adsorbed oxygen molecules on the surface of the sensor material and target gas.[1,29,34,118–120] Generally O_2^- at temperature < 100°C and O^- and O^{2-} at temperature > 100°C are the dominant oxygen species adsorbed on the semiconductor. The adsorption

of oxygen ions on the surface of oxide semiconductor forms an electron depletion region by withdrawing electrons from the conduction band. The interaction between the adsorbed oxygen ions and target gas release electrons back to the semiconductor, consequently the depletion layer width and resistance of the semiconductor decreases.

The reasons for the improved sensing behavior of ZnO/CuO hierarchical structures can be attributed to 1) increased the number of active sites for gas adsorption[121] and 2) the formation of p-n heterojunctions at the interface of p-CuO and n-ZnO.[64,108,122] The high surface to volume ratio of nanorods and the presence of CuO nanoparticles together increased the number of gas adsorption sites. Also, the nanogaps in the nanorod array make more target gas molecules to penetrate into the sensing material. The schematic energy band diagram of p-CuO/n-ZnO heterojunction at thermal equilibrium is shown in figure 3.11 (b). Generally, oxygen deficient ZnO exhibit n-type and oxygen excess CuO exhibit p-type conductivity. When there is a difference in Fermi energy between the materials forming a junction, electrons from the higher energy will flow across the interface to the lower energy until the Fermi energies have equilibrated. This leads to the formation of a depletion region and a potential barrier at the interface. The presence of a number of p-n junctions at the interface result in a remarkable increase in the resistance of the heterostructure compared to pristine ZnO or CuO. The total resistance of the heterostructure will be contributed by the depletion layer on ZnO, accumulation layer on CuO and depletion region at the junction and the increased resistance is clear from the current-voltage (I-V) characteristics in figure 3.12. Because of this increased

resistance of the heterojunction we have chosen a voltage (8 V) higher than the turn-on voltage of the diode for sensing measurements. The response time and recovery time of the sensor depend on the activation energy for gas adsorption and desorption. Both these factors depend on the morphology and composition of the sensing material. In the present work, the one-dimensional morphology of ZnO as well as the attachment of CuO nanoparticles increase the number of adsorption sites for oxygen and may decrease the activation energy for gas adsorption and desorption processes at room temperature resulting in enhanced gas sensing performance.

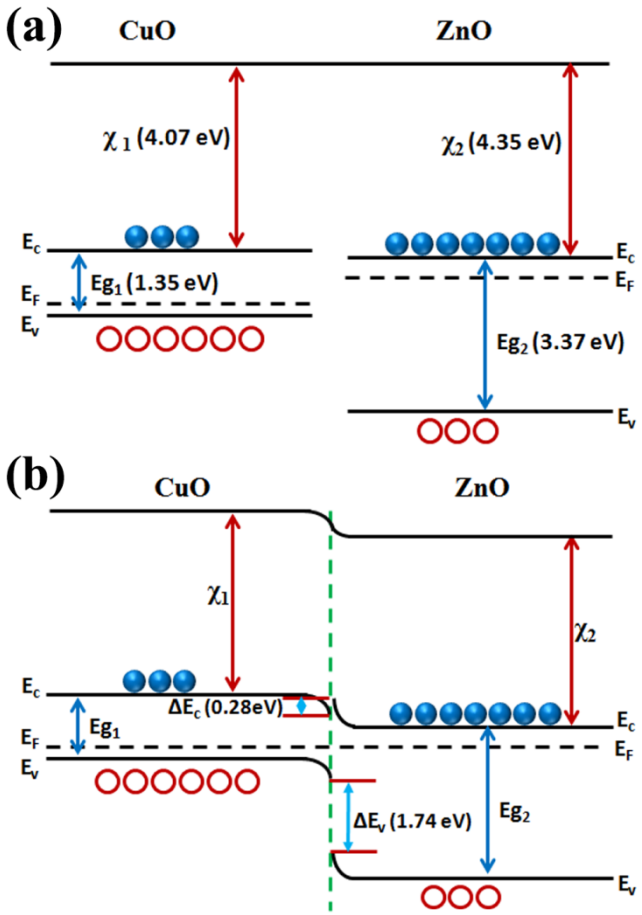

Figure 3.11. Energy-band diagram of (a) CuO and ZnO and (b) ZnO/CuO heterojunction device at thermal equilibrium.

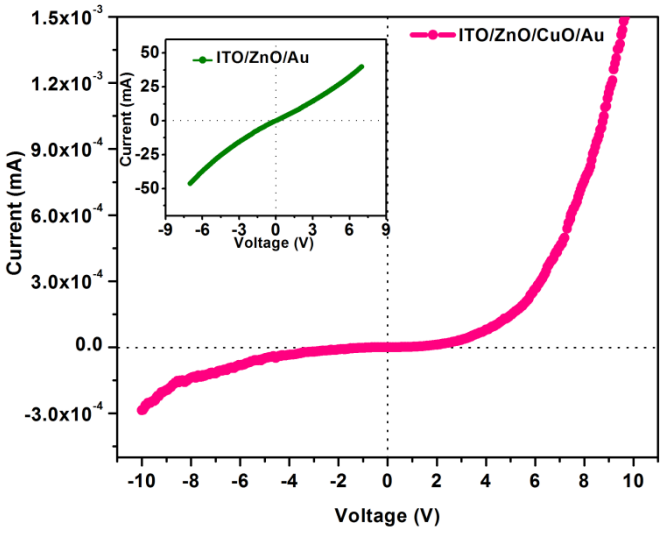

Figure 3.12. Current-voltage characteristics of ZnO/CuO hierarchical structure (Inset shows the I-V characteristics of ZnO alone.

In the energy band diagram shown in figure 3.11, E_{g1}(1.35 eV) , χ_1 (4.07 eV) and E_{g2} (3.37eV) , χ_2 (4.35 eV) represent band gaps and electron affinities[109,123–125] of CuO and ZnO respectively. The barrier height of conduction band ($\Delta E_C = \chi_2 - \chi_1$) and valence band $\left[\Delta E_V = \left(E_{g2} - E_{g1}\right) - \Delta E_C\right]$ at the p-n junction were 0.28 eV and 1.74 eV respectively. The generated free electrons on adsorption of ethanol gas in ZnO can easily transport through the p-n junction due to the low value of ΔE_C and at the same time the holes in CuO will accumulate at the valence band of p-CuO due to the large value of ΔE_V. At low temperatures, the dissociation of ethanol into aldehyde (CH_3CHO) and H_2O are prominent than the formation of CO_2 and H_2O.[116,126,127] At room temperature, the dehydrogenation of ethanol molecules generate OH^- ions (breaking of C-

O bond) and $[CH_3CH_2O]^-$ ions (breaking of O-H bond) due to the lower bond breaking energy of C-O and O-H bonds. Ethanol vapor can be easily attached to metal oxide surfaces in the form of dehydrogenated ionic fragment $[CH_3CH_2O]^-$ through the interaction of adsorbed oxygen on metal oxide surfaces represented by the equation (3.1). Also at the interface of ZnO/CuO junction ethanol molecules react with holes in CuO[39,120,128,129] followed by the equation (3.2).

$$CH_3CH_2OH_{(g)} + O_{2\,(ads)}^- \rightarrow \begin{cases} [CH_3CH_2O]_{(ads)}^- + OH^-{}_{(ads)} \\ CH_3CHO + H_2O + e^- \end{cases} \quad (3.1)$$

$$CH_3CH_2OH_{(g)} + 2h^+ + e^- + O_{2\,(ads)}^- \rightarrow CH_3CHO + H_2O + e^- \quad (3.2)$$

These reactions release free electrons resulting in the enhanced room temperature gas sensing performance of p-CuO/n-ZnO heterojunction device.

3.4 Conclusions

ZnO/CuO heterojunction gas sensor has been successfully fabricated by low-temperature solution processing and its room temperature (29°C) response to various reducing gases has been investigated. Working at room temperature, the response to ethanol gas of the fabricated device is higher than to hydrogen sulfide or ammonia gases. All the gas sensor parameters have been improved by the incorporation of CuO nanoparticles on ZnO nanorods. The easy preparation technique and room temperature gas sensing of the samples will make the practical use of these devices with reduced power consumption a reality.

Chapter 4

Surface modification of TiO_2 nanorod arrays by Ag nanoparticles for improved gas sensing properties

The present chapter details the room temperature gas sensing properties of rutile TiO_2 nanorods functionalized with Ag nanoparticles (Ag-TiO_2). TiO_2 nanorods were grown on FTO substrates through a seed mediated hydrothermal method and Ag nanoparticles were deposited by wet chemical method. The introduction of seed layer markedly improved the porosity of the samples which made them suitable for fabricating efficient gas sensors operating at room temperature. The fabricated device exhibited excellent sensing response to various concentrations of ethanol. The response of TiO_2 sensor to 50 ppm ethanol was 8 with response and

recovery times 6 and 213 seconds respectively. The addition of Ag nanoparticles on the nanorod surface enhanced the response value to 12 and decreased the response and recovery times to 3 and 73 seconds respectively. The improved sensing performance of Ag-TiO_2 structure can be explained on the basis of chemical sensitization via 'spillover' effect and catalytic properties of the noble metal Ag.

Surface modification of TiO_2 nanorod arrays by Ag nanoparticles and its enhanced room temperature ethanol sensing properties, P P Subha, K Hasna, and M K Jayaraj *Material Research Express* 4(10), 105037 (2017).

4.1 Introduction

Titanium dioxide (TiO_2) is a well-established oxide semiconductor widely used for photovoltaic[81] as well as photocatalytic[78] applications and it seems equally good for fabricating gas sensors[130] since changes in the surrounding atmosphere cause appreciable variation in the resistance of TiO_2. TiO_2 exists in three phases; anatase, rutile, and brookite where rutile is the most stable form.[131] One dimensional (1D) nanostructures are ideal candidates for gas sensing applications due to their high surface to volume ratio and efficient electron transfer along their length.[132–135] Since gas sensing is solely a surface phenomenon, the enhanced surface area will, in turn, enhance the performance of the device. Formation of hierarchical structures is an effective and easy way to improve the sensing properties of metal oxide based gas sensors. Hierarchical structures can be formed by coupling secondary nanostructures of either noble metals (Au, Ag, Pd, Pt etc.) or metal oxides (CuO, NiO, SnO_2, TiO_2 etc.) with the

sensing material.[104,136,137] The secondary nanostructures significantly lower the activation energy for gas adsorption reactions and most of them act as catalysts promoting the interaction between surface defects of metal oxide and analyte gases.[138] In addition, noble metal decoration on oxide surface has already been proven to be an efficient way to lower the operating temperature of metal oxide gas sensors.[139]

The present work is on the room temperature gas sensing characteristics of rutile TiO_2 nanorods decorated with Ag nanoparticles. Only a few reports have discussed the ethanol sensing characteristics of Ag-TiO_2 heterostructures.[140–142] The presence of nucleation sites on the substrate has a huge impact on the orientation and morphology of TiO_2 nanorods grown by hydrothermal method. The seed layer significantly increases the density of TiO_2 nanorods leading to high gas adsorption and electron transport, finally resulting in improved sensor performance. A good sensor should be porous enough so that the gas molecules can penetrate into the sample to result in enhanced sensor performance.[143] The increased number of adsorption sites for the target gas molecules will also improve the gas sensing characteristics even at room temperature.[144] Here, we employed seed-mediated hydrothermal method and silver nanoparticle decoration on TiO_2 nanorods to improve the porosity and the number of gas adsorption sites respectively.[47,75] The introduction of a thin layer of TiO_2 on FTO substrate prior to hydrothermal made the nanorods well separated and the reduction in the concentration of the precursor solution remarkably decreased the diameter of the nanorods. The addition of optimized concentration of Ag nanoparticles on the surface of TiO_2 nanorods increased the number of gas adsorption sites. All these factors

together contributed to the enhanced room temperature sensing properties of Ag-TiO_2 heterostructure. The mechanism responsible for the enhanced performance is explained on the basis of chemical sensitization via 'spillover' effect and catalytic properties of noble metal Ag.

4.2 Experimental

4.2.1 Materials

All the chemicals purchased were analytical grade and used without further purification. Titanium tetra-isopropoxide (TTIP) was purchased from Acros Organics. Silver nitrate ($AgNO_3$), hydrochloric acid (HCl), isopropyl alcohol (IPA), ammonia solution, and glucose were purchased from Merck. Deionized water (D.I) was obtained from an ultrafilter system. Fluorine-doped tin oxide (FTO) coated glass substrates (surface resistivity 15-25 Ω/sq) were purchased from Solaronix.

4.2.2 Methods

FTO substrates were ultrasonically cleaned sequentially in acetone, ethanol and D.I water. Prior to the hydrothermal experiment, a thin layer of TiO_2 was deposited on cleaned FTO substrates by immersing them in the optimized concentration of 0.03 M TTIP solution prepared in isopropyl alcohol followed by annealing at 400°C in air for 1 hour. The precursor solution for solvothermal experiment was prepared by adding TTIP (1 ml, 0.8 ml, and 0.6 ml) into a mixture of deionized water and concentrated HCl with a volume ratio of 1:1. Concentrated hydrochloric acid plays an inevitable role in the growth of rutile TiO_2 nanorods.[75,145] H^+ ions from concentrated HCl slow down the hydrolysis rate of TTIP

leading to the formation of crystalline rutile TiO_2. The mixture was stirred well at room temperature and transferred into a Teflon lined autoclave. The solvothermal experiment was carried out at the optimized heating conditions, 180°C for 3 hours. After synthesis, the substrate was taken out, rinsed extensively with deionized water and dried in ambient air. The as-grown nanorods were decorated with Ag nanoparticles by the reduction of $[Ag(NH_3)_2]^+$ with glucose. Solution of $[Ag(NH_3)_2]^+$ was prepared by adding ammonia into $Ag(NO)_3$ solution until it became transparent. The TiO_2 nanorod array was immersed in $[Ag(NH_3)_2]^+$ solution for few minutes. Subsequently, the array was dipped in D.I water and then immersed in glucose solution for few minutes. The sample again dipped in D.I water to remove extra glucose molecules and subsequently dried in ambient air.

4.3 Results and discussion

The structural properties of TiO_2 and Ag nanoparticle decorated TiO_2 nanorods were investigated by glancing angle X-ray diffraction technique. The diffraction patterns of TiO_2 grown on bare and pre-treated FTO substrates are shown in figure 4.1. All the diffraction peaks match well with tetragonal rutile phase of TiO_2 (ICDD No: 00-001-1292). The introduction of seed layer promoted the growth along (101) plane since these planes are the side walls of rod-shaped tetragonal rutile TiO_2 exposed to X-ray whose growth axis is along [001] direction.[146] With the decrease in the volume of TTIP, the intensity of the X-ray diffraction peak corresponding to (101) plane increased and we got maximum intensity for a volume of 0.6 ml TTIP. On further decreasing the volume of TTIP, keeping all other parameters same, no nanorods were formed on

the substrate. Ag nanoparticles were decorated on TiO_2 nanorods synthesized using 0.6 ml TTIP. At low concentration of silver, no impurity peaks were observed whereas on increasing silver concentration diffraction peaks corresponding to Ag_2O also appeared in the spectra shown in figure 4.2. The (111) plane of Ag at 38.09° is observed to be merged with the peak corresponding to FTO (ICDD No: 00-001-1167**)**.

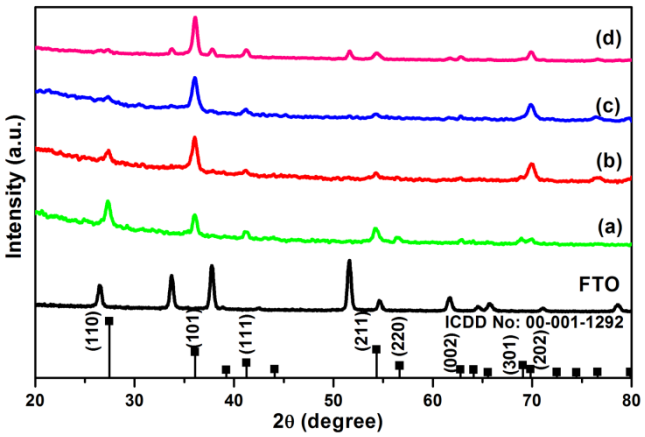

Figure 4.1. Glancing angle X-ray diffraction pattern of TiO_2 nanorods grown on (a) bare FTO substrate using 1ml TTIP for hydrothermal and (b),(c) and (d) seed layer coated FTO substrate using 1,0.8 and 0.6 ml TTIP respectively during hydrothermal.

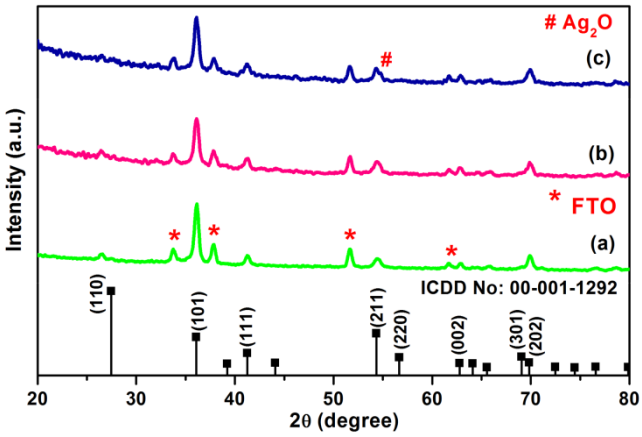

Figure 4.2. Glancing angle X-ray diffraction pattern of (a) TiO_2, and (b) with 0.005 M and (c) 0.01 M $AgNO_3$ solution for preparing Ag decorated TiO_2 nanorods.

Further insight into the structural details of Ag-TiO_2 was obtained by analyzing TEM and HRTEM images. Ag nanoparticles having approximately 10 nm size were found to be uniformly distributed on the surface of TiO_2 nanorods which is clearly seen in figure 4.3(b). The '*d*' spacing values marked in figure 4.3(c) correspond to (101) plane of rutile TiO_2 and (111) plane of Ag. The bright spots in the SAED pattern show the crystallinity of Ag-TiO_2 sample. There exists an optimum concentration of Ag for which we get maximum value of sensor performance. The higher concentration of Ag in the semiconducting material (inset of figure 4.3(b)) reduces the number of active sites for gas adsorption and thereby deteriorates the gas sensing performance. In the present work we have used 0.005 M Ag decorated TiO_2 nanorods for the fabrication of gas sensors.

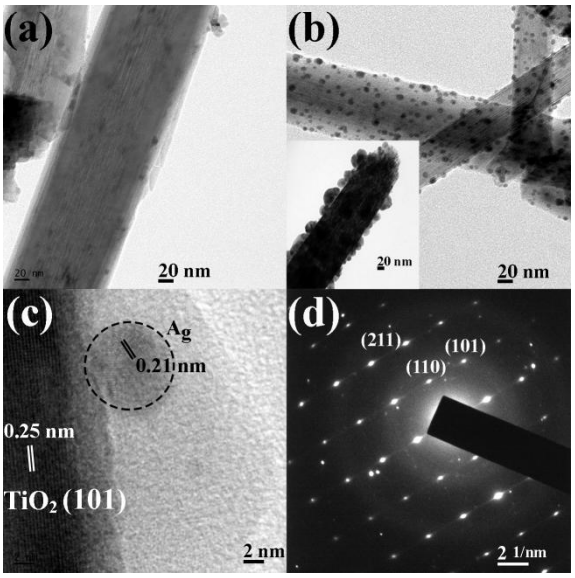

Figure 4.3. TEM images of (a) TiO_2 nanorods (b) 0.005 M Ag decorated TiO_2 (inset shows 0.01 M Ag decorated TiO_2) (c) HRTEM image and (d) SAED pattern of Ag decorated TiO_2 nanorods.

The morphological features of the samples were investigated by analyzing FESEM images. TiO_2 nanorods on bare FTO substrate in figure 4.4 (a) show severe bundling, where each rods are closely packed. The deposition of a thin layer of TiO_2 seed layer on FTO substrate made all the nanorods well separated from each other which is clearly depicted in figure 4.4 (b). The diameter of the nanorods was approximately 100 nm and they are aligned slightly inclined to the substrate surface. This misorientation of the rods will increase the number of Ag nanoparticles adsorbed on the surface of each nanorod. On decreasing the volume of titanium precursor from 1 ml to 0.6 ml, the diameter has reduced noticeably and we got tetragonal nanorods having a diameter approximately 50 nm with square top facets which is used for further

studies. The cross-sectional images reveal the enhanced porosity of the sample with a decrease in volume of the titanium precursor solution. For all samples, the average length of the nanorods was approximately 1.5 μm and no significant variation was observed on changing the experimental conditions used in the present study. For a better gas sensor, the sample should be porous enough to allow penetration of target gas deep into the sample to achieve enhanced sensor parameters. We have observed that the introduction of seed layer, as well as the decreased concentration of the titanium precursor, has effectively improved the porosity and aspect ratio of the nanorods.

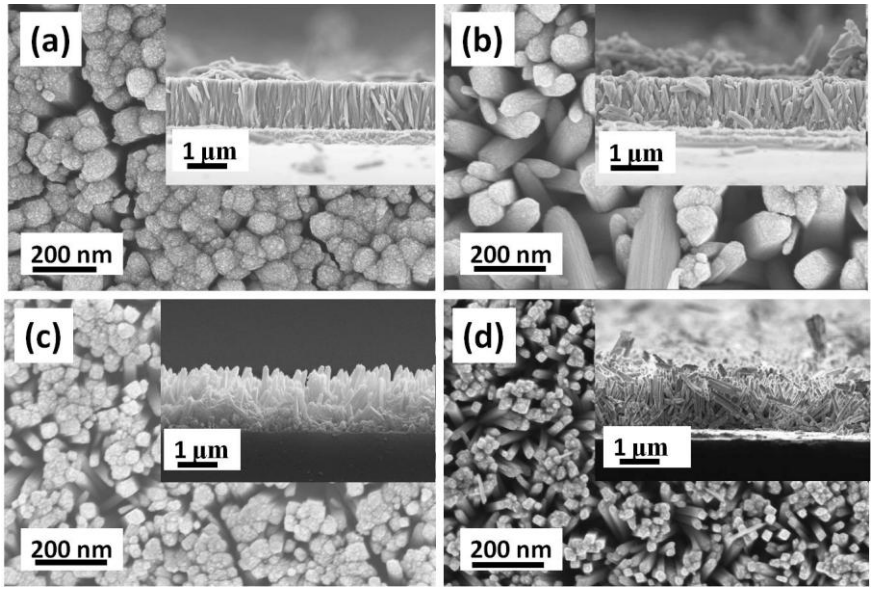

Figure 4.4. FESEM images of TiO_2 nanorods grown on (a) bare FTO substrate using 1ml TTIP for hydrothermal and (b), (c) and (d) seed layer coated FTO substrate using 1, 0.8 and 0.6 ml TTIP respectively. The inset shows the corresponding cross-sectional images.

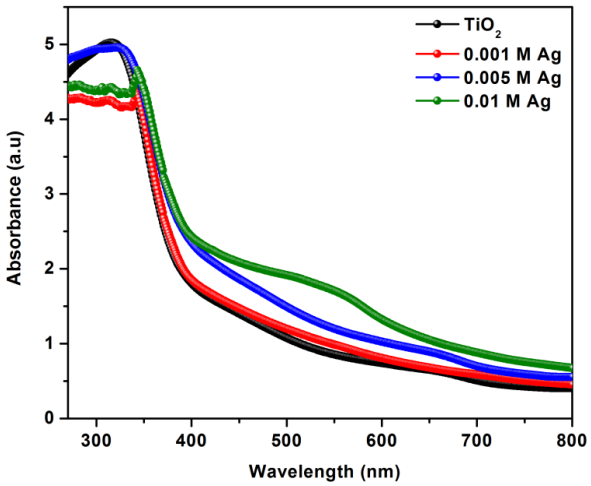

Figure 4.5. Absorption spectra of TiO_2 and Ag nanoparticle decorated TiO_2 nanorods.

The absorption spectra of TiO_2 and Ag decorated TiO_2 nanorod arrays for various concentrations of Ag are shown in figure 4.5. The Ag decorated TiO_2 possess absorbance in the visible region along with the band edge emission of TiO_2. The absorption edge of Ag decorated TiO_2 nanorods shifted to visible region confirming the presence of Ag on the surface of TiO_2 nanorods. With the increase in Ag concentration, the absorption becomes stronger and more red shifted due to the increased quantity and larger size of Ag nanoparticles.

Gas sensors were fabricated by depositing circular gold electrodes on the top of nanorod array. The schematic of the device structure is shown in figure 4.6 (i). The sensing measurements were carried out by applying a constant voltage of 1 V to TiO_2 and 0.5 V to Ag-TiO_2

respectively. The room temperature ethanol sensing characteristics of TiO_2 nanorods grown on bare and seed layer coated FTO substrates are shown in figure 4.6 (ii) where the improved response is obviously seen for nanorods grown on a substrate with the seed layer. The response value for nanorods grown on seed layer coated substrate is almost 4 times greater than that grown on the bare substrate because the former sample is porous enough facilitating more gas molecules to penetrate into the film resulting in enhanced sensing performance.[43]

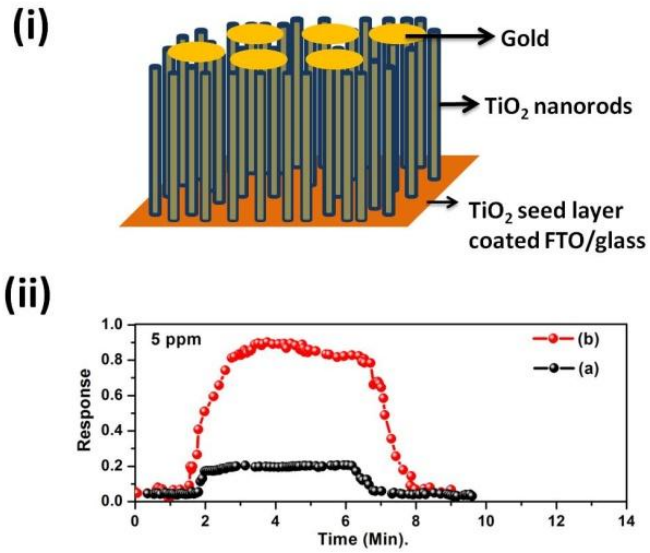

Figure 4.6. (i) Schematic of the device structure and (ii) room temperature ethanol response characteristics of TiO_2 nanorods grown on (a) bare FTO substrate and (b) seed layer coated FTO substrate.

Figure 4.7 displays the room temperature ethanol response curves of TiO_2 and Ag decorated TiO_2. The response curve clearly shows

significant enhancement in Ag decorated TiO_2 nanorods for all the target gas concentrations used in the present study. The better sensing characteristics in Ag-TiO_2 samples can be attributed to the enhanced surface area as well as the catalytic properties of Ag nanoparticles. The attachment of Ag nanoparticles increases the specific surface area of the sample which in turn increases the number of active sites for gas adsorption.[147]

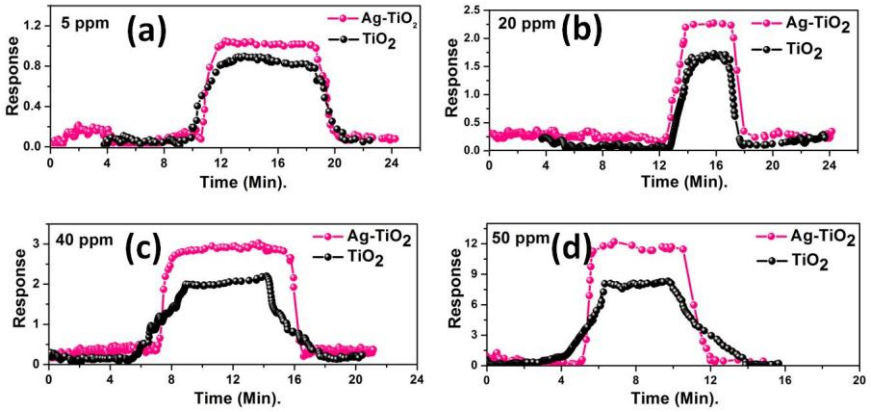

Figure 4.7. Room temperature response characteristics of TiO_2 and Ag decorated TiO_2 nanorods for various concentrations of ethanol.

Figure 4.8 compares the response of TiO_2 and Ag-TiO_2 sensors to various concentrations of ethanol. Increase in concentration of the target gas has resulted in improvement of the response of both the sensors; with Ag-TiO_2 heterostructure response being much more enhanced compared to that of pristine TiO_2. The response values calculated for TiO_2 and Ag-TiO_2 are 0.8 and 1.1 for 5 ppm and 8.15 and 11. 98 for 50 ppm ethanol gas, respectively.

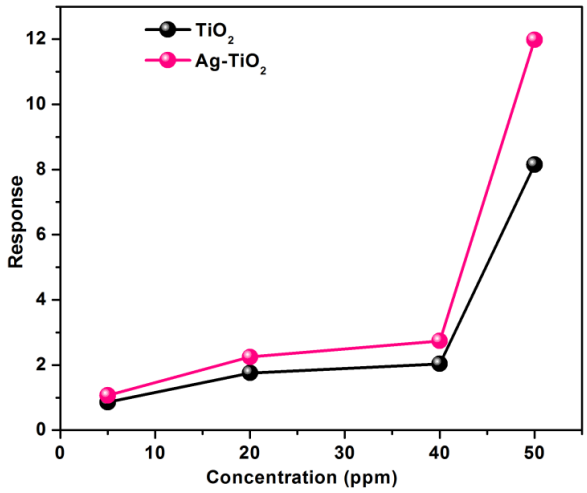

Figure 4.8. Comparison of ethanol response of TiO_2 and Ag-TiO_2 sensors.

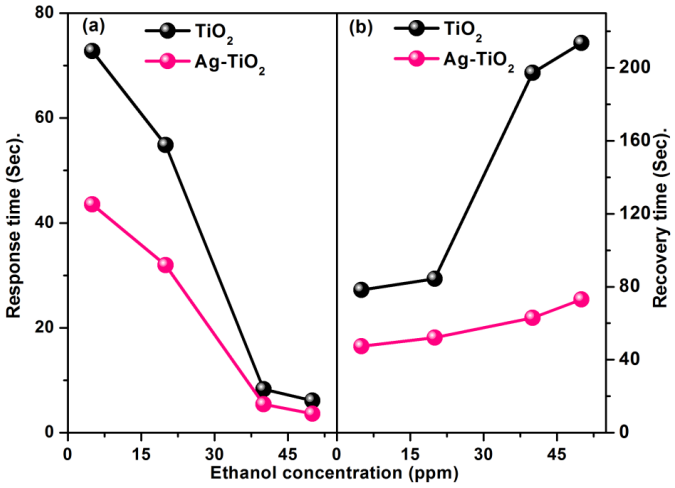

Figure 4.9. (a) Response and (b) recovery time of TiO_2 and Ag-TiO_2 sensors.

The variation in response and recovery time of the sensors with ethanol concentration is shown in figure 4.9. The response time decreases

with increase in concentration whereas the recovery time increases with increase in concentration. The response time of TiO_2 and Ag-TiO_2 sensors to 5 ppm ethanol are 73 and 43 seconds and those to 50 ppm are 6 and 3 seconds, respectively.

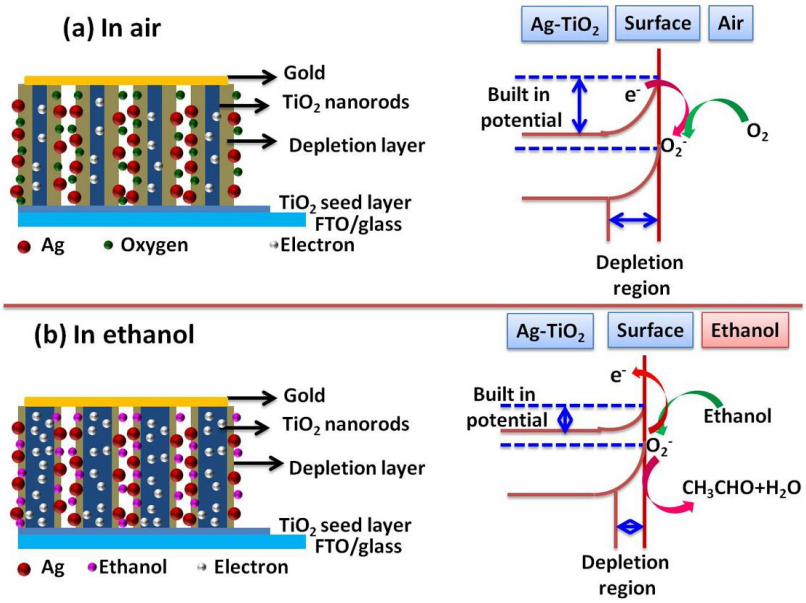

Figure 4.10. Schematic representation of charge carrier density and depletion layer in Ag-TiO_2 in (a) ambient air and (b) ethanol gas. (Respective band diagrams are shown).

The dramatic improvement in the response time of Ag-TiO_2 for detecting even low concentration of ethanol can be attributed to the enhanced specific surface area contributed by the hierarchical structure and the presence of catalytically active Ag nanoparticles. Similarly, an obvious improvement in the recovery time is also observed for the hierarchical sensor where the recovery time reduced to 73 seconds from

213 seconds for 50 ppm ethanol. Thus, it can be concluded that Ag decorated TiO_2 nanorod arrays exhibit excellent sensing characteristics at room temperature and hence they can be used for potential gas sensor applications.

The sensing properties are largely dependent on the charge transport dynamics between target gas molecules and adsorbed oxygen ions. The gas sensing mechanism of metal oxide nanostructures relies on the redox reactions taking place between target gas molecules and adsorbed oxygen on the semiconductor surface.[32,44] Depending on the sensor operating temperature T, oxygen molecules can be adsorbed either as O_2^- at $T < 100°C$ or O^-or O^{2-} at $T > 100°C$[28]. When the metal oxide sensor is exposed to air the oxygen molecules trap electrons from the conduction band of the sensing material due to its strong electronegativity and form oxygen ions. In the present case, oxygen molecules from air combines with surface electrons of TiO_2 and form "molecular ion" O_2^-. The oxygen adsorption reaction at room temperature can be represented by the equation (4.1)

$$O_2(ads) + e^- \rightarrow O_2^-(ads) \qquad (4.1)$$

As a result, the free carrier concentration in the sensing material decreases and a depletion region will be formed which in turn increases the resistance of the sensing material. When the reductive ethanol is introduced into the chamber chemical reactions take place between ethanol molecules and adsorbed oxygen ions releasing electrons back to the material decreasing the width of the depletion region and hence the resistance of the sensing material.[148] All these processes are schematically

illustrated in figure 4.10 and corresponding chemical reactions can be written as

$$CH_3CH_2OH_{(g)} + O_{2\,(ads)}^{-} \rightarrow \begin{cases} [CH_3CH_2O]_{(ads)}^{-} + OH_{(ads)}^{-} \\ CH_3CHO + H_2O + e^{-} \end{cases} \quad (4.2)$$

Even without silver nanoparticles decoration, TiO_2 exhibited good ethanol response characteristics at room temperature. This can be due to the direct adsorption of a target gas by the semiconductor in addition to the interaction with adsorbed oxygen ions.[149,150] The addition of Ag nanoparticles on the surface of TiO_2 nanorods markedly lowered the response and response and recovery time of the sensor at room temperature. The predominant mechanism responsible for the significant improvement in the sensing performance of Ag decorated TiO_2 nanorods at room temperature can be attributed to chemical sensitization via "spillover effect" and exceptional catalytic properties of Ag nanoparticles towards oxidation and reduction of gases.[27,140,144,151–154] In chemical sensitization, catalyst metal nanoparticles do not change the resistance of the metal oxide leaving the sensing mechanism same as that without the presence of metal nanoparticles. In spillover effect, metal nanoparticles act as gas adsorption centers facilitating catalytic oxidation and reduction processes leading to faster reactions between target gas molecules and adsorbed oxygen ions. Rather than forming a continuous film, additive nanoparticles must be dispersed on the surface of the metal oxide sensing material so that both oxide material and additive will be exposed to the surrounding ambient. Uniformly distributed Ag nanoparticles can act as an efficient catalyst for adsorption-desorption reactions of both oxygen and ethanol. Silver nanoparticles can effectively reduce the activation

energy for gas adsorption, accelerating the electron exchange between target gas and sensing material.[142] The spillover effect promotes catalytic oxidation and makes the reactions between target gas molecules and adsorbed oxygen ions faster. An excessive amount of silver nanoparticles effectively reduces the active surface area of the whole device thereby decreasing the gas sensing performance. Also, the higher Ag concentration forms a network of silver nanoparticles on the surface of metal oxide nanorods and the material exhibit almost a metallic behavior. At this condition, the oxygen molecules and target gas molecules are not capable of appreciably altering the conductivity of the sensing material with a consequent loss of sensor response.[144] The results in the present work can be further explored for various potential applications.

4.4 Conclusions

Room temperature ethanol sensors were developed using TiO_2 and Ag-TiO_2 nanostructures synthesized by simple solution methods. The seed layer has a significant effect on the density, orientation, and gas sensing properties of rutile TiO_2 nanorods. The remarkable increase in the ethanol response characteristics was observed on modifying the surface of the nanorods with Ag nanoparticles. The simple cost-effective processing techniques and room temperature operation of the Ag-TiO_2 sensor make it a potential candidate for future environment applications.

Chapter 5

Fabrication of solution processed TiO_2/CuO heterojunction and its room temperature gas sensing properties

In the previous chapter, we have seen the effects of Ag nanoparticles on the room temperature ethanol sensing properties of TiO_2 nanorods and have obtained excellent improvement in the response and recovery time of the sensor. Still, there was not much enhancement in the response value. The present chapter details the influence of CuO nanoparticles on the ethanol sensing characteristics of TiO_2 nanorods. With the incorporation of CuO nanoparticles, the response of TiO_2 has been increased to 34 and response time has been reduced to 2 seconds for

50 ppm concentration of ethanol. The corresponding response and response time values for TiO_2 were 8 and 6 seconds respectively. Here the recovery time was almost constant for both TiO_2 and TiO_2/CuO. The reasons for improved response characteristics can be attributed to the higher surface area contributed by the hierarchical structure and the formation of multiple p-n junctions at the interface of TiO_2 and CuO.

Solution-processed TiO_2/CuO heterojunction for enhanced room temperature ethanol sensing applications, P P Subha, L S Vikas, and M K Jayaraj, *Physica Scripta* (under review).

5.1 Introduction

Metal oxide nanostructures are widely accepted for gas sensor fabrication especially because of their inherent resistance change in accordance with the changes in the surrounding atmosphere. Among the inorganic metal oxides, TiO_2 has significant importance because of its unique catalytic and electrical properties. TiO_2 in its rutile phase is the most stable form which is extensively used in photovoltaics[75,76], gas sensors[144,155], catalysis[156,157], batteries[158,159] etc. Nanomaterials can be used for improving the gas sensing properties especially because of their high surface to volume ratio and other interesting properties.[11,160] Among them, the directional mobility of charge carriers and high surface to volume ratio of one-dimensional (1D) nanostructures such as nanorods, nanowires, nanobelts, and nanotubes attract the intense attention of researchers to use them in a wide variety of applications.[130,132]

Metal oxides such as SnO_2, ZnO, TiO_2, WO_3 etc. are widely used for fabricating gas sensor devices. Most of the metal oxide based gas

sensors operate at an elevated temperature generally above 150°C. Reducing the operating temperature eventually reduces the power consumption of the device making it useful for explosive environments where high temperature is undesirable. In addition, the low values of sensor parameters such as response, response and recovery time, selectivity etc. inhibit the practical implementation of these devices. Several techniques such as metal loading[47], forming hierarchical structures[161], light activation[162] etc. can be employed to overcome these disadvantages. The use of hierarchical nanostructures constituting two or more compounds always give excellent properties compared to their individual counterpart and hence improve the properties of metal oxide based devices.[104,108] One-dimensional TiO_2 can form hierarchical structures either with noble metals[163,164] (Ag, Au, Pt, Pd etc.) or metal oxides[165–167] (CuO, ZnO, Co_3O_4 etc.). In the present work, we have successfully synthesized rutile TiO_2 nanorods decorated with CuO nanoparticles by simple solution techniques. In addition to the unique one-dimensional morphology of TiO_2 nanorods, the hierarchical structure formed by the attachment of CuO nanoparticles provide plenty of active sites for gas adsorption reactions. Generally, most of the p-type oxide semiconductors have been widely used as catalysts to promote oxygen dissociation.[168–170] CuO nanoparticles accelerate the diffusion of oxygen molecules into surface vacancies and capture electrons from the conduction band of TiO_2 to become oxygen ions. Also the successful integration of p-type CuO and n-type TiO_2 form p-n heterojunctions resulting in better room temperature sensing characteristics. TiO_2 nanorods were synthesized by seed-mediated hydrothermal method and CuO nanoparticles were deposited by wet chemical method followed by

annealing. Both hydrothermal, as well as wet chemical methods, are already proven to be versatile, low-cost and environment-friendly.

5.2 Experimental

5.2.1 Materials

All the chemicals purchased were analytical grade and used without further purification. Titanium tetra isopropoxide; TTIP (Acros Organics), hydrochloric acid; HCl (Merck), and isopropyl alcohol; IPA (Merck), and copper acetate hydrate; (Fisher Scientific) were used as the precursors for the hydrothermal growth of TiO_2/CuO samples nanorods. Deionized water was obtained from an ultrafilter system. Fluorine-doped tin oxide (FTO) coated glass substrate having surface resistivity 15-25 Ω/sq (Solaronix) was used as the substrate and bottom electrode.

5.2.2 Growth of TiO_2 nanorods on FTO substrate

FTO substrates were ultrasonically cleaned sequentially in ethanol and deionized water. Prior to hydrothermal growth, a thin layer of TiO_2 was deposited on cleaned FTO substrates by immersing them in 0.03 M TTIP solution prepared in isopropyl alcohol followed by annealing at 400°C in air for 1 hour. The precursor solution for hydrothermal growth was prepared by adding 0.6 ml TTIP into a mixture of deionized water and concentrated HCl took in a volume ratio of 1:1. The mixture was stirred well at room temperature and transferred into a Teflon lined autoclave. The solvothermal experiment was carried out at the optimized conditions 180°C for 3 hours. After synthesis, the substrate was taken out, rinsed with deionized water and dried in ambient air.

5.2.3 Deposition of CuO nanoparticles on the surface of TiO_2 nanorods

For depositing CuO nanoparticles on TiO_2 nanorods, as grown TiO_2 samples were immersed in copper acetate solution (0.05 M and 0.1 M) for 1 hour and annealed at the optimized temperature 250°C for 2 hours in air.

5.3 Results and discussion

The phase composition and crystal structure of the samples were investigated by glancing angle X-ray diffraction technique. The X-ray diffraction pattern of pristine TiO_2 exhibits peaks corresponding to tetragonal rutile structure with prominent orientation along (101) plane (ICDD No: 00-001-1292). In addition to TiO_2, monoclinic CuO diffraction peaks (ICDD No: 00-005-0661) were observed in the spectra of 0.1 M CuO decorated TiO_2 nanorod array which can be clearly seen in the inset magnified image of figure 5.1. No significant diffraction peaks were obtained for CuO at lower copper acetate concentrations and above 0.1 M impurity peaks other than CuO were observed in the X-ray diffraction pattern.

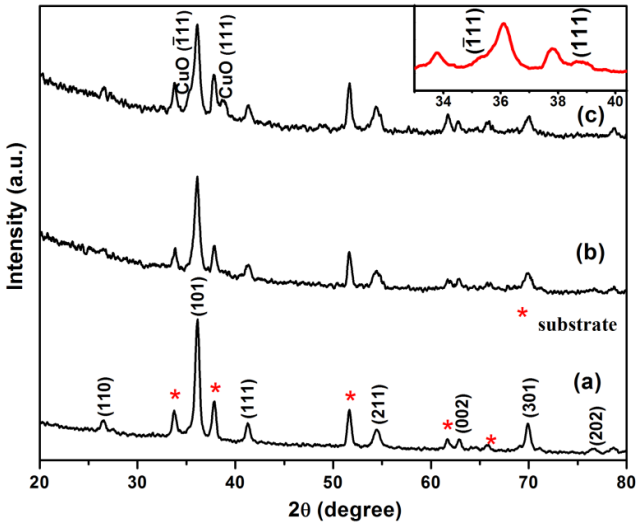

Figure 5.1. Glancing angle X-ray diffraction pattern of (a) TiO_2, and CuO decorated TiO_2 nanorods by immersing in (b) 0.05 M and (c) 0.1 M copper acetate solution. (Inset shows the magnified view of the peaks corresponding to monoclinic CuO).

The detailed structural analyses of TiO_2 and TiO_2/CuO (0.1 M Copper acetate) were done with transmission electron microscopy. Figure 5.2(a) shows pristine TiO_2 nanorod and in figure 5.2(b) uniform distribution of CuO nanoparticles having approximately 10 nm size on the surface of TiO_2 nanorods can be clearly seen, further confirming the formation of CuO decorated TiO_2 nanorods. The HRTEM image and SAED pattern of the heterostructure are shown in figure 5.2(c) and 5.2(d) respectively. The marked $'d'$ spacing values correspond to (101) plane of rutile TiO_2 and $(\bar{1}11)$ plane of monoclinic CuO respectively. The bright spots in the SAED pattern confirm the polycrystalline nature of TiO_2/CuO heterostructure.

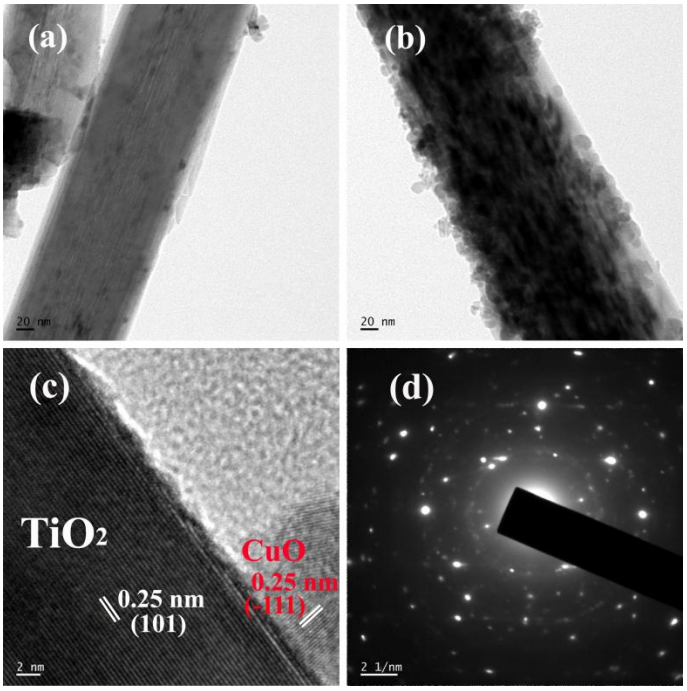

Figure 5.2. TEM images of (a) TiO_2 and (b) TiO_2/CuO (c) HRTEM image of TiO_2/CuO and (d) SAED pattern of TiO_2/CuO.

Micro Raman spectroscopy is a widely accepted technique used to analyze the vibrational properties of nanostructures. Raman spectra of the samples recorded at an excitation of 514 nm are displayed in figure 5.3. The first order Raman spectrum of rutile TiO_2 shows four Raman active fundamental modes such as B_{1g} (144 cm^{-1}), E_g (446 cm^{-1}), A_{1g} (610 cm^{-1}) and B_{2g} (826 cm^{-1}) along with secondary scattering features, the one at 238 cm^{-1} being the most prominent.[171,172] All the observed modes in the spectra correspond to tetragonal rutile structure of TiO_2 nanorods. The three Raman active modes exhibited by monoclinic CuO can be assigned

at 278 cm^{-1}(A_g), 333 cm^{-1} (B_{1g}) and 620 cm^{-1} (B_{2g}).[112,113] The A_g and B_{1g} vibrational modes are visible in figure 5.3 and the inset multi-peak fitting curve shows the B_{2g} mode of CuO. Thus X-ray diffraction pattern, TEM analysis, and Raman analysis confirmed the incorporation of CuO nanoparticles on TiO_2 nanorods.

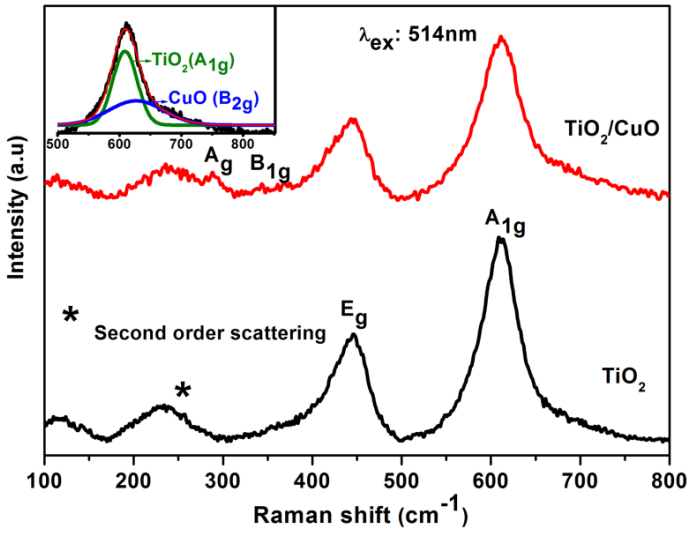

Figure 5.3. Micro Raman spectra of TiO_2 and TiO_2 /CuO (Inset shows the multi-peak fitting curve of TiO_2/CuO heterojunction).

The FESEM images of pristine TiO_2 and TiO_2/CuO samples are shown in figure 5.4. TiO_2 nanorods having square top facets inclined at an angle with the substrate surface were grown on seed layer coated FTO substrate. The average length and diameter of the rods are approximately 1.5 μm and 50 nm respectively. No noticeable variation in morphology was observed for TiO_2/CuO in figure 5.4(d) which may be due to the very small size of CuO nanoparticles.

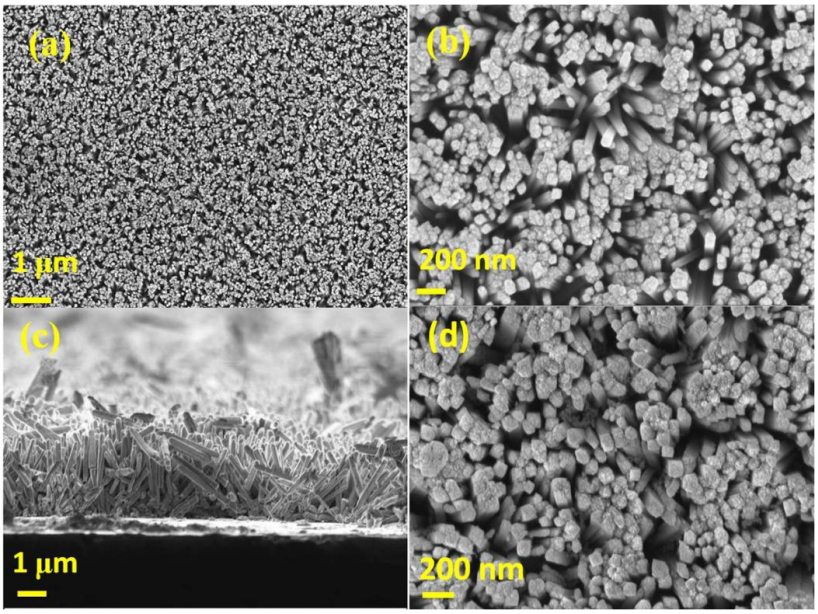

Figure 5.4. FESEM images of TiO_2 nanorods (a) large area view (b) magnified view (c) cross-sectional view and (d) TiO_2/CuO heterojunction.

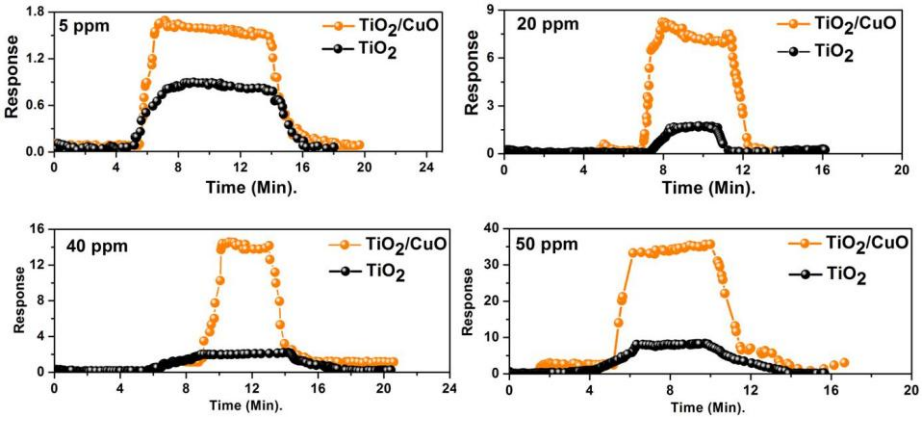

Figure 5.5. Room temperature response characteristics of TiO_2 and TiO_2/CuO heterojunction to various concentrations of ethanol.

The room temperature (29°C) ethanol response characteristics of TiO_2 and TiO_2/CuO heterojunction device are shown in figure 5.5. The applied voltages to TiO_2 and TiO_2/CuO were 1 and 5 V respectively. Both pristine TiO_2 nanorod array and TiO_2/CuO hetero-junction sensors exhibit an appreciable response to various concentrations of ethanol at room temperature. The measured current increased in the presence of ethanol and it retains the initial resistance in ambient air. TiO_2/CuO sensor shows significant enhancement in the sensing characteristics compared to the pristine sample. It can be seen that the response value gradually increases with increase in the concentration of the target gas. Even for 5 ppm concentration of ethanol both the sensors exhibit an obvious response at room temperature.

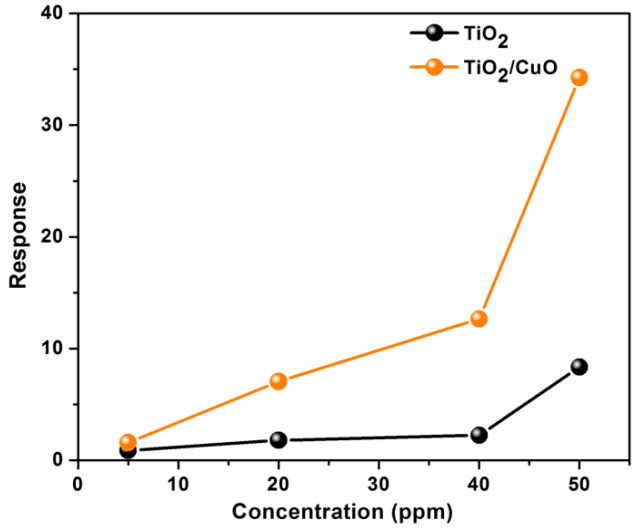

Figure 5.6. Comparison of ethanol response of TiO_2 and TiO_2/CuO heterojunction.

Figure 5.6 compares the room temperature ethanol response characteristics of TiO_2 and TiO_2/CuO sensors which clearly show the excellent improvement in sensor response for heterojunction sensor. In addition to the response, the response speed of the CuO decorated TiO_2 nanorods also increased compared to the pristine sensor which can be clearly seen in figure 5.7. The response time calculated for TiO_2/CuO sensor to 5 and 50 ppm ethanol is 12 and 2 seconds and for TiO_2 alone these values are 73 and 6 seconds respectively. The dramatic improvement in the response speed can be attributed to the formation of multiple p- n junctions at the interface of CuO nanoparticles and TiO_2 nanorods. Even though the response and response time of the heterojunction sensor has been improved, the recovery time remained almost same for both the sensors. This may be due to the low desorption rate of ethanol at room temperature.[117]

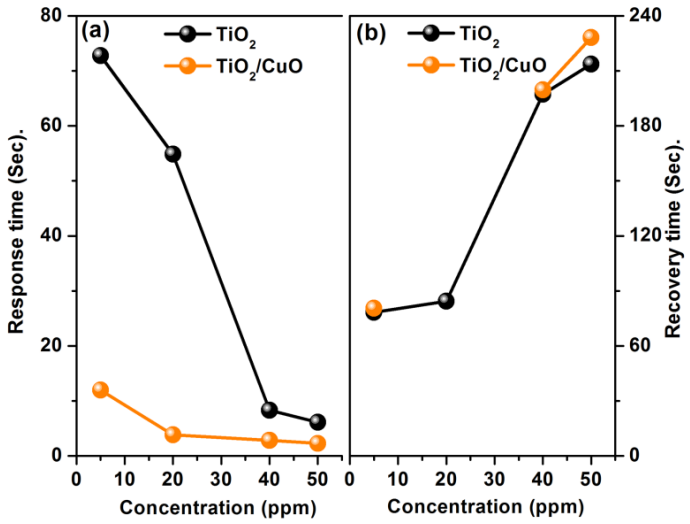

Figure 5.7. (a) Response and (b) recovery time of TiO_2 and TiO_2/CuO structures.

The sensing mechanism of metal oxide based gas sensors is based on the change in resistance caused by the interaction between adsorbed oxygen ions and target gas molecules.[1,32,132,173] The oxygen molecules trap electrons from the conduction band of the metal oxide semiconductor and form oxygen ions. This process leads to the formation of a depletion region in the semiconductor with a consequent increase in the resistance of the sensing material. Any reducing gas, like ethanol, on reacting with these adsorbed oxygen ions release electrons back to the semiconductor thereby reducing the width of the depletion layer as well as the resistance of the sensing material. Depending on the operating temperature of the sensor, oxygen molecules can form O_2^- (below 100°C), O^-(100°C-400°C) and O^{2-}(above 400°C) by withdrawing electrons from the conduction band.[132,174] The oxygen adsorption reactions at room temperature can be represented by the following equations.

$$O_2(g) \rightarrow O_2(ads) \quad (5.1)$$

$$O_2(ads) + e^- \rightarrow O_2^-(ads) \quad (5.2)$$

The enhanced sensing performance of TiO_2/CuO heterojunction at room temperature is due to the following reasons. Firstly, the unique structure consisting of one-dimensional TiO_2 nanorods modified with CuO nanoparticles offer plenty of active sites for gas adsorption.[175,176] Most of the p-type oxide semiconductors like CuO, NiO, Co_3O_4 etc. are good candidates for promoting oxygen dissociation. In the present case, the catalytic properties of CuO make oxygen to diffuse faster into the surface vacancies of TiO_2 nanorods capturing electrons from the conduction band and form oxygen ions.[125] The above-mentioned

properties of CuO nanoparticles result in the adsorption of large quantities of oxygen on the oxide surface within a short time leading to an increase in resistance of the material. Since there are more adsorbed oxygen molecules, more ethanol molecules can react with oxygen molecules and reduce the resistance of the sensing material contributing to the enhanced sensing performance. Secondly, the formation of p-n junctions at the interface of n-TiO_2 and p-CuO has a remarkable effect on the gas sensing properties of the heterojunction sensor. Generally, oxygen deficient TiO_2 exhibits n-type conductivity and oxygen excess CuO displays p-type conductivity. The formation of p-n heterojunction at the interface of TiO_2 and CuO results in band bending in the depletion layers and correspondingly a built-in electric field is developed by the transfer of electrons to p-type CuO and holes to n-type TiO_2 until the system obtains an equalization of Fermi levels. The built-in field enhances the transfer efficiency of interfacial charge to the oxygen molecules adsorbed on the surface of the oxide semiconductor.[177] The resistance of the heterojunction can be expressed by the equation

$$R \propto B \exp(q\emptyset/kT) \tag{5.3}$$

where B is a constant, k is the Boltzmann constant, T is the absolute temperature and $q\emptyset$ is the effective potential energy barrier at the heterojunction. Under exposure to air the, energy barrier $q\emptyset$ will be high because of oxygen adsorption. Ethanol gas molecules react with these adsorbed oxygen ions and the trapped electrons are released back to the semiconductor leading to the decrease in energy barrier $q\emptyset$ formed at the interface. From equations (1.1) and (5.3) it is obvious that the response

magnitude of the heterojunction sensor is in direct proportion to the value of exp ($\Delta q\emptyset$) and hence the marked changes in the energy barrier can induce significant changes in the resistance and correspondingly in the response magnitude of the heterojunction sensors, called as the synergistic effect.[108,177,178] The increase in the resistance of TiO_2/CuO heterojunction is clear from the current-voltage (I-V) characteristics in figure 5.8. In addition, the excellent catalytic properties of TiO_2 and CuO heterojunction promote the interaction between ethanol molecules and adsorbed oxygen ions contributing to enhanced room temperature response characteristics.[156,179,180]

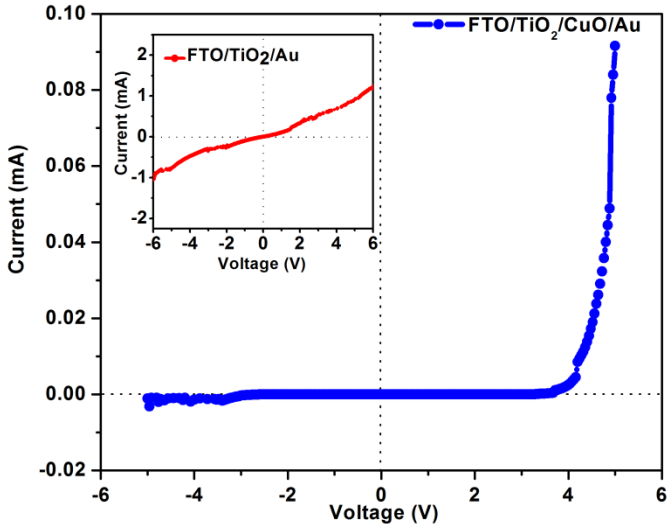

Figure 5.8. I-V characteristics of TiO_2/CuO hetero-junction (Inset shows the I-V curve of pristine TiO_2).

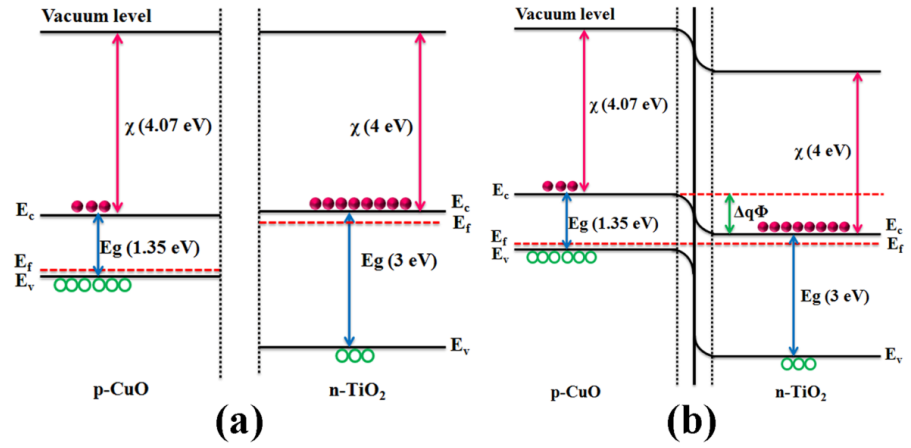

Figure 5.9. Energy band diagram for TiO_2/CuO heterojunction (a) before equilibrium and (b) after equilibrium.

Usually, alcohol molecules react with adsorbed oxygen ions undergoing dehydrogenation and dehydration reactions to form CO_2 and H_2O respectively. Since the sensors in the present work operate at room temperature, ethanol molecules undergo dehydrogenation reactions by breaking $C-O$ and $O-H$ bonds due to their lower bond breaking energies and form aldehyde and water represented by the equation (5.4).[120,129]

$$CH_3CH_2OH_{(g)} + O_{2\,(ads)}^{-} \rightarrow \begin{cases} [CH_3CH_2O]_{(ads)}^{-} + OH^{-}{}_{(ads)} \\ CH_3CHO + H_2O + e^{-} \end{cases} \qquad (5.4)$$

The result demonstrated in the present work concludes that the fabrication of heterojunctions is an effective way to improve the gas sensing properties of metal oxide based gas sensors.

5.4 Conclusion

Low-temperature solution processed gas sensors were fabricated and its room temperature ethanol sensing characteristics were investigated. We have demonstrated a simple, low-cost two-step process for developing gas sensors based on metal oxide heterostructures. Both TiO_2 and TiO_2/CuO exhibit appreciable response to ethanol at room temperature and the heterojunction sensor show remarkable improvement in the response characteristics. The room temperature gas sensing properties make the device suitable for several applications including that in explosive environments.

Chapter 6

Synthesis and room temperature gas sensing characteristics of TiO_2/ZnO hierarchical structure

In the previous chapters, room temperature ethanol response characteristics of ZnO/CuO, Ag-TiO_2, and TiO_2/CuO were discussed. Excellent improvements in the response and recovery time have been observed for Ag-TiO_2 and high value of response has been obtained for TiO_2/CuO hierarchical structures. With the use of TiO_2/ZnO hierarchical structures, the response value has been increased to 40 and response and recovery times were decreased to 6 and 90 seconds respectively for 50 ppm ethanol, which is better than the performance of the devices discussed in the previous chapters. Thus, all the sensor parameters could be improved in a single device.

6.1 Introduction

Greater surface area of hierarchical nanostructures is attracting people in the field to fabricate high-performance gas sensors. Among the various semiconducting oxide materials, TiO_2 and ZnO are two technologically important materials due to their electrical and optical properties. Compared to their individual counterpart, the combination of TiO_2 and ZnO can further enhance the gas sensing properties making them suitable for fabricating efficient devices. Titanium dioxide (TiO_2) is one of the most promising semiconducting materials for gas detection due to its excellent physical and chemical properties, high environmental stability, and catalytic properties.[77,181] TiO_2 based hierarchical structures like TiO_2/ZnO[59,70], TiO_2/SnO_2[58,182], TiO_2/Co_3O_4[168,183] etc. with improved gas sensing properties were already reported. The improved sensing properties of hierarchical structures are due to its high surface to volume ratio, the formation of heterojunctions at the interface and their catalytic properties. The materials constituting the hierarchical structure should have appropriate energy levels to form a potential barrier at the heterojunction interface. The band gap, electron affinity and work function of TiO_2 and ZnO are 3 eV, 4 eV, 4.9 eV and 3.37 eV, 4.35 eV, 5.3 eV respectively.[184,185] The difference in work function between TiO_2 and ZnO facilitate migration of electrons across the junction forming an accumulation layer in ZnO rather than a depletion region. This charge transfer develops a potential barrier at the interface contributing to the enhanced gas sensing performances.[64,108] In the present work, we have successfully developed TiO_2/ZnO hierarchical structures and its ethanol response characteristics were investigated at room temperature.

6.2 Experimental

6.2.1 Materials

All the reagents were of analytical grade and used without further purification. Titanium tetra isopropoxide; TTIP (Acros Organics), hydrochloric acid; HCl (Merck), and Isopropyl alcohol; IPA (Merck) were used as the precursors for the hydrothermal growth of TiO_2 nanorods. zinc nitrate (Merck) and hexamethylenetetramine; HMTA (Alfa Aesar) were used for the synthesis of ZnO nanorods. Deionized water was obtained from an ultrafilter system. Fluorine-doped tin oxide (FTO) coated glass substrate having surface resistivity 15-25 Ω/sq (Solaronix) was used as the substrate and bottom electrode.

6.2.2 Synthesis of rutile TiO_2 nanorods on FTO/glass substrate

Rutile titanium dioxide nanorods were synthesized by a seed-mediated low-temperature hydrothermal method. Prior to hydrothermal, a thin layer of TiO_2 was deposited on cleaned FTO/glass substrate by immersing FTO in 0.03 M TTIP solution prepared in isopropyl alcohol followed by annealing at 400°C in air for 1 hour. The precursor solution for solvothermal experiment was prepared by adding 0.6 ml TTIP into a mixture of deionized water and concentrated HCl taken in a volume ratio of 1:1. Hydrothermal experiment was carried out at 180°C for 3 hours to form well aligned rutile TiO_2 nanorods.

6.2.3 Growth of ZnO nanorods over TiO_2 nanorods

ZnO nanorods were grown over TiO_2 nanorods by a second hydrothermal process in which TiO_2 nanorods were used as the substrate and the precursor solution contains 0.1 M zinc nitrate and 0.1 M hexamethylenetetramine. Hydrothermal experiments were carried out at 100°C for 2 hours. After hydrothermal, the samples were taken out and dried in ambient air.

6.3 Results and discussion

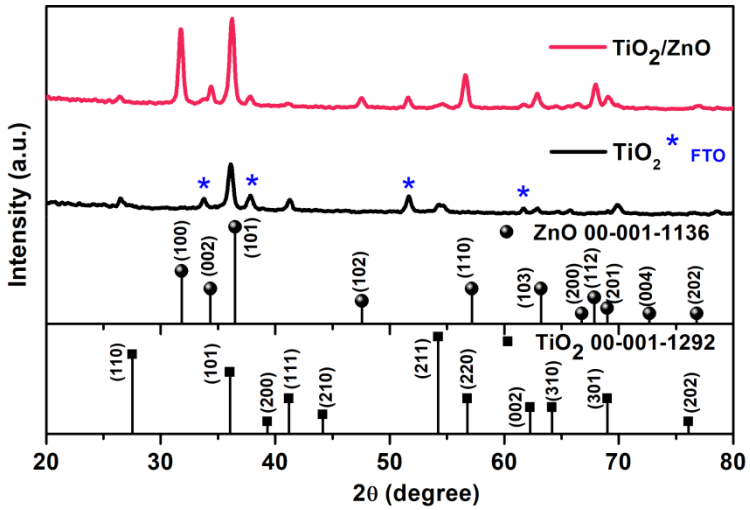

Figure 6.1. Glancing angle X-ray diffraction pattern of TiO_2/ZnO hierarchical structures.

The crystal structure of the samples was analyzed using glancing angle X-ray diffraction analysis. All the diffraction peaks in figure 6.1 can be indexed to (110), (101), (211) and (301) planes of tetragonal rutile TiO_2 (Card No: 00-001-1292) and (100), (002), (101) and (110) planes of

wurtzite hexagonal ZnO (Card No: 00-001-1136) of the composite structure.

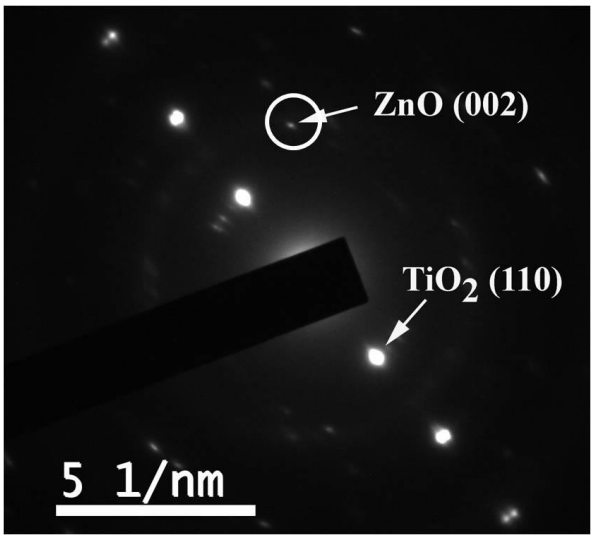

Figure 6.2. SAED pattern of TiO_2/ZnO hierarchical structure.

The detailed structural investigations of the samples were done using SAED analysis. The SAED pattern in figure 6.2 shows the (002) plane of ZnO and (110) plane of TiO_2. The presence of bright spots in the SAED pattern confirms the crystalline nature of the samples.

Micro Raman spectroscopy is a useful technique to analyze the vibrational properties of nanomaterials. Raman spectra of the samples recorded at an excitation of 514 nm are displayed in figure 6.3. The first order Raman spectrum of rutile TiO_2 shows four Raman active fundamental modes such as B_{1g} (144 cm^{-1}), E_g (446 cm^{-1}), A_{1g} (610 cm^{-1}) and B_{2g} (826 cm^{-1}) along with secondary scattering features, most

prominent one being at 238 cm^{-1}.[171,172] All the modes except B_{2g} are present in the spectra of TiO_2. In addition to the vibrations of TiO_2, the vibrational modes E_{2L} (98 cm^{-1}) and E_{2H} (437 cm^{-1}) corresponding to wurtzite hexagonal structure of ZnO are also present in the Raman spectra of TiO_2/ZnO hierarchical structure.[186]

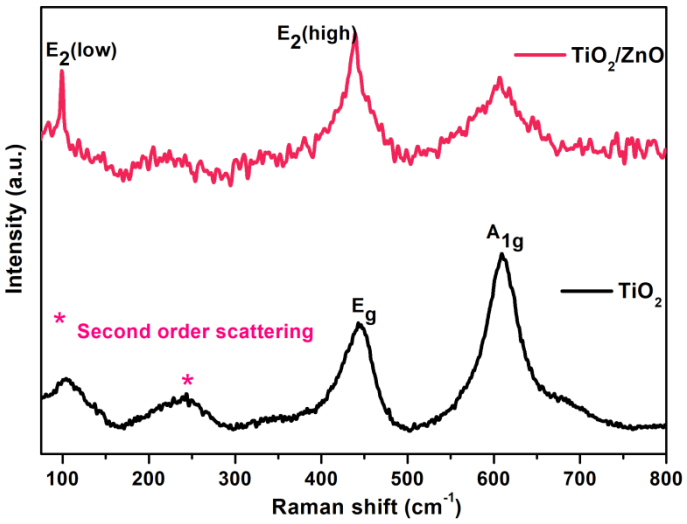

Figure 6.3. Micro Raman spectra of TiO_2/ZnO hierarchical structures.

The morphology of the samples was analyzed using FESEM analysis. The growth of vertically aligned tetragonal rod shaped TiO_2 nanorods with a diameter approximately 50 nm is clear from figure 6.4(b). In the FESEM image of TiO_2/ZnO structures shown in figure 6.4(d), the growth of hexagonal shaped of ZnO nanorods (yellow circle) over TiO_2 nanorods (red circle) are seen. The diameter of ZnO nanorods is approximately 70 nm. The EDX elemental mapping shows the presence of the elements Ti, Zn and O in the sample.

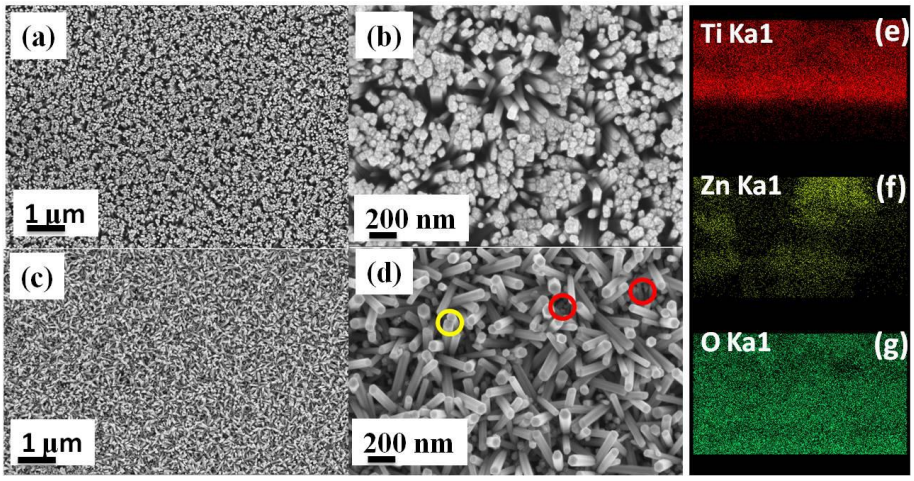

Figure 6.4. FESEM images of (a) and (b) TiO_2 nanorods and (c) and (d) TiO_2/ZnO hierarchical structures (yellow and red circles represent ZnO and TiO_2 nanorods respectively). (e), (f) and (g) are EDX elemental mapping of Ti, Zn, and O respectively.

The basic gas sensing mechanism of metal oxide semiconductors relies on the interaction between target gas molecules and adsorbed oxygen ions on the surface of the semiconductor.[2,130] The adsorption of oxygen ions depends on the operating temperature of the sensor. At temperatures lower than 100°C (T<100°C), oxygen molecules will be adsorbed as O_2^- ions and above 100°C, oxygen will be adsorbed as O^- or O^{2-} ions.[187,188] In ambient air, oxygen molecules trap electrons from the conduction band forming a depletion region and a potential barrier in the material. Reducing gases like ethanol or ammonia react with these adsorbed oxygen ions releasing the trapped electrons back to the material. As a result, the width of the depletion region and hence the height of the potential barrier decreases.

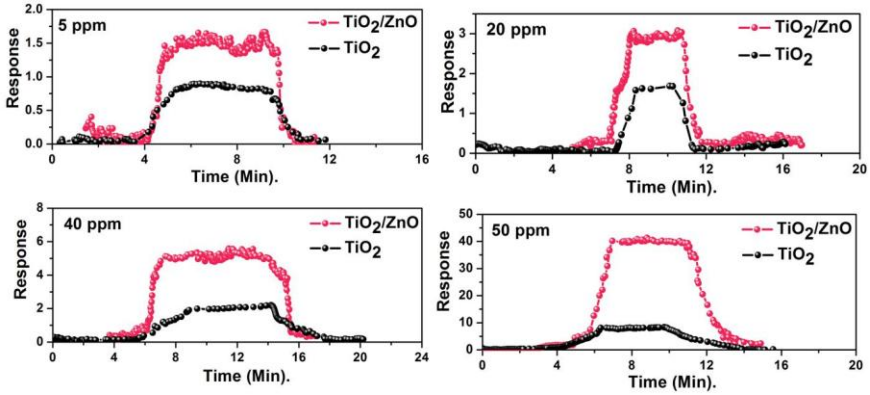

Figure 6.5. Room temperature response of TiO_2 and TiO_2/ZnO to various concentrations of ethanol.

The response characteristics of the samples were investigated by applying 1 V and 3.3 V to TiO_2 and TiO_2/ZnO respectively. The room temperature response of TiO_2 and TiO_2/ZnO to various concentrations of ethanol is shown in figure 6.5. TiO_2/ZnO hierarchical structure show enhanced response to all the concentrations of ethanol used in the present study. The enhanced response of TiO_2/ZnO to 50 ppm ethanol is 40, whereas the response was 8 for TiO_2 alone. As shown in figure 6.6, the response of both TiO_2 and TiO_2/ZnO increases with increase in the concentration of ethanol due to the increased number of gas molecules at high concentrations.

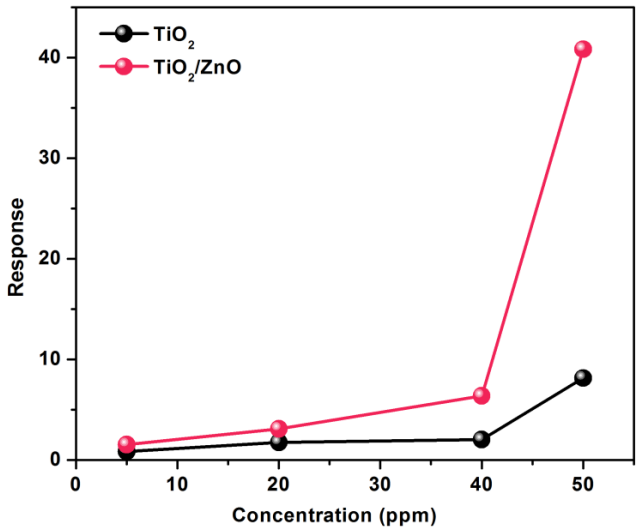

Figure 6.6. Comparison of ethanol response of TiO_2 and TiO_2/ZnO hierarchical structures.

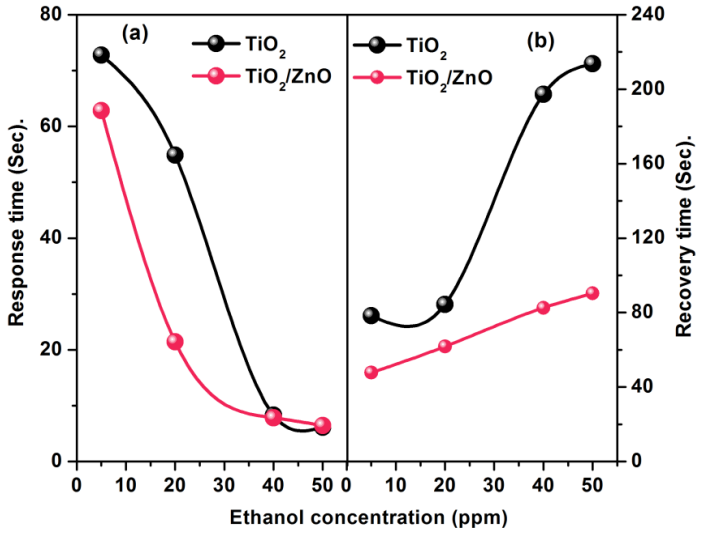

Figure 6.7. (a) Response time and (b) recovery time of TiO_2 and TiO_2/ZnO with various concentrations of ethanol.

Figure 6.7 shows the variation in response time and recovery times of the fabricated sensors with various concentrations of ethanol. The response time decreases and recovery time increases with increase in the concentration of ethanol. The increase in recovery time is due to the slow desorption rate of ethanol at room temperature. For 50 ppm concentration of ethanol, the response time of TiO_2 and TiO_2/ZnO are 6 seconds and recovery time has been reduced from 213 seconds to 90 seconds. The high value of response and low value of response and recovery time can be attributed to the increased surface to volume ratio as well as due to the formation of n-n heterojunctions at the interface of TiO_2 and ZnO.

Nanomaterials with high surface to volume ratio are more suitable for fabricating high-performance gas sensors. Hierarchical structures enhance the gas sensing parameters of a semiconductor gas sensor due to the formation of multiple junctions at the interface of the materials constituting the structure.[104,189,190] Figure 6.9 shows the band diagram of TiO_2/ZnO before and after thermal equilibrium. Due to the difference in work function of TiO_2 (4.9 eV) and ZnO (5.3 eV), electrons flow from the conduction band of TiO_2 to the conduction band of ZnO until thermal equilibrium is reached.[59,184] The migration of electrons from TiO_2 to ZnO leads to the formation of an accumulation layer on ZnO and a depletion layer on TiO_2. The accumulation layer is further depleted by additional oxygen adsorption leading to enhanced gas sensing performance of TiO_2/ZnO hierarchical structure.[70,191]

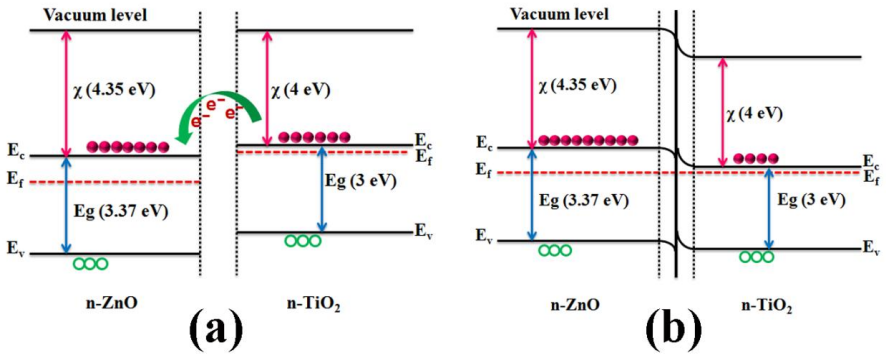

Figure 6.8. Band diagram of TiO_2/ZnO hierarchical structure at (a) before equilibrium and (b) after equilibrium.

Usually, alcohol molecules react with adsorbed oxygen ions and undergo dehydrogenation and dehydration reactions to form CO_2 and H_2O respectively depending on the operating temperature of the sensor. Since sensors in the present work operate at room temperature, ethanol molecules undergo dehydrogenation reactions by breaking $C-O$ and $O-H$ bonds due to their lower bond breaking energies and form aldehyde and water represented by the equation (5.1).[120,129]

$$CH_3CH_2OH_{(g)} + O_2^-{}_{(ads)} \rightarrow \begin{cases} [CH_3CH_2O]^-{}_{(ads)} + OH^-{}_{(ads)} \\ CH_3CHO + H_2O + e^- \end{cases} \quad (5.1)$$

6.4 Conclusion

TiO_2/ZnO hierarchical structures were grown by two-step hydrothermal method and its room temperature ethanol sensing characteristics were investigated. Both TiO_2 and TiO_2/ZnO show a good response to ethanol at room temperature and the heterojunction sensor

show improved response characteristics. The room temperature operation makes the fabricated device a potential candidate for future gas sensing applications.

Chapter 7

Conclusions and scope for future works

This chapter summarizes the results presented in the thesis and future prospects of hierarchical metal oxide semiconductor nanostructure gas sensors operating at room temperature.

7.1 Conclusions

In recent years, tremendous efforts have been directed towards the development of low- cost, portable, efficient gas sensors with good response, fast response and recovery times, and low power consumption for practical applications. In the present investigation, we have fabricated room temperature gas sensors based on various metal oxide hierarchical nanostructures.

ZnO based gas sensors are well established in the gas sensor research field. We have developed ZnO/CuO heterojunction sensors using low-temperature solution methods and demonstrated its capability to detect gases like ethanol, hydrogen sulfide, and ammonia. The p-n heterojunction formed at the interface of ZnO and CuO as well as the increased surface area provided by the one dimensional ZnO nanorods and its surface modification by CuO nanoparticles improved the gas sensing properties of ZnO/CuO device compared to that of pristine ZnO.

Metal nanoparticles are attractive for their inherent catalytic properties which can enhance the performance of various devices. Ag nanoparticle decorated TiO_2 nanorods fabricated in the present study significantly improved the room temperature gas sensing properties especially the response and recovery time. The well separated one-dimensional morphology of TiO_2 nanorods and the exceptional catalytic properties of Ag nanoparticles are the reasons for the better performance of Ag-TiO_2 structure compared to that of TiO_2.

A better gas sensor should have a high value of response and low values for response and recovery time. With the addition of Ag nanoparticles on TiO_2 nanorods, we were able to fabricate room temperature gas sensors with fast response fast recovery. Still, the response value was not much enhanced. The fabrication of p-CuO/n-TiO_2 heterojunction markedly improved the room temperature response of the sensor. Also, the presence of CuO nanoparticles lowered the response time making it suitable for practical device applications. But the recovery time was almost constant for both TiO_2 and TiO_2/CuO. The p-n junction

formation and the increased number of gas adsorption sites enhanced the response and lowered the response time of the heterojunction sensor.

In the present study, it has been observed that the addition of CuO and Ag nanoparticles on TiO_2 nanorods enhanced the room temperature response and lowered the response and recovery time of the sensors respectively. In order to get all the sensing parameters improved together in a single device, we have grown TiO_2/ZnO hierarchical structure and its room temperature response characteristics were investigated. The migration of electrons across the interface of TiO_2 and ZnO form an accumulation layer in ZnO which is further depleted by additional oxygen adsorption thereby improving all the response characteristics of the hierarchical sensor at room temperature. The simple processing techniques and room temperature response of all the fabricated sensors make them potential candidates for future sensing applications. The table below compares the ethanol response characteristics of some gas sensors.

Table 7.1. Comparison of ethanol response of some metal oxide based gas sensors.

Sl. No.	Material	Synthesis method	Ethanol concentration (ppm)	Operating temperature	Response	Response-recovery times (S)	Ref.
1	ZnO	CVD	40	RT	25	60/20	[192]
2	Co_3O_4/ TiO_2	Anodization/ hydrothermal	100	260°C	40	1.4/7.2	[183]
3	ZnO/CuO	Hydrothermal	150	RT	2.3	70/88	[193]

4	TiO_2/ $Ag_{0.35}V_2O_5$	Electro spinning	100	350°C	15	7/8	[178]
5	Ag-$SnO_{1.8}$	Aerosol route	1000	400°C	45	2/45	[194]
6	Ag-ZnO	Hydrothermal	20	370°C	20	15/20	[195]
7	TiO_2/SnO_2	Hydrothermal	10	43°C	11	2400/300	[182]
8	Al-ZnO	Sol gel	160	RT	0.82	68/50	[138]
9	Au-ZnO	Hydrothermal	50	325	7	5/20	[196]
10	ZnO	Hydrothermal	50	RT	2	98/508	Present work
11	TiO_2	Hydrothermal	50	RT	8	6/213	Present work
12	ZnO/CuO	Hydrothermal /wet chemical	50	RT	5	9/420	Present work
13	Ag-TiO_2	Hydrothermal /wet chemical	50	RT	11	3/73	Present work
14	TiO_2/CuO	Hydrothermal /wet chemical	50	RT	34	2/228	Present work
15	TiO_2/ZnO	Hydrothermal	50	RT	40	6/90	Present work

7.2 Future scope

The thesis covers the room temperature ethanol sensing characteristics of TiO_2 and ZnO based hierarchical structures. The gas sensing is solely a surface phenomenon which involves the interaction between target gas molecules and adsorbed oxygen ions on the surface of the metal oxide semiconductor. Therefore all the devices developed can be used for the detection of other poisonous gases like NO_2, CO, volatile organic compounds (VOCs) etc. Even at room temperature, the fabricated devices show good response characteristics, hence can be used for the detection of explosive gases where high temperature is undesirable.

Nowadays one of the most important applications of gas sensors is in breath analysis. The presence of component gases like ammonia, hydrogen sulfide, acetone, toluene etc. in the exhaled breath is in correlation with specific diseases such as kidney malfunction, halitosis, diabetes, lung cancer and so on. Metal oxide nanostructure-based breath sensing is an emerging technique for early disease diagnosis due to their portability, real-time analysis, low-cost etc. In this thesis, as an example, we have shown the response characteristics of some metal oxide heterojunction sensors to ethanol, hydrogen sulfide and ammonia and the lowest concentration detected was 5 ppm. The results show that the heterojunction sensors can also be used for clinical diagnostic applications.

We have seen that the sensor response of nanostructures is in direct relationship with the size of the nanomaterial. Equation (1.19) shows that if the size of the nanomaterial is of the order of its Debye

length, a high value of sensor parameters can be obtained. Also, poor selectivity, which is the major drawback of metal oxide gas sensors, can be improved by fabricating an array of various metal oxide sensors in a single device.

Appendix

Abbreviations used in the thesis

Abbreviation	Expansion
Ag	Silver
Au	Gold
CuO	Copper Oxide
EDX	Energy-dispersive X-ray spectroscopy
FESEM	Field Emission Scanning Electron Microscopy
FTO	Fluorine doped Tin Oxide
HCl	Hydro Chloric Acid
H_2S	Hydrogen Sulfide
H_2O	Water
HRXRD	High resolution X-ray diffraction
HRTEM	High Resolution Transmission Electron Microscopy
I-V	Current-Voltage
ITO	Tin doped Indium Oxide
IUPAC	International Union of Pure and Applied Chemistry
MO	Metal Oxide
SnO_2	Tin Dioxide

SAED	Selected Area Electron Diffraction
TiO_2	Titanium Dioxide
TTIP	Titanium Tetra Iso Propoxide
UV	Ultra Violet
VOC	Volatile Organic Compounds
ZnO	Zinc Oxide

Bibliography

[1] E. Comini, C. Baratto, I. Concina, G. Faglia, M. Falasconi, M. Ferroni, V. Galstyan, E. Gobbi, A. Ponzoni, A. Vomiero, D. Zappa, V. Sberveglieri, and G. Sberveglieri, Sens. Actuators B Chem 179, 3 (2013).

[2] S. Choopun, N. Hongsith, and E. Wongrat, in Nanowires - Recent Adv., edited by X. Peng, First edit (InTech, Croatia, 2012), pp. 1–24.

[3] P. Shankar, J. Bosco, and B. Rayappan, Sci. Jet 126, 1 (2015).

[4] N. Hongsith, E. Wongrat, T. Kerdcharoen, and S. Choopun, Sens. Actuators B Chem 144, 67 (2010).

[5] Y. Shimizu and M. Egashira, MRS Bull. 24, 18 (1999).

[6] X. Liu, S. Cheng, H. Liu, S. Hu, D. Zhang, and H. Ning, Sensors 12, 9635 (2012).

[7] N. Yamazoe, G. Sakai, K. Shimanoe, N.Y. Ã, G. Sakai, and K. Shimanoe, Catal. Surv. from Asia 7, 63 (2003).

[8] G.F. Fine, L.M. Cavanagh, A. Afonja, and R. Binions, Sensors 10, 5469 (2010).

[9] N. Yamazoe, Sens. Actuators B Chem 108, 2 (2005).

[10] X.J. Huang and Y.K. Choi, Sens. Actuators B Chem 122, 659 (2007).

[11] G.J. Cadena, J. Riu, and F.X. Rius, Analyst 132, 1083 (2007).

[12] J. Tao and M. Batzill, in Met. -Oxide Nanowires Chem. Sensors, edited by A.K. Michael A, Sanjay Mathur (Springer Science & Business Media, Germany, 2013), pp. 35–68.

[13] S. Sharma and M. Madou, Philos. Trans. A. Math. Phys. Eng. Sci. 370, 2448 (2012).

[14] H. Zeng, G. Duan, Y. Li, S. Yang, X. Xu, and W. Cai, Adv. Funct. Mater. 20, 561 (2010).

[15] B.K. Meyer, H. Alves, D.M. Hofmann, W. Kriegseis, D. Forster, F. Bertram, J. Christen, a. Hoffmann, M. Straßburg, M. Dworzak, U. Haboeck, and a. V. Rodina, Phys. Status Solidi Basic Res. 241, 231 (2004).

[16] A.M. Azad, S.A. Akbar, S.G. Mhaisalkar, L.D. Birkefeld, and K.S. Goto, J. Electrochem. Soc. 139, 3690 (1992).

[17] W.H. Brattain and J. Bardeen, Bell Labs Tech. J. 32, 1 (1953).

[18] G. Heiland, Z. Phys. 138, 459 (1954).

[19] T. Seiyama and A. Kato, Anal. Chem. 34, 1502 (1962).

[20] P.J. Shaver, Appl. Phys. Lett 11, 255 (1967).

[21] N. Taguchi, US3631436 A (1971).

[22] H. Meixner and U. Lampe, Sens. Actuators B 33, 198 (1996).

[23] G. Korotcenkov, Sens. Actuators B 107, 209 (2005).

[24] M.R. Mahmood, T. Soga, M.H. Mamat, Z. Khusaimi, and A.M. Nor, Adv. Mater. Res. 667, 329 (2013).

[25] A. Tricoli, M. Righettoni, and S.E. Pratsinis, Nanotechnology 20, 315502 (2009).

[26] F. Wolkenstein, Discuss. Faraday Soc 31, 209 (1961).

[27] N. Yamazoe, Y. Kurokawa, and T. Seiyama, Sens. Actuators B Chem 4, 283 (1983).

[28] S.R. Morrison, Sens. Actuators 2, 329 (1981).

[29] P. Shankar, J. Bosco, and B. Rayappan, Sci. Lett. J. 4:126, 1 (2015).

[30] D. Kohl, in Gas Sensors, edited by G. Sberveglieri, First edit (Springer Netherlands, Germany, 1992), pp. 43–88.

[31] G. Neri, Chemosensors 3, 1 (2015).

[32] M. Gardon and J. M. Guilemany, J. Mater. Sci. Mater. Electron. 24, 1410 (2013).

[33] R.L. van der Wal, G.W. Hunter, J.C. Xu, M.J. Kulis, G.M. Berger, and T.M. Ticich, Sens. Actuators B Chem 138, 113 (2009).

[34] Y.F. Sun, S.B. Liu, F.L. Meng, J.Y. Liu, Z. Jin, L.T. Kong, and J.H. Liu, Sensors 12, 2610 (2012).

[35] G. Korotcenkov, Mater. Sci. Eng. B 139, 1 (2007).

[36] Z.P. Tshabalala, D.E. Motaung, G.H. Mhlongo, and O. M. Ntwaeaborwa, Sens. Actuators B Chem 224, 841 (2015).

[37] Y. Wang, G. Duan, Y. Zhu, H. Zhang, Z. Xu, Z. Dai, and W. Cai, Sens. Actuators B Chem 228, 74 (2016).

[38] Z.S. Hosseini, A.I. Zad, and A. Mortezaali, Sens. Actuators B Chem 207, 865 (2015).

[39] F. Mendoza, D.M. Hernández, V. Makarov, E. Febus, B.R. Weiner, and G. Morell, Sens. Actuators B Chem 190, 227 (2014).

[40] C.H. Xu, S.Q. Shi, and C. Surya, in Handb. Nanoceramics Their Based Nanodevices, edited by T.-Y. Tseng and H.S. Nalwa (American Scientific Pub, Hong Kong, 2009), pp. 1–22.

[41] J.R.D. Retamal, C.Y. Chen, D.H. Lien, M.R.S. Huang, C.A. Lin, C.P. Liu, and J.H.He, ACS Photonics 1, 354 (2014).

[42] E. Wongrat, N. Hongsith, D. Wongratanaphisan, A. Gardchareon, and S. Choopun, Sens. Actuators B Chem 171–172, 230 (2012).

[43] N. Barsan and U.D.O. Weimar, J. Electroceramics 7, 143 (2001).

[44] N. Barsan and U.D.O. Weimar, J. Phys. Condens. Matter 15, R813 (2003).

[45] N.D. Hoa, N.V. Duy, S.A. El-safty, and N.V. Hieu, J. Nanomater. 2015, 1 (2015).

[46] W. Göpel, Prog. Surf. Sci. 20, 9 (1985).

[47] N. Yamazoe, Sens. Actuators B 5, 7 (1991).

[48] C. Xu, J. Tamaki, N. Miura, and N. Yamazoe, Sens. Actuators B Chem 3, 147 (1991).

[49] N. Yamazoe and K. Shimanoe, in Sci. Technol. Chemiresistor Gas Sensors, edited by D.K. Aswal and S.K. Gupta (Nova Science Publishers, Inc., New York, 2007), pp. 1–32.

[50] E. Comini, Anal. Chim. Acta 568, 28 (2006).

[51] H. Ogawa, M. Nishikawa, and A. Abe, J. Appl. Phys. 53, 4448 (1982).

[52] D.K. Schroder, Semiconductor Material and Device Characterization, Second ed. (John Wiley & Sons, INC., Arizona, 1998).

[53] A. Mirzaei, S.G. Leonardi, and G. Neri, Ceram. Int. 42, 15119 (2016).

[54] J. Zhang, L. Xianghong, G. Neri, and N. Pinna, Adv. Mater. 28, 795 (2016).

[55] P. Rai, W. Kwak, and Y. Yu, ACS Appl. Mater. Interfaces 5, 3026 (2013).

[56] S.M. Sze and K.K. Ng, Physics of Semiconductor Devices, Third ed. (John Wiley & Sons Inc., New Jersey, 2006).

[57] A. Chen, S. Bai, B. Shi, Z. Liu, D. Li, and C. Liu, and C.C.Liu, Sens. Actuators B Chem 135, 7 (2008).

[58] H. Xu, J. Ju, W. Li, J. Zhang, J. Wang, and B. Cao, Sens. Actuators B Chem 228, 634 (2016).

[59] C.W. Zou, J. Wang, and W. Xie, J. Colloid Interface Sci. 478, 22 (2016).

[60] H. Gu, Z. Wang, and Y.Hu, Sensors 12, 5517 (2012).

[61] M. Rumyantseva, V. Kovalenko, A. Gaskov, E. Makshina, V. Yuschenko, I. Ivanova, A. Ponzoni, G. Faglia, and E. Comini, Sens. Actuators B Chem 118, 208 (2006).

[62] Y. Zeng, Y. Bing, L. Chang, W. Zheng, and G. Zou, Trans. Nonferrous Met. Soc. China 22, 2451 (2012).

[63] C. Liangyuan, B. Shouli, Z. Guojun, L. Dianqing, C. Aifan, and C.C. Liu, Sens. Actuators B Chem 134, 370 (2008).

[64] T. Li, W. Zeng, and Z. Wang, Sens. Actuators B Chem 221, 1570 (2015).

[65] D.A. Neamen, Semiconductor Physics and Devices Basic Principles, Third ed. (McGraw-HIII Education, New York, 2003).

[66] M. Kwiatkowski, I. Bezverkhyy, and M. Skompska, J. Mater. Chem. A 3, 12748 (2015).

[67] B. Liu, Y. Sun, D. Wang, L. Wang, L. Zhang, X. Zhang, Y. Lin, and T. Xie, RSC Adv. 4, 32773 (2014).

[68] E. Roduner, Chem. Soc. Rev. 43, 8226 (2014).

[69] R.F. Pierret, Semiconductor Device Fundamentals, First ed.

(Addison wesley Publishing Company, United States of America, 1996).

[70] S. Park, S. An, H. Ko, S. Lee, H.W. Kim, and C. Lee, Appl. Phys. A 115, 1223 (2014).

[71] H. Morkoç and U. Ozgur, Zinc Oxide Fundamentals, Materials and Device Technology, First ed. (Wiley-VCH Verlag GmbH & Co. KGaA, Weinheim, 2009).

[72] Ü. Özgür, Y.I. Alivov, C. Liu, A. Teke, M.A. Reshchikov, S. Doğan, V. Avrutin, S.J. Cho, and H. Morkoç, J. Appl. Phys. 98, 1 (2005).

[73] D. Hwang, M. Oh, J. Lim, and S. Park, J. Phys. D. Appl. Phys. 40, R387 (2007).

[74] S.K. Gupta, A. Joshi, and M. Kaur, J. Chem. Sci. 122, 57 (2010).

[75] M.Y. Liao, L. Fang, C.L. Xu, F. Wu, Q.L. Huang, and M. Saleem, Mater. Sci. Semicond. Process. 24, 1 (2014).

[76] H. Wang, Y. Liu, M. Li, H. Huang, H.M. Xu, R.J. Hong, and H. Shen, Optoelectron. Adv. Mater. Rapid Commun. 4, 1166 (2010).

[77] R. Daghrir, P. Drogui, and D. Robert, Ind. Eng. Chem. Res. 52, 3581 (2013).

[78] P.P. Subha and M.K. Jayaraj, J. Exp. Nanosci. 10, 1106 (2015).

[79] J. Qiu, S. Li, E. Gray, H. Liu, Q. Gu, C. Sun, C. Lai, H. Zhao, and S. Zhang, J. Phys. Chem. C 118, 8824 (2014).

[80] G.L. Chiarello, A. Zuliani, D. Ceresoli, R. Martinazzo, and E. Selli, ACS Catal. 6, 1345 (2016).

[81] J. Wang, T. Zhang, D. Wang, R. Pan, Q. Wang, and H. Xia, J. Alloys Compd. 551, 82 (2013).

[82] F.B. Kessler, Chinese Sci. Bull. 56, 1639 (2014).

[83] O. Carp, C.L. Huisman, and A. Reller, Prog. Solid State Chem. 32, 33 (2004).

[84] O. Brian and M. Grätzel, Nature 353, 737 (1991).

[85] A. Fujishima and K. Honda, Nature 238, 37 (1972).

[86] I. Kim, S. Choi, S. Kim, and J. Jang, in Smart Sensors Heal. Environ. Monit., edited by C. Kyung (Springer Netherlands, 2015), pp. 19–49.

[87] G. Skandan and A. Singhal, in Nanomater. Handb., edited by Y. Gogotsi (CRC Press, New Jersey, 2006).

[88] G. Cao, Nanostructures and Nanomaterials; Synthesis, Properties and Applications, First ed. (Imperial College Press, USA, 2004).

[89] A. Varma, A.S. Mukasyan, A. Rogachev, and K. Manukyan., Chem. Rev. 116, 14493 (2016).

[90] K. Byrappa and M. Yoshimura, Handbook of Hydrothermal Technology, Second ed. (Noyes Publications, U.S.A, 2012).

[91] A. Rabenau, Angew. Chemie Int. Ed. English 24, 1026 (1985).

[92] G.S. Bumbrah and R.M. Sharma, Egypt. J. Forensic Sci. 6, 209 (2016).

[93] B.B. Laud, in Lasers Non-Linear Opt., Second ed. (New Age International (P) Limited, New Delhi, 2003), pp. 205–207.

[94] A. Janotti and C.G. Van de Walle, Reports Prog. Phys. 72, 126501 (2009).

[95] C.C. Li, Z.F. Du, L.M. Li, H.C. Yu, Q. Wan, and T.H. Wang, Appl. Phys. Lett. 91, 2005 (2007).

[96] R.C. Pawar, J.S. Shaikh, S.S. Suryavanshi, and P.S. Patil, Curr. Appl. Phys. 12, 778 (2012).

[97] M. Mccune, W. Zhang, and Y. Deng, Nano Lett. 12, 3656 (2012).

[98] F. Pan, C. Song, X.J. Liu, Y.C. Yang, and F. Zeng, Mater. Sci. Eng. R 62, 1 (2008).

[99] J. Huang, Z. Yin, and Q. Zheng, Energy Environ. Sci. 4, 3861 (2011).

[100] M.T. Qamar, M. Aslam, I.M.I. Ismail, N. Salah, and A. Hameed, ACS Appl. Mater. Interfaces 7, 8757 (2015).

[101] S. Ranwa, M. Kumar, J. Singh, M. Fanetti, and M. Kumar, J. Appl. Phys. 118, 34509 (2015).

[102] K.V. Gurav, M.G. Gang, S.W Shin, U.M. Patil, P.R. Deshmukh, G.L. Agawane, M.P. Suryawanshi, S.M. Pawar, P.S. Patil, C.D. Lokhande, and J.H. Kim, Sens. Actuators B Chem 190,439 (2014).

[103] J. Park, I. Mahmud, H. Jae, M. Park, A. Ranjkesh, D. Kyung, and H. Kim, Appl. Surf. Sci. 362, 132 (2016).

[104] M.R. Alenezi, S.J. Henley, G. Emerson, and S.R.P. Silva, Nanoscale 6, 235 (2014).

[105] Q. Simon, D. Barreca, A. Gasparotto, C. Maccato, E. Tondello, C. Sada, E. Comini, A. Devi, and R. Fischer, Nanotechnology 23, 25502 (2012).

[106] S. Öztürk, A. Kösemen, Z. Alpaslan, N. Kılınc, Z.Z. Öztürk, and M. Penza, Sensors Actuators B. Chem. 222, 280 (2016).

[107] A. Dhara, B. Show, A. Baral, S. Chabri, A. Sinha, N.R. Bandyopadhyay, and N. Mukherjee, Sol. Energy 136, 327 (2016).

[108] D.R. Miller, S.A. Akbar, and P.A. Morris, Sens. Actuators B Chem 204, 250 (2014).

[109] A. Zainelabdin, S. Zaman, G. Amin, O. Nur, and M. Willander, Appl. Phys. A 108, 921 (2012).

[110] Q. Ahsanulhaq, A. Umar, and Y.B. Hahn, Nanotechnology 18, 115603 (2007).

[111] X. Cai, B. Han, S. Deng, Y. Wang, C. Dong, Y.W. Djerdj, and I. Djerdj, Cryst. Eng. Comm 16, 7761 (2014).

[112] J.X. Wang, X.W. Sun, Y. Yang, K.K.A. Kyaw, X.Y. Huang, J.Z. Yin, J. Wei, and H.V. Demir, Nanotechnology 22, 325704 (2011).

[113] B.Y. Zhu, C.H. Sow, T. Yu, Q. Zhao, P. Li, Z. Shen, D. Yu, and J.T.L. Thong, Adv. Funct. Mater. 16, 2415 (2006).

[114] N.M. Vuong, N.D. Chinh, B.T. Huy, and Y. Lee, Sci. Rep. 6, 26736 (2016).

[115] C. Shao, Y. Chang, and Y. Long, Sens. Actuators B Chem 204, 666 (2014).

[116] M.R. Yu, G. Suyambrakasam, R.J. Wu, and M. Chavali, Mater. Res. Bull. 47, 1713 (2012).

[117] M. Batzill, Sensors 6, 1345 (2006).

[118] N. Barsan and U.D.O. Weimar, J. Electroceramics 7, 143 (2001).

[119] N. Yamazoe and K. Shimanoe, J. Sensors 2009, 1 (2009).

[120] D. Acharyya and P. Bhattacharyya, Sens. Actuators B Chem 228, 373 (2016).

[121] Y. Bin, J. Yin, L. Li, L.X. Zhang, and L.J. Bie, Sens. Actuators B Chem 202, 500 (2014).

[122] Y. Guo, M. Gong, Y. Li, Y. Liu, and X. Dou, Nanoscale Res. Lett. 11:475, 1 (2016).

[123] I. Singh and R.K. Bedi, J. Mater. Sci. 46, 5568 (2011).

[124] S. Park, H. Ko, S. Kim, and C. Lee, ACS Appl. Mater. Interfaces 6, 9595 (2014).

[125] C. Wang, X.Q. Fu, X.Y. Xue, Y.G. Wang, and T.H. Wang, Nanotechnology 18, 145506 (2007).

[126] A. Hazra, K. Dutta, B. Bhowmik, and P. Bhattacharyya, IEEE

Sens. J. 15, 408 (2015).

[127] W. Song, P. Liu, and E.J.M. Hensen, Catal. Sci. Techology 4, 2997 (2014).

[128] Y. Chen, L. Yu, D. Feng, M. Zhuo, M. Zhang, E. Zhang, Z. Xu, Q. Li, and T. Wang, Sens. Actuators B Chem 166–167, 61 (2012).

[129] Y.J. Chen, C.L. Zhu, and G. Xiao, Sens. Actuators B 129, 639 (2008).

[130] M.M. Arafat, B. Dinan, S.A. Akbar, and A.S.M.A. Haseeb, Sensors 12, 7207 (2012).

[131] N. Rahimi, R.A. Pax, and E.M. Gray, Prog. Solid State Chem. 44, 86 (2016).

[132] A. Kolmakov and M. Moskovits, Annu. Rev. Mater. Res. 34, 151 (2004).

[133] E. Comini, C. Baratto, G. Faglia, M. Ferroni, A. Vomiero, and G. Sberveglieri, Prog. Mater. Sci. 54, 1 (2009).

[134] M. Ge, C. Cao, J. Huang, S. Li, and Z. Chen, J. Mater. Chem. A 4, 6772 (2016).

[135] T. Zhai, X. Fang, M. Liao, X. Xu, H. Zeng, B. Yoshio, and D. Golberg, Sensors 9, 6504 (2009).

[136] J. Lee, Sensors Actuators B. Chem. 140, 319 (2009).

[137] H. Wang, X. Huang, Y. Huang, and X. Zhang, Sci. Rep. 2, 1 (2012).

[138] M. Chitra, K. Uthayarani, N. Rajasekaran, N. Neelakandeswari, E.K. Girija, and D.P. Padiyan, Surf. Rev. Lett. 23, 1 (2016).

[139] Y. Lin, P. Deng, Y. Nie, Y. Hu, and L. Xing, Nanoscale 6, 4604 (2014).

[140] P. Hu, G. Du, W. Zhou, J. Cui, J. Lin, H. Liu, D. Liu, J. Wang, and S. Chen, Appl. Mater. Interfaces 2, 3263 (2010).

[141] X. Cheng, Y. Xu, S. Gao, H. Zhao, and L. Huo, Sensors Actuators B Chem. 155, 716 (2011).

[142] N. Bahadur, K. Jain, R. Pasricha, and S. Chand, Sensors Actuators B. Chem. 159, 112 (2011).

[143] J. Huang, Y. Dai, C. Gu, Y. Sun, and J. Liu, J. Alloys Compd. 575, 115 (2013).

[144] D.M. Tobaldi, S.G. Leonardi, R.C. Pullar, M.P. Seabra, G. Neri, and J.A. Labrincha, J. Mater. Chem. A 4, 9600 (2016).

[145] A. Kumar, A.R. Madaria, and C. Zhou, J. Phys. Chem. C 114, 7787 (2010).

[146] P. Soundarrajan, K. Sankarasubramanian, K. Sethuraman, and K. Ramamurthi, Cryst.Eng.Comm 16, 8756 (2014).

[147] G. Korotcenkov, Sens. Actuators B Chem 107, 209 (2005).

[148] M. Chitra, K. Uthayarani, N. Rajasekaran, N. Neelakandeswari, and E.K. Girija, RSC Adv. 6, 111526 (2016).

[149] H. Idriss and E.G. Seebauer, J. Mol. Catal. A Chem. 152, 201

(2000).

[150] F.H. Babaei, N.A. Sheini, and M.M. Lajvardi, in IC-MAST 2015 (2016), p. 12030.

[151] L. Wang, S. Wang, M. Xu, X. Hu, H. Zhang, Y. Wang, and W. Huang, Phys. Chem. Chem. Phys. 15, 17179 (2013).

[152] G. Velmathi, S. Mohan, and R. Henry, Iete Tech. Rev. 1 (2015).

[153] M. Faisal, B. Alam, D. Phan, and G. Chung, Mater. Lett. 156, 113 (2015).

[154] W.C. Conner and J.L. Falconer, Chem Rev 95, 759 (1995).

[155] Z. Zhu, C.T. Kao and R.J. Wu, Appl. Surf. Sci. 320, 348 (2014).

[156] E. Kowalska, A. Lehoux, A. Herissan, B. Ohtani, D. Bahena, V. Briois, J.L. Rodr, and H. Remita, J. Phys. Chem. C 2, 5143 (2016).

[157] R. Zha, R. Nadimicherla, and X. Guo, J. Mater. Chem. A 3, 6565 (2015).

[158] Y.Q. Wang, L. Gu, Y.G. Guo, H. Li, X.Q. He, S. Tsukimoto, Y. Ikuhara, and L.J. Wan, J. Am. Chem. Soc. 134, 7874 (2012).

[159] L. Gao, M. Cao, Y.Q. Fu, Z. Zhong, Y. Shen, and M. Wang, J. Mater. Chem. A 4, 16454 (2016).

[160] J. Kim, J. Yun, and C. Han, Curr. Appl. Phys. 9, e38 (2009).

[161] N. Yamazoe, J. Tamaki, and N. Miura, Mater. Sci. Eng. B 41, 178

(1996).

[162] F. Hooriabad, T. Ueda, K. Kamada, T. Hyodo, Y. Mortazavi, A. Ali, and Y. Shimizu, Sensors Actuators B. Chem. 223, 429 (2016).

[163] E.Z. Tan, P.G. Yin, T.T. You, H. Wang, and L. Guo, ACS Appl. Mater. Interfaces 4, 3432 (2012).

[164] H. Tada, F. Suzuki, S. Ito, T. Akita, K. Tanaka, T. Kawahara, and H. Kobayashi, J. Phys. Chem. B 106, 8714 (2002).

[165] V. Ramakrishnan, H. Kim, J. Park, and B. Yang, RSC Adv. 6, 9789 (2016).

[166] K. Xu, N. Li, D. Zeng, S. Tian, S. Zhang, D. Hu, and C. Xie, ACS Appl. Mater. Interfaces 7, 11359 (2015).

[167] I. Mondal and U. Pal, Phys. Chem. Chem. Phys. 18, 4780 (2016).

[168] J. Zhang, P. Tang, T. Liu, Y. Feng, C. Blackman, and D. Li, J. Mater. Chem. A Mater. Energy Sustain. 5, 10387 (2017).

[169] S. Bai, H. Liu, R. Luo, A. Chen, and D. Li, RSC Adv. 4, 62862 (2014).

[170] H. Kim and J. Lee, Sensors Actuators B Chem. 192, 607 (2014).

[171] P.S. Narayanan, in Proc. Indian Acad. Sci. (1953), pp. 411–414.

[172] J. Parker and R.W. Siegel, J. Mater. Res. 5, 1246 (1990).

[173] N. Yamazoe, G. Sakai, and K. Shimanoe, Catal. Surv. from Asia

7, 63 (2003).

[174] M. Iwamoto, Y. Yoda, N. Yamazoe, and T. Seiyama, J. Phys. Chem. 82, 2564 (1978).

[175] L. Zhang, Z. Gao, C. Liu, Y. Zhang, and Z. Tu, J. Mater. Chem. A 3, 1 (2014).

[176] J. Deng, B. Yu, Z. Lou, L. Wang, R. Wang, and T. Zhang, Sensors Actuators B. Chem. 184, 21 (2013).

[177] D. Acharyya, K.Y. Huang, P.P. Chattopadhyay, M.S. Ho, H. Fecht, and P. Bhattacharyya, Analyst 141, 2977 (2016).

[178] Y. Wang, L. Liu, C. Meng, Y. Zhou, Z. Gao, X. Li, X. Cao, and L. Xu, Sci. Rep. 6, 33092 (2016).

[179] G.D. Moon, J.B. Joo, I. Lee, and Y. Yin, Nanoscale 6, 12002 (2014).

[180] I. Tamiolakis, I.T. Papadas, K.C. Spyridopoulos, and G. Armatas, RSC Adv. 6, 54848 (2016).

[181] J. Tian, Z. Zhao, A. Kumar, I. Boughton, and H. Liu, Chem. Soc. Rev. 43, 6920 (2014).

[182] G. Chen, S. Ji, H. Li, X. Kang, S. Chang, Y. Wang, G. Yu, J. Lu, J. Claverie, Y. Sang, and H. Liu, Appl. Mater. Interfaces 44, 24950 (2015).

[183] Y.Q. Liang, Z.D. Cui, S.L. Zhu, Z.Y. Li, X.J. Yang, Y.J Chen, and J.M. Ma, Nanoscale 5, 10916 (2013).

[184] K. Zakrzewska and M. Radecka, Nanoscale Res. Lett. 12–89, 1 (2017).

[185] E. Mccarthy, S. Garry, D. Byrne, E. Mcglynn, J. Mosnier, E. Mccarthy, S. Garry, D. Byrne, E. Mcglynn, and J. Mosnier, J. Appl. Phys. 110, 124324 (2011).

[186] K.A. Alim, V.A. Fonoberov, M. Shamsa, and A.A. Balandin, J. Appl.Phys. 97, 1 (2005).

[187] D.G. An, S.Y. Davydov, and S.V. Troshin, Tech. Phys. Lett. 34, 795 (2008).

[188] M. Breedon, M.J.S. Spencer, and I. Yarovsky, J. Physics. Condens. Matter 21, 144208 (2009).

[189] J. Zhang, Z. Qin, D. Zeng, and C. Xie, Phys. Chem. Chem. Phys. 19, 6313 (2017).

[190] H. Wang, X. Huang, Y. Huang, and X. Zhang, Sci. Rep. 2:701, 1 (2012).

[191] J. Deng, B. Yu, Z. Lou, L. Wang, R. Wang, and T. Zhang, Sensors Actuators B Chem. 184, 21 (2013).

[192] A.A. Zou, L.Z. Hu, Y. Qiu, G.Y. Cao, J. J. Yu, L.N. Wang, H.Q. Zhang, B. Yin, and L.L. Xu, J. Mater. Sci. Mater. Electron. 26, 4908 (2015).

[193] M. Yu, G. Suyambrakasam, R. Wu, and M. Chavali, Mater. Res. Bull. 47, 1713 (2012).

[194] R. K. Joshi and F. E. Kruis, Appl. Phys. Lett 89, 153116 (2006).

[195] J. Ding, J. Zhu, P. Yao, J. Li, H. Bi, and X. Wang, Ind. Eng. Chem. Res. 54, 8947 (2015).

[196] C. Peng and Y. Liu, Appl. Phys. A Mater. Sci. Process. 111, 1151 (2013).